Title

Gallium Arsenide Photonic Integrated Circuit Platform for Optical Phased Array Applications

Author

Nickerson, Michael

Publication Date

2023

UNIVERSITY OF CALIFORNIA

Santa Barbara

Gallium Arsenide Photonic Integrated Circuit Platform for Optical Phased Array Applications

A dissertation submitted in partial satisfaction

of the requirements for the degree

Doctor of Philosophy

in

Electrical and Computer Engineering

by

Michael J. Nickerson

Committee in charge:

Professor Jonathan Klamkin, Chair
Professor John Bowers
Professor Larry Coldren
Professor Nadir Dagli

October 2023

The dissertation of Michael J. Nickerson is approved.

Professor John Bowers

Professor Larry Coldren

Professor Nadir Dagli

Professor Jonathan Klamkin, Chair

October 2023

Gallium Arsenide Photonic Integrated Circuit Platform for

Optical Phased Array Applications

by

Michael J. Nickerson

This page intentionally left blank.

Acknowledgements

The work in this dissertation is based on research funded by:

MKS Instruments

US Army, STTR program number A22B-T007

A portion of this work was performed in the UCSB Nanofabrication Facility, an open access laboratory.

Use was made of computational facilities purchased with funds from the National Science Foundation (CNS-1725797) and administered by the Center for Scientific Computing (CSC). The CSC is supported by the California NanoSystems Institute and the Materials Research Science and Engineering Center (MRSEC; NSF DMR 2308708) at UC Santa Barbara.

Vita of Michael J. Nickerson

EDUCATION

UC Santa Barbara, Electrical and Computer Engineering	**Sep 2018 – Oct 2023**
Ph.D., GPA 4.00	Oct 2023
M.S.	Jun 2020
University of Washington, Physics	**Aug 2003 - Jun 2006**
B.S., GPA 3.60	Jun 2006

PROFESSIONAL EMPLOYMENT

Senior Photonics Design Engineer, Analog Photonics	Nov 2023 – Present
Graduate Student Researcher, UC Santa Barbara	Sep 2018 – Oct 2023
Assistant Technical Staff, MIT Lincoln Laboratory	May 2014 – Aug 2018
Professional Research Assistant, JILA, University of Colorado	Jun 2006 – Apr 2014
Undergraduate Research Assistant, University of Washington	Aug 2003 – Jun 2006

PUBLICATIONS

M. Nickerson, B. Song, J. Brookhyser, G. Erwin, J. Kleinert, and J. Klamkin, "Gallium arsenide optical phased array photonic integrated circuit," *Opt. Express*, vol. 31, no. 17, pp. 27106–27122, Aug. 2023. https://doi.org/10.1364/OE.492556

M. Nickerson, J. Brookhyser, G. Erwin, B. Song, J. Kleinert, and J. Klamkin, "Gallium Arsenide Optical Phased Array Beam Steering Photonic Integrated Circuit," *Optica Advanced Photonics Congress* (2023), Jul. 2023.

M. Nickerson, P. Verrinder, L. Wang, B. Song, and J. Klamkin, "Broadband Optical Phase Modulator with Low Residual Amplitude Modulation," *Optica Advanced Photonics Congress (2022), paper IW4B.4*, Jul. 24, 2022. https://doi.org/10/grtvck

M. Nickerson *et al.*, "Broadband and Low Residual Amplitude Modulation Phase Modulator Arrays for Optical Beamsteering Applications," *Conference on Lasers and Electro-Optics (2022), paper SS1D.4*, May 15, 2022. https://doi.org/10/grtvcm

P. A. Verrinder *et al.*, "Gallium Arsenide Photonic Integrated Circuit Platform for Tunable Laser Applications," *IEEE Journal of Selected Topics in Quantum Electronics*, vol. 28, no. 1, Jan 2022. https://doi.org/10/gmzfnn

P. A. Verrinder *et al.,* "SGDBR tunable laser on gallium arsenide for 1030 nm lidar applications," *27th International Semiconductor Laser Conference (ISLC)*, Oct 2021. https://doi.org/10/gpd82j

J. Fridlander *et al.*, "Photonic Integrated Circuits for Precision Spectroscopy," *2020 Conference on Lasers and Electro-Optics (CLEO)*, May 2020.

C. A. Wang *et al.*, "MOVPE Growth of LWIR AlInAs/GaInAs/InP Quantum Cascade Lasers: Impact of Growth and Material Quality on Laser Performance," *IEEE Journal of Selected Topics in Quantum Electronics*, vol. 23, no. 6, pp. 1–13, Nov 2017. https://doi.org/10/gfzm6b

M. Nickerson, E. Ames, and P. L. Bender, "Recent LISA studies at the University of Colorado," *J. Phys.: Conf. Ser.*, vol. 154, p. 012027, Mar 2009. https://doi.org/10/bt7dpz

Abstract

Gallium Arsenide Photonic Integrated Circuit Platform for
Optical Phased Array Applications

by

Michael J. Nickerson

Optical beam steering is increasingly utilized for many applications – a well-known example being terrestrial navigation light detection and ranging for autonomous vehicles. The performance requirements for this application and others, including remote sensing for climate monitoring and disaster relief, and even industrial machining for printed circuit board manufacturing and integrated circuit repair, are pushing the limits of existing beam steering solutions. Steering speed is an especially demanding requirement which cannot be met by traditional beam steering methods, and optical phased arrays are the only feasible solution for obtaining GHz-class steering speeds.

By utilizing integrated photonics technology, optical phased arrays can be cost-effectively realized compared to other methods. Yet, typical integrated photonic solutions impose additional restrictions on wavelength and struggle to meet steering speed requirements. Group III-V semiconductor-based integrated photonics platforms, in contrast, are able to provide increased steering speed, and gallium arsenide platforms in particular offer a wide wavelength range covering traditional optical beam steering wavelengths. Moreover, gallium arsenide based materials enable efficient integrated light sources and optical amplification in 900-1300 nm wavelengths and beyond, leading to the possibility of a fully monolithically integrated optical phased array solution.

In this work, a gallium arsenide photonic integrated circuit platform has been developed with fast electro-optic phase modulators to enable GHz-class beam steering, with demonstrated single-sided $V_\pi \cdot L$ phase modulation efficiency ranging from 0.5 V·cm to 1.22 V·cm at wavelengths from 980 nm to 1360 nm. This platform was leveraged to fabricate and demonstrate a 16-channel optical phased array with phase control, with a one-dimensional optical phased array output featuring 0.92° beamwidth, 15.3° grating-lobe-free steering range, 12 dB sidelobe level, and ≥770 MHz single-element electro-optical bandwidth when operating at 1064 nm.

Further development has integrated active material to provide the possibility of on-chip lasers and per-channel gain in an active-passive platform. While still in development, this platform has successfully demonstrated an active-passive fabrication process and produced fully functional of phase modulators and passive elements, paving the way for a fully monolithically integrated photonic integrated circuit platform for optical phased array applications.

Table of Contents

Chapter 1

Introduction

1.1 Motivation and Background

Optical beam steering is increasingly required for a variety of applications undergoing significant growth, ranging from terrestrial navigation LiDAR (light detection and ranging) for autonomous vehicles [1] to free-space optical communication for spacecraft [2], [3], climate monitoring [4], and even disaster relief [5] and industrial machining [6], [7]. These applications are pushing the limits of existing beam steering solutions, especially steering speed. Several of these applications are illustrated in Figure 1.

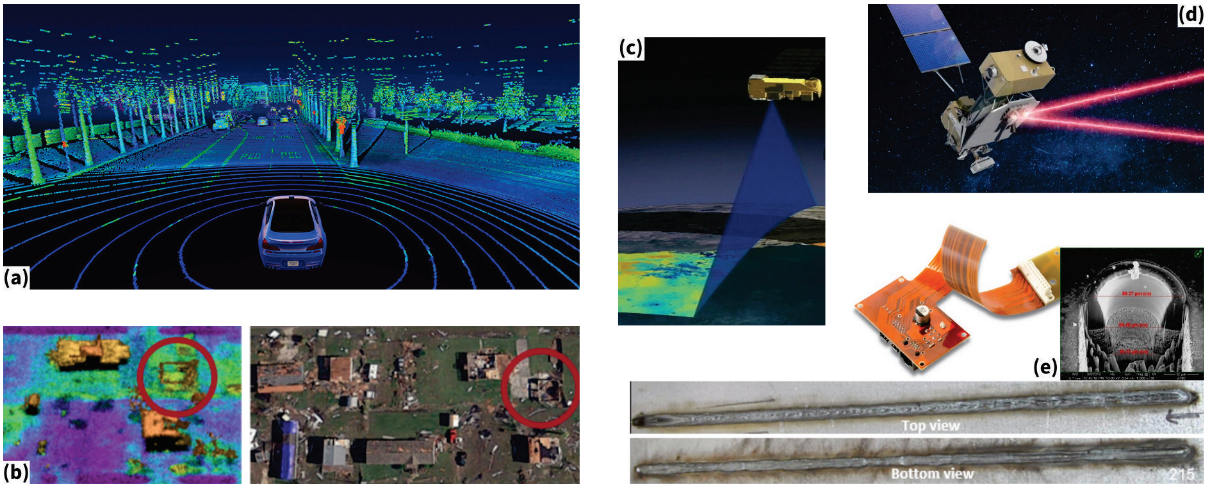

Figure 1: Illustration of multiple applications requiring optical beam steering: (a) LiDAR is used for terrestrial navigation; image reproduced from [8]. (b) LiDAR is used for disaster relief, in this case automated identification of damaged buildings; image adapted from [9]. (c) LiDAR is used for climate monitoring; image adapted from [10]. (d) Free-space laser communication requires beam steering; image reproduced from [11]. (e) Beam steering is used for industrial machining including flexible PCBs, PCB via drilling, and welding; images adapted from [12], [12], [13].

Traditional beam steering methods, illustrated in Figure 2, often utilize rotating sources or gimbals with gross physical movement, resulting in physically large systems that are typically expensive and restricted to Hz-range steering speeds. Industry leader Velodyne's most common LiDAR utilizes a 10 Hz spinning source and is roughly 10 cm across [14], while NASA's next-generation compact free-space laser communication (lasercom) terminals use gimbals significantly larger than 10 cm [15]. Minor physical movement is also used in the form of fast steering mirrors that provide scanning speeds in the kHz range, but these often suffer from large system sizes and complicated optical paths. Acousto-optic deflectors have been used for >200 MHz beam steering, but are limited in wavelength flexibility and optical power handling. No traditional solution can provide GHz-class beam steering speed.

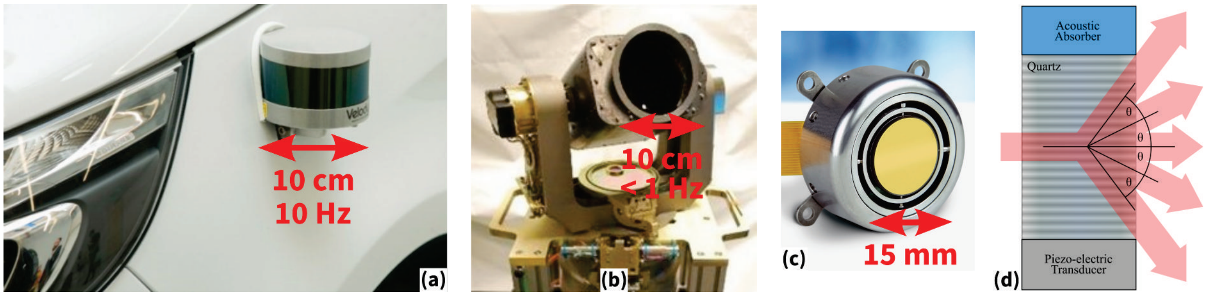

Figure 2: Illustration of existing beam steering solutions: (a) Common automotive LiDAR; image reproduced from [14]. (b) Next-generation "compact" lasercom gimbal, image adapted from [15]. (c) Fast steering mirror, image adapted from [16]. (d) Acousto-optic deflector, image reproduced from [17].

Optical phased arrays (OPAs) are a promising solution for faster beam steering above 1 GHz rates, but traditional OPA implementations have struggled with cost, size, and power handling. More recent methods using photonic integrated circuit (PIC) technology can reduce the cost, size, and weight, yet common PIC platforms impose other limitations on usable wavelengths and maximum achievable steering speeds.

1.2 Photonic Integrated Circuits

Photonic integrated circuit technology, or integrated photonics in general, is the integration of multiple photonic devices on a single semiconductor wafer. PICs were first envisioned in 1969 [18] as devices combining gain material, optical modulators, hybrid couplers, and passive waveguides on a single microchip. This description was developed only a few years after the invention of the gallium arsenide (GaAs) [19]– [21] and gallium arsenide phosphide (GaAsP) [22] heterojunction diode lasers, and the same year as the first room temperature continuous-wave double-heterostructure lasers [23], [24].

While steady improvements in semiconductor growth and manufacturing techniques have enabled corresponding advances in semiconductor lasers and the integration of these on to single microchips, as well as other components including amplifiers, detectors, phase modulators, amplitude modulators, and passive waveguides, PICs have languished compared to electronic integrated circuits. Having primarily served specialized roles as discrete components in fiber-based telecommunications systems, it was not until the 1990s that an appropriate platform emerged for larger scale photonic integration.

Indium phosphide (InP) and related materials can provide efficient direct-bandgap lasers and low-loss passive waveguides over the ideal transmission window of optical fiber in the 1300 nm to 1550 nm wavelength range. Being well matched to the task, the development of PICs based on InP platforms was thus prompted by the growing complexity of telecommunications systems' light sources in the 1990s, especially the introduction of wavelength-division-multiplexing [25]. Since then, the massive investment in worldwide telecommunications technologies has led to an exponential growth in the scale of PICs. Figure 3 presents a recent example of an InP PIC developed for LiDAR applications, illustrating the scale and complexity of such devices.

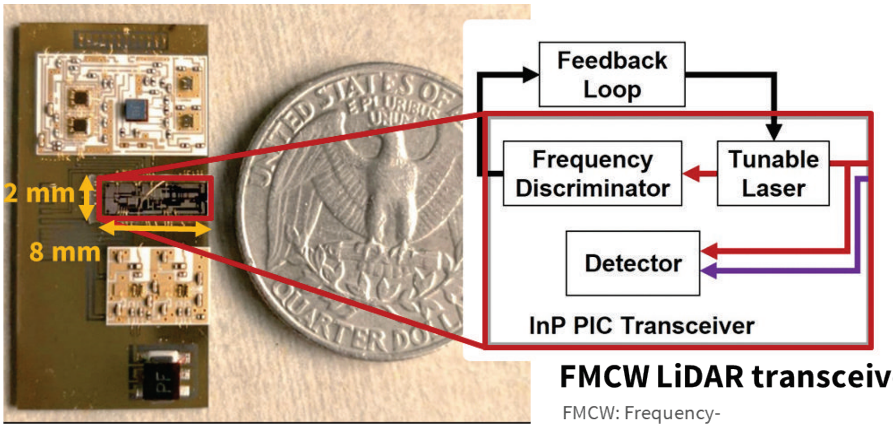

FMCW LiDAR transceiver

FMCW: Frequency-modulated continuous wave

Figure 3: Example of an InP PIC providing all optical components necessary for an FMCW LiDAR system. Adapted from [26].

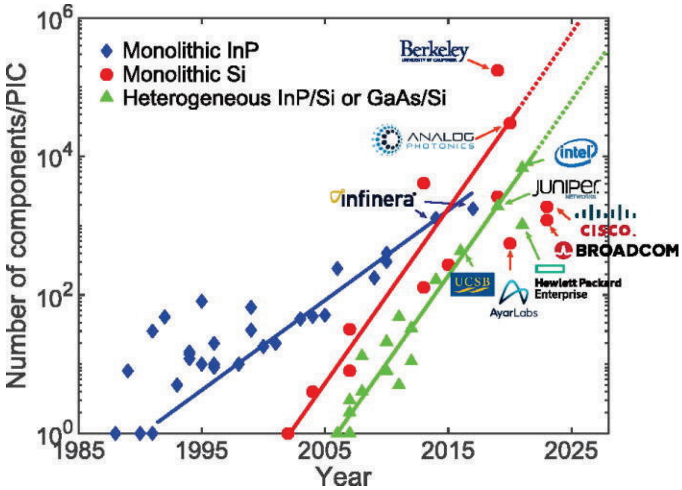

Figure 4: The number of components in a PIC across time for three integrated photonics platforms: indium phosphide, silicon photonics, and silicon photonics heterogeneously integrated with other group III-V materials. Reproduced from [27].

However, while InP PICs with thousands of components on a single chip have been demonstrated, further growth is limited by the large size of InP components and the smaller size of InP substrates compared to other semiconductor processes. InP substrates are fragile, and the largest commercialized wafer size is 4 inches. Silicon (Si) and GaAs are commercially processed with up to 300 mm and 8 inch wafers respectively, enabling much larger economies of scale.

While it started development a decade or two later than InP photonics, silicon photonics (SiPh) has been able to take advantage of the established CMOS fabrication techniques from the electronic IC industry to scale more rapidly than InP technologies, recently surpassing them in terms of components per device [27]. With an indirect bandgap, however SiPh cannot natively provide any active devices. This has been partially addressed by efforts to heterogeneously integrate InP or GaAs with SiPh. Figure 4 shows the relative growth of these PIC technologies.

1.3 Integrated Optical Phased Arrays

Optical phased arrays (OPAs) are a technology that can resolve mechanical beam steering limitations by providing solid-state electronic control, thereby avoiding moving parts. OPAs are simply optical versions of the familiar RF phased arrays that have been employed since the 1940s [28]. Phased arrays function as a single large effective aperture by coherently interfering the output of multiple subapertures in the far field, allowing the emission angle to be electronically controlled by changing subaperture phases.

OPAs have been previously explored for beam steering, often using optical fibers [29] or liquid-crystal gratings [30]. Coherently combined high energy laser systems, represented in Figure 5, are a type of OPA that have successfully used optical fiber arrays [31]– [34] with fiber-optic lithium niobate modulators, but they remain relatively bulky with discrete commercial components. Liquid-crystal gratings are flexible and low-cost, but have not overcome historically low response time, efficiency, and power limits [35].

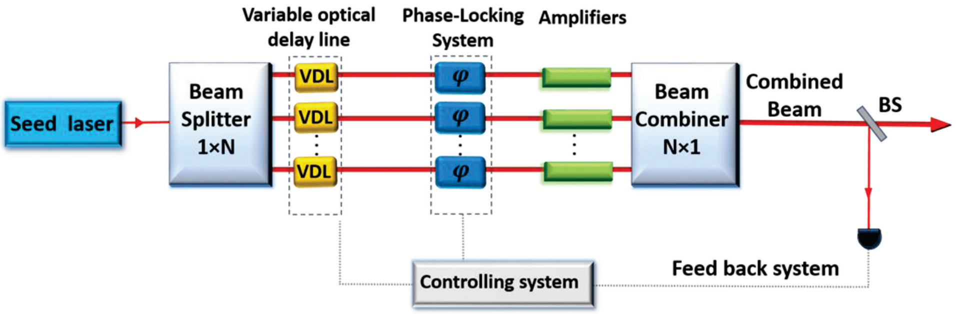

Figure 5: Schematic of coherently combined fiber-optic high energy laser system. Reproduced from [34].

Integrated photonics, on the other hand, is an ideal technology to provide a scalable implementation of OPAs. Several basic components are required for an OPA: a laser source, distribution to multiple channels, phase control, and output coupling. These are all typical components in various PIC platforms, and are exactly those components mentioned in the first 1969 proposal of integrated photonics [18]. Given their capability, the compact size, low weight, and low cost of PICs make them a perfect fit for OPA development, and indeed OPA PICs have been an area of active research for the last decade.

1.3.1 STATE OF THE ART OF INTEGRATED OPAS

A variety of technologies have been investigated for integrated OPAs, including discrete micro-electromechanical system (MEMS) components, arrays of vertical-cavity surface-emitting lasers (VCSELs), lithium niobate on insulator (LNOI) PICs, and silicon photonics (SiPh) PICs. Some of these are shown in Figure 6.

MEMS technology has produced reflection-mode spatial phase modulators arrays of both gratings and mirrors [36], [37]. Relatively immature, they are potentially efficient free-space modulators, but are intrinsically slower than solid state devices. Coherent VCSEL arrays are another emerging field comprising arrays of phased locked integrated lasers [38], [39], and may be an excellent scalable solution if efficiencies are improved. LNOI is a promising high-speed technology using integrated lithium niobate waveguides and modulators, and will be a competitor for dedicated phase modulation applications where gain is not required [40].

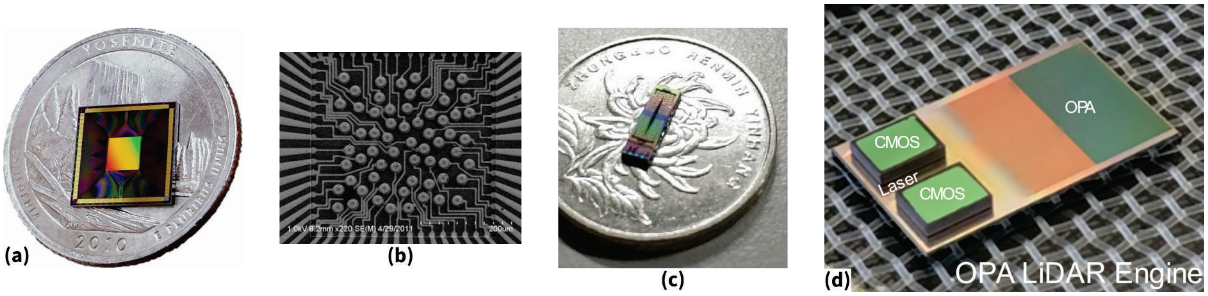

Figure 6: Several existing OPA technologies: (a) Photograph of MEMS OPA system, reproduced from [37]. (b) SEM image of 64-element VCSEL array, reproduced from [39]. (c) Photograph of 8x8 channel SiPh OPA PIC with full phase controlled steering, adapted from [41]. (d) Photograph of 1024 channel SiPh OPA PIC with phase-and-wavelength steering and co-packaged electronics, reproduced from [42].

Most integrated OPA research has focused on SiPh PICs, and several research groups have produced phase-controlled 2D-steerable integrated arrays with 128 individual emitters [41], [43]. Other common designs combine phase and wavelength control, where each parameter actuates one dimension [44]– [48]. This uses the wavelength dependency of reflection gratings so that a single tunable laser entirely controls one dimension, while the other dimension is a typical phased array. The major benefit of this method is high packing density and efficient scaling – with only one direction to extend the array, emitters can be closely spaced while still providing 2D steering, and arrays with over 8000 elements have been demonstrated. Such devices can even provide multiple simultaneous beams by using multiple optical frequencies [49]. The drawback is that the application must accept an operating wavelength that varies with steering angle.

1.4 Gallium Arsenide Photonic Integrated Circuits

While SiPh PICs are a significant improvement over previous OPA methods, and their technology offers significant reductions in cost, size, and weight, SiPh PICs cannot satisfy requirements for some applications. The silicon bandgap limits operation to wavelengths greater than 1100 nm, which excludes the region near 1000 nm that is commonly utilized for topographical and remote-sensing LiDAR [50]– [52]. Crucially for OPAs, the phase modulators available in SiPh platforms are a limiting factor, even compared to traditional methods: thermal phase modulators are restricted to well under 1 MHz modulation speeds with high power dissipation [53], and faster carrier-based phase modulators produce high residual amplitude modulation (RAM) [41], [53]– [55] which reduces beam quality during continuous beamsteering. Alternative modulators for silicon photonics require complex heterogeneous integration techniques involving flip-chip mounting or wafer bonding of other materials. Such techniques have led to several demonstrations of compact and highly functional heterogeneously integrated devices with high speed and low RAM [56], [57], but add manufacturing difficulty and higher loss [54], [58]. These heterogenous integration methods are also required to provide any sort of on-chip gain and lasers for SiPh, since silicon does not have a direct band gap.

In contrast, group III-V compound semiconductor platforms offer native optical gain, well developed lasers, and efficient low-RAM phase modulation mechanisms all on a single material platform. Previously demonstrated OPAs based on III-V compound semiconductors have primarily focused on InP PIC platforms in the 1300 nm and 1550 nm telecommunications wavelength regions. Low power OPAs have been demonstrated on these platforms, some with on-chip gain [59]– [65]. InP PICs are not suitable for shorter wavelengths, however, and as previously discussed typically have high manufacturing costs [66] with smaller and more fragile substrates than Si or GaAs.

GaAs, another III-V material, is the first material system used for room temperature semiconductor lasers [23], [24], and has long been employed to build discrete optical components, especially diode lasers [67]– [69]. While the development of PIC technology has been focused on the InP system due to its support for common telecommunications wavelengths and on SiPh because of the supportive CMOS technology, GaAs fabrication methods have also been matured by the large telecommunications market for VCSELs at 850 nm and quantum dot lasers at 1300 nm, the demand for efficient high power diode lasers near 900 nm, and the wide use of GaAs in high power microwave electronics.

While GaAs clearly offers performant on-chip lasers over a wide wavelength range [70]– [72], it is also a promising material for low-RAM phase modulators operating at wavelengths near 1000 nm because of its strong linear (Pockels) and quadratic electro-optic effects [73]– [77]. These effects allow for deep phase modulation without relying on free carrier effects, enabling efficient low-RAM modulators, and have been previously utilized in discrete GaAs phase modulation devices as far back as 1986 [78], [79].The combination of efficient integrated gain and phase modulation in a single material system enables the possibility of fully monolithic OPA PICs.

1.5 Overview of Dissertation

The focus of this dissertation is on the development of a compact and an efficient OPA platform with steering speeds ≥1 GHz, operational wavelength near 1000 nm, low RAM for continuous beamforming, and integrated gain for high output power. No existing OPA technology meets all of these needs simultaneously. As shown in Figure 7, existing legacy and integrated photonics technologies are insufficient in at least one area.

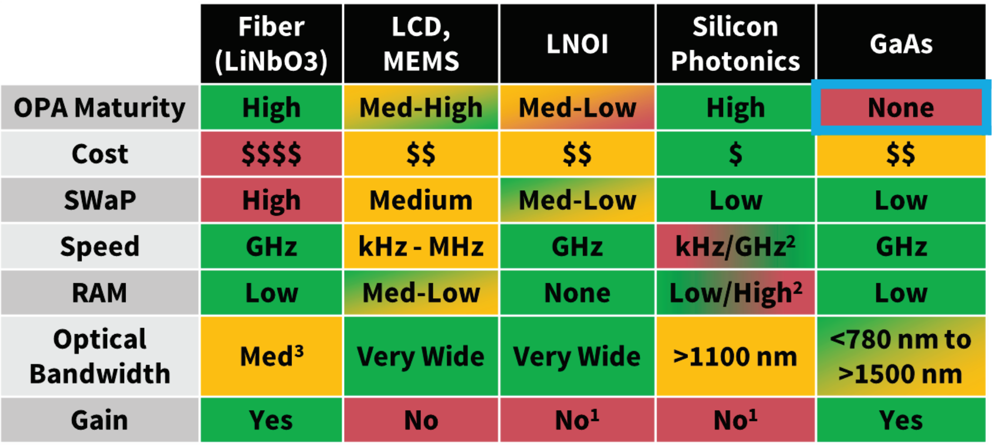

	Fiber (LiNbO3)	LCD, MEMS	LNOI	Silicon Photonics	GaAs
OPA Maturity	High	Med-High	Med-Low	High	None
Cost	$$$$	$$	$$	$	$$
SWaP	High	Medium	Med-Low	Low	Low
Speed	GHz	kHz - MHz	GHz	kHz/GHz[2]	GHz
RAM	Low	Med-Low	None	Low/High[2]	Low
Optical Bandwidth	Med[3]	Very Wide	Very Wide	>1100 nm	<780 nm to >1500 nm
Gain	Yes	No	No[1]	No[1]	Yes

[1] Without III-V integration of some sort

[2] Depends on modulation method

[3] Restricted with gain, very wide if not

Figure 7: Comparison of optical phased array technologies. The focus of this dissertation is outlined in the upper right.

GaAs, however, is an ideal OPA PIC technology that only lacks demonstrated OPA devices and systems. Two discrete GaAs OPAs comprising only the phase modulator array have been previously demonstrated [80], [81], but there are no known reports of fully integrated OPAs on GaAs PIC platforms. This dissertation will thus focus on the development of an OPA PIC platform based on the GaAs material system, demonstrating the technology's suitability for fully integrated monolithic OPAs, and providing a nominal platform that is immediately useful for multiple OPA applications. A schematic diagram of a nominal OPA PIC produced on this platform is shown in Figure 8.

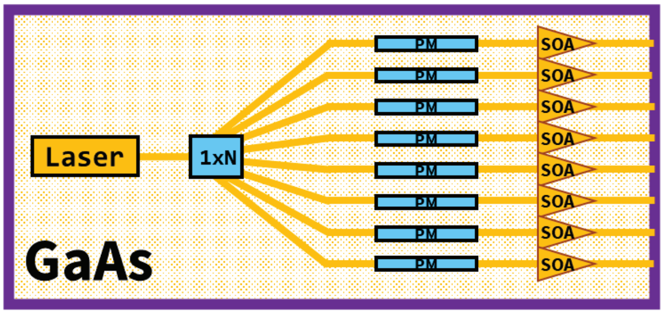

Figure 8: Schematic diagram of nominal fully monolithic OPA PIC platform.

This dissertation is organized into four main sections. Firstly, Chapter 2 presents the known phase modulation effects in GaAs and Chapter 3 describes the research methods used in the remainder of this work. Secondly, the development of all required passive components and their integration into a fully functioning OPA PIC with phase control are described in Chapter 4, demonstrating the suitability of GaAs for OPAs independent of gain. Thirdly, Chapter 5 extends this to include gain in a full active-passive GaAs PIC platform, developing an OPA with both phase control and per-channel gain. Finally, Chapter 6 and Chapter 7 conclude with expectations for future work and a summary of accomplishments.

Chapter 2

Phase Modulation in Gallium Arsenide

GaAs is a promising material for low-RAM phase modulators operating at wavelengths near 1000 nm due to its strong linear (Pockels) and quadratic electro-optic effects. These allow for deep phase modulation without relying on free carrier effects, enabling efficient low-RAM modulators. The details of phase modulation mechanisms in GaAs have been well explored in literature [73]– [77]. Figure 9 shows a dispersion relation of these effects.

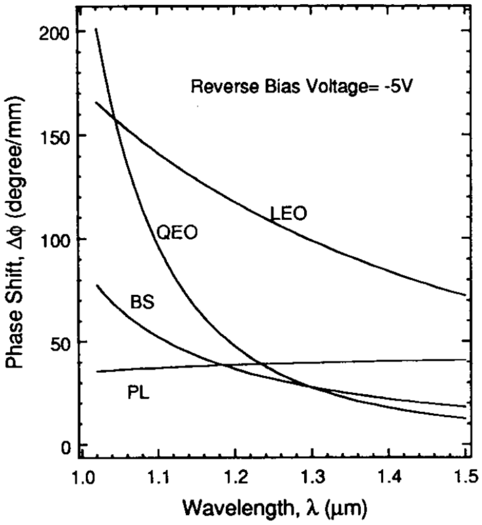

Figure 9: Dispersion relation of phase modulation effects in GaAs for an arbitrary epitaxy. Reproduced from [75].

For accurate prediction of relevant effects in a given GaAs heterostructure waveguide, the index perturbation (Δn) and light absorption (α) effects within a GaAs waveguide are modeled as functions of applied bias (V_{bias}), wavelength (λ or photon energy E_{γ}), and carrier concentrations (N and P).

To provide a full solution, these effects must be applied to a physically modeled system including the waveguide's optical mode, DC electric field distribution, and carrier distribution:

$$\Delta n_{TE} = \frac{\int I(r)\left(\Delta n_{EO}\big(E_j(r)\big)+\Delta n_{FC}\big(N(r),P(r)\big)\right)\mathrm{d}r}{\int I(r)\mathrm{d}r} \tag{2.1}$$

$$\alpha = \frac{\int I(r)\left(\alpha_{EA}\big(E_j(r)\big)+\alpha_{FC}\big(N(r),P(r)\big)\right)\mathrm{d}r}{\int I(r)\mathrm{d}r} \tag{2.2}$$

where $r = \{x, y\}$ is the cross-section dimensions perpendicular to the direction of optical propagation, $I(r)$ is the optical intensity, $\{N(r), P(r)\}$ are the N and P carrier densities, and $E_j(r)$ is the $\hat{z}$ component of the DC electric field.

Potential tools to determine these distributions for physically modeled systems are Lumerical MODE (optical) and Lumerical CHARGE (charge transport) [82], or other similar finite element physics simulation software such as COMSOL [83].

2.1 Assumed System

In this chapter, effects are modeled assuming a p-i-n GaAs epitaxy, with a DC electric field of amplitude $\mathrm{E_j}$ created along the vertical $\hat{z}$ direction (epitaxial surface-normal) by applying a bias V_{bias} across the p-i-n junction, and with light propagating through a waveguide perpendicular to this field. Unless specified, the optical mode in the waveguide is assumed to be the TE polarization with the optical field $\vec{E}_{opt}$ perpendicular to both the propagation direction and DC field across the junction $\vec{E}_j$.

2.2 Definitions

$$E_\gamma = h\nu = \hbar\omega = \text{photon energy}$$

$$E_g = \text{material bandgap; 1.424 eV for GaAs}$$

$$E_j = E_j^1 * (V_0 - V_{bias}) \approx E_j^0 - E_j^1 * V_{bias} = \text{DC electric field amplitude in vertical direction}$$

$$\alpha = \text{power absorption per length, from } P(z) \propto \exp(-\alpha\, \mathrm{z})$$

2.3 Index Perturbation Effects

Index perturbation effects are defined here as:

$$\Delta n = \text{absolute change in refractive index}$$

$$\Delta\phi = \text{phase modulation change} = 2\,\pi\,\Delta n\, L/\lambda$$

2.3.1 LINEAR ELECTRO-OPTIC EFFECT

The linear electro-optic (LEO) effect is also known as the *Pockels effect*, and is a birefringence induced by an external electric field. In GaAs, the index change is given by:

$$\Delta\left(\frac{1}{n^2}\right) = \pm r_{41}\left|E_j\right| \tag{2.3}$$

r_{41} is only nonzero for the TE polarization with an electric field along the $[001]$ direction, and the expression is positive for propagation in the $[110]$ direction and negative in the $[1\overline{1}0]$ direction [77]. From fits to literature values for GaAs as in Figure 10(a), including data from Berseth [76] and Faist [84], a reasonable empirical estimation is:

$$r_{41} = (7.788 - 72.16/n^2) * 10^{-10}\ \mathrm{cm/V} \tag{2.4}$$

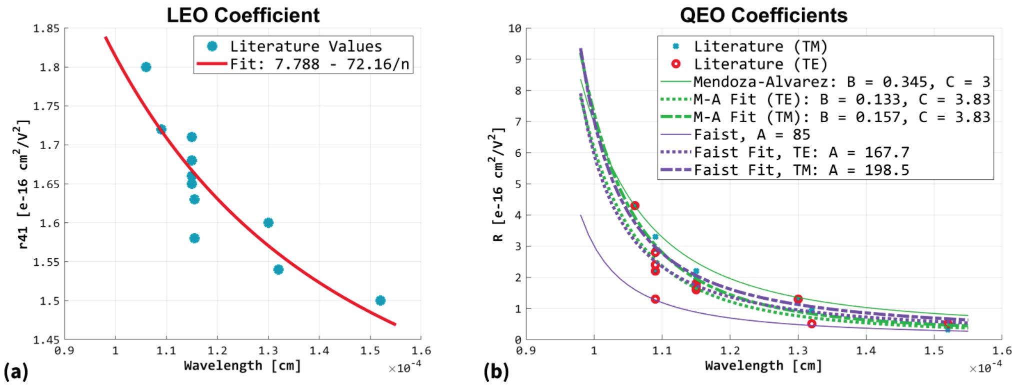

Figure 10: Fit to (a) linear and (b) quadratic electro-optic coefficients from literature values.

2.3.2 QUADRATIC ELECTRO-OPTIC EFFECT

The quadratic electro-optic (QEO) effect is also known as the *Franz-Keldysh* or *band bending* effect. With an applied electric field, the band edges are tilted, increasing the overlap of the electron and hole wavefunctions in the conduction and valence bands, thus increasing the tunneling probability. This shifts the absorption edge to lower energies, or alternatively creates exponential tails in the absorption edge. Via the Kramers-Kronig (K-K) relations, this changes the refractive index below the absorption edge, and can be modeled as a quadratic electric field dependence [73]:

$$\Delta\left(\frac{1}{n^2}\right) = R(\lambda)\left|E_j\right|^2 \tag{2.5}$$

There is a slight polarization dependence reported by some sources [84]. Note that the exact analytical solution via the K-K relations is not quite $\left|E_j\right|^2$ [85].

The dispersion relation reported by Mendoza-Alvarez [73] for GaAs up to 1550 nm is:

$$R(\lambda) = 3.45 \cdot 10^{-17} \cdot \exp(3\ \mu\mathrm{m}^3/\lambda^3)\ \mathrm{cm}^2 \cdot \mathrm{V}^{-2} \tag{2.6}$$

And by Faist [74]:

$$R = \frac{A\,\mathrm{E}_{\gamma}^{2}}{n^{4}\left(E_{g}^{2}-E_{\gamma}^{2}\right)^{2}};\ \mathrm{A} = 85 \cdot 10^{-16}\ \mathrm{eV}^{2}\ \mathrm{cm}^{2}\ \mathrm{V}^{-2} \tag{2.7}$$

Note that these two dispersion relations do not have the same form. These two equations bracket reported values in literature, as shown in Figure 10(b), with fits of either form giving good agreement. As Faist's model only has a single parameter A, that is adopted here for simplicity, with coefficients:

$$A_{TE} = 167.7 \cdot 10^{-16}\ \mathrm{cm}^{2}\ \mathrm{V}^{-2};\ A_{TM} = 198.5 \cdot 10^{-16}\ \mathrm{cm}^{2}\ \mathrm{V}^{-2} \tag{2.8}$$

2.3.3 QUANTUM-CONFINED STARK EFFECT

Relevant for quantum well (QW) systems, the quantum-confined Stark effect is another effect that is also quadratic in E_j. Essentially the same as the *Franz-Keldysh* effect, it is instead applied to the electron and hole wavefunctions confined in a quantum well. There is no general solution – it must be solved with $k{\cdot}p$ (or similar) models and the K-K relation [86]. The Lumerical MQW [82] product can also solve this directly with the "`mqwindex`" command.

As this is not relevant for bulk GaAs systems, it is ignored in the remainder of this dissertation. It is however a potential area of future work for improving phase modulation efficiency per length at the potential cost of higher RAM and EL.

2.3.4 DC KERR EFFECT

The DC Kerr effect is rarely addressed in GaAs. The form is:

$$\Delta n_{Kerr} = \frac{3\,\mathrm{X}^{(3)}\,E_j^2}{2\,n} \tag{2.9}$$

For GaAs, $\mathrm{X}^{(3)} \leq 3 \cdot 10^{-15}\mathrm{cm}^2/\mathrm{V}^2$ at 1030 nm [87]. While nonzero, it is $< 10^{-7}$ the fraction of other EO effects, so it can safely be neglected.

2.3.5 FREE CARRIER EFFECTS

The change of free carrier absorption in the conduction or valence band alters the refractive index via K-K. Index increases when carriers decrease.

From Faist [74], the contributions of intervalence band absorption (FP) and scattering by free carriers (PL) are:

$$\Delta n_{FP} = -2.9 \cdot 10^{-22}\,\frac{P}{E_\gamma^2} \tag{2.10}$$

$$\Delta n_{PL} = -\frac{n}{2}\left(\frac{\nu_p}{\nu_\gamma}\right)^2 \; ; \; \nu_p^2 = \frac{q^2\,\{N,P\}}{\epsilon\, m_{n,p}^*} \tag{2.11}$$

Using the well-known masses [88] of:

$$m_c = 0.063\, m_0, m_{lh} = 0.082\, m_0, m_{hh} = 0.51\, m_0$$

The PL coefficient thus reduces to:

$$\Delta n_{PL} = -\frac{\{N,P\}}{n\, E_\gamma^2}\left(\frac{h^2\, q^2}{8\,\pi^2\,\epsilon_0\, m^*}\right)$$

$$\rightarrow \Delta n_{PL} = -\frac{1}{n\,E_\gamma^2}\,(N \cdot 1.09 \cdot 10^{-20} + P \cdot 1.35 \cdot 10^{-21})\ \mathrm{cm}^3\,\mathrm{eV}^2 \tag{2.12}$$

Comparing to Stern [89] (noted as approximate with up to 50% error by Mendoza-Alvarez [73]), this is similar for N, and also similar for P *if light holes are neglected*. Comparing the result to Faist's total carrier contribution formula (not reproduced here), neglecting light holes seems to be the correct interpretation.

2.3.6 BAND-GAP SHIFT EFFECT

The band-gap shift (BS) effect is composed of a combination of band-gap shrinkage (BGS) and band filling (BF) effects that shift the fundamental absorption edge, thus altering the index via the K-K relation. According to Faist [74] for GaAs at room temperature:

$$\Delta n_{BF} = -2.92 \cdot 10^{-21} \frac{N+P}{E_g^2 - E_\gamma^2} \tag{2.13}$$

$$\Delta n_{BGS} = + \frac{(b_n\, N + b_p\, P)}{E_g^2 - E_\gamma^2} \tag{2.14}$$

$$b_n = 8.9 \cdot 10^{-22}\ \mathrm{cm}^3\ \mathrm{eV}^2,\ b_p = 1.42 \cdot 10^{-21}\ \mathrm{cm}^3\ \mathrm{eV}^2$$

Compared to Lee [75] near 1000 nm, the n-type coefficients are similar, but p-type coefficients differ by 3x. This discrepancy is noted by Lee *et al*.

2.4 Total Index Perturbation

2.4.1 ELECTRO-OPTIC EFFECTS

Considering only the LEO and QEO effects,

$$\Delta\left(\frac{1}{n^2}\right) = \left(\frac{1}{n+\Delta n_{EO}}\right)^2 - \left(\frac{1}{n}\right)^2 = \pm r_{41}\left|E_j\right| + R\left|E_j\right|^2 \tag{2.15}$$

$$\rightarrow \Delta n_{EO} = n\left(\frac{1}{\sqrt{1+n^2\left(r_{41}\left|E_j\right|+R\left|E_j\right|^2\right)}} - 1\right) \tag{2.16}$$

Expanding quadratically in E_j and discarding higher order r_{41} and R terms:

$$\Delta n_{EO} \approx -\frac{n^3}{2}\left(\pm r_{41}\left|E_j\right| + R\left|E_j\right|^2\right) \tag{2.17}$$

However, due to the built-in bias, the electric field is $E_j \approx E_j^0 + E_j^1 * V_{bias}$. Expanding to quadratic V_{bias} and discarding higher order r_{41} and R terms:

$$\Delta n_{EO} \approx -\frac{n^3}{2}\left(\left(\pm r_{41}\, E_{j0} + E_{j0}^2\right) + \left(\pm r_{41} + 2\, R\, E_j^0\right)\left(E_j^1\, V_{bias}\right) + (R)\left(E_j^1\, V_{bias}\right)^2\right) \tag{2.18}$$

$$r_{41} = (7.788 - 72.16/n^2) \cdot 10^{-10}\ \mathrm{cm/V}$$

$$\mathrm{R} = \frac{A\, E_\Upsilon^2}{n^4\left(E_g^2 - E_\Upsilon^2\right)^2},\ A_{TE} = 167.7 \cdot 10^{-16}\ \mathrm{cm}^2\ \mathrm{V}^{-2},\ \mathrm{A}_{TM} = 198.5 \cdot 10^{-16}\ \mathrm{cm}^2\ \mathrm{V}^{-2}$$

Note that the linear-in-V_{bias} term now also depends on R – so the linear term will both be higher than naively expected, and will be nonzero for TM modes.

2.4.2 FREE CARRIER EFFECTS

Simply summing the FP, PL, and BS effects,

$$\Delta n_{FC} = D_n\, N + D_p\, P \tag{2.19}$$

With coefficients:

$$D_n = -\left(\frac{1.09\cdot 10^{-20}}{n\, E_\gamma^2} + \frac{2.03\cdot 10^{-21}}{E_g^2 - E_\gamma^2}\right) \text{ eV}^2 \text{ cm}^3 \tag{2.20}$$

$$D_p = -\left(\frac{2.9\cdot 10^{-22}}{E_\gamma^2} + \frac{1.35\cdot 10^{-21}}{n\, E_\gamma^2} + \frac{1.50\cdot 10^{-21}}{E_g^2 - E_\gamma^2}\right) \text{ eV}^2 \text{ cm}^3 \tag{2.21}$$

More detailed calculations are performed by Huang [90], [91] at nearby wavelengths, but with nontrivial formulas involving band-structure integrations.

2.5 Optical Absorption Effects

Two major sources of absorption are important for modeling phase modulators in GaAs: free carrier absorption, present where the optical field overlaps free carriers, and electroabsorption from the Franz-Keldysh effect, where the DC electric field across the p-i-n junction bends the bands, shifting the absorption edge closer to the operating wavelength. These both vary with the applied bias, causing RAM.

2.5.1 FREE CARRIER ABSORPTION

The simple Drude model for free carrier absorption is [92]:

$$\alpha_{FC} = \frac{q^3\, h^2\, N}{4\pi^2\, \mu\, (m^*)^2\, n\, \epsilon_0\, c\, E_\gamma^2} \tag{2.22}$$

Good empirical electron mobility fits are available from Sotoodeh Table 1 [93]:

$$\mu(N,T) = \mu_{min} + \frac{\mu_{max}\,(300\text{ K}/T)^{\theta_1} - \mu_{min}}{1+\left(\frac{N}{N_{ref}\,(T/300\text{ K})^{\theta_2}}\right)^{\lambda}} \tag{2.23}$$

For GaAs at 300 K, neglecting heavy holes (~1/40th), this evaluates to:

$$\mu_N = \left(500 + \frac{8900}{\left(1+\left(\frac{N}{6*10^{16}}\right)^{0.394}\right)}\right)\text{ cm}^2\text{ V}^{-1}\text{ s}^{-1} \tag{2.24}$$

$$\mu_P = \left(20 + \frac{471.5}{\left(1+\left(\frac{N}{1.48*10^{17}}\right)^{0.38}\right)}\right)\text{ cm}^2\text{ V}^{-1}\text{ s}^{-1} \tag{2.25}$$

$$\alpha_{FC} = \frac{8.1\cdot 10^{-17}}{E_\gamma^2}\left[\text{eV}^2\text{ cm}^4\text{ V}^{-1}\text{ s}^{-1}\right]\left(\frac{N}{0.063^2\cdot\mu_N(N)} + \frac{P}{0.082^2\cdot\mu_P(P)}\right) \tag{2.26}$$

2.5.2 DOPING LOSS DATA

Alternatively, it may be possible to use an empirical fit to doped-GaAs material loss instead of the Drude model. It is unclear if the loss from the doping is directly connected to free carrier absorption, as sources of the data disagree: Spitzer [94], Johnson [95], and Babic [96] indicate the measured loss from doped GaAs is due to free carrier absorption, but Turner [97] indicates most is **not** free carrier absorption, especially P-type.

Regardless of the cause, it seems reasonable that absorption effects due to carrier concentration can be taken from these sources of empirically measured data [94]– [99]. A good empirical fit is presented in section 3.1.1 and equation 3.2.

Compared to the Drude model, the doped absorption loss is generally significantly lower, by a factor of 0.8-6 for n-type and 2.5-10 for p-type. The p-type scaling is similar between both, while the Drude model's n-doped scaling is higher with respect to N and λ.

Overall, additional test data is needed to determine which model is more appropriate.

2.5.3 ELECTROABSORPTION

Electroabsorption is from the same Franz-Keldysh effect responsible for the QEO index perturbation. Due to band bending, the effective bandgap is shifted closer to the operating wavelength, resulting in increased optical absorption at higher bias.

A simple parabolic band approximation from Tharmalingam and Callaway via Mendoza-Alvarez [73] and Alping [85], with units of eV and cm, is:

$$\alpha_{EA} = \sum_j A_j \left|E_j\right|^{1/3} \left(\text{AiryAi}'\left(\beta_j\right)^2 - \beta_j \, \text{AiryAi}\left(\beta_j\right)^2 \right) \tag{2.27}$$

$$\beta_j = B_j \left(E_g - E_\gamma\right) \left|E_j\right|^{-2/3};\ A_j = \frac{7.65 \cdot 10^5}{n\, E_\gamma} \left(2\mu_j/m_0\right)^{4/3};\ B_j = 1.1 \cdot 10^5 \left(2\mu_j/m_0\right)^{1/3}$$

$$j = lh, hh;\ \mu_{lh} = 0.0369\, m_0,\ \mu_{hh} = 0.0583\, m_0$$

Alping [85] multiplied the result by 1.30 to obtain agreement with measurements, and Bennett [100] has more complex calculations involving nonparabolic band structures. Hagn [101] presents a detailed derivation and measurement of the Franz-Keldysh effect’s phase and absorption dispersion, which matches other models in literature.

2.5.4 COMPARISON TO DATA

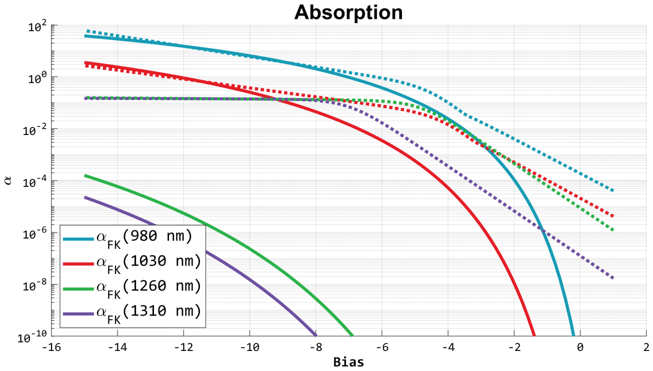

Figure 11: Theoretical Franz-Keldysh electroabsorption (solid) compared to RAM data from section 4.8 (dotted), presented for several different wavelengths. The theoretical values are scaled by $1.2 \cdot 10^{-4}$.

Compared to measured $\alpha(V_{bias})$ data presented later in section 4.8, this model describes high-bias absorption very well at ≤1030 nm wavelengths, and decently well above that. However, scaling is a problem. At 1030 nm, a very good fit has a scaling factor of $1.2 \cdot 10^{-4}$ as seen in Figure 11; compare this to Alping's scaling of 1.3, and the 10^{-4} can possibly be accounted for by mistaken unit scaling. Unfortunately, this still underpredicts 980 nm loss and severely underpredicts >1030 nm loss. It is likely that the absorption at longer wavelengths is not Franz-Keldysh electroabsorption, so the apparently incorrect scaling at longer wavelengths can be neglected. It is also likely that other absorption effects are stronger at 980 nm – and the measured shapes do bear that out. Additionally, since this is a complicated function, the scaling factor is potentially present in a different coefficient; this has not been investigated.

For use in this work, the simple parabolic band approximation with a $1.2 \cdot 10^{-4}$ scaling factor appears to be the best predictor of near-1000 nm electroabsorption loss.

2.5.5 MQW SYSTEMS

For multiple-quantum-well (MQW) systems, full $k{\cdot}p$ or similar models are needed to determine optical absorption [86]. The Lumerical MQW [82] product can solve this directly with the "`mqwindex`" command. This is further discussed in section 3.1.4.

2.6 Chapter Summary

Chapter 2 has reviewed literature reports for relevant phase modulation effects in GaAs, and presented detailed equations for the modeling the phase modulation $\Delta\phi$ and amplitude modulation α effects. These assume a p-i-n GaAs epitaxy, with a DC electric field of amplitude $\mathrm{E_j}$ along the vertical created by applying a bias V_{bias} across the p-i-n junction, and with light propagating through a waveguide perpendicular to this field.

These equations will be used throughout the rest of this dissertation to provide expected or simulated values for the phase modulation of assorted epitaxial structures given an optical field and electric field.

Chapter 3

Research Methods

A variety of tools and methods have been utilized to develop the reported PIC platforms. These consist of software tools for simulation and lithographic mask layout, processing methods and tools for fabrication, and software tools combined with physical hardware systems for device testing. Descriptions of the primary components of these are reported in this chapter, and are referenced in later chapters when reporting results.

3.1 Simulation

3.1.1 OPTICAL MODES

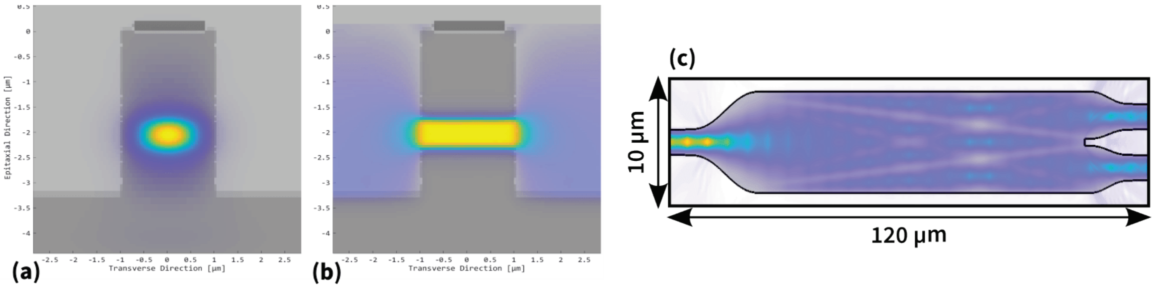

Figure 12: (a) Simulated fundamental TE optical mode of modulator and passive waveguides (color) and waveguide structure (shaded grey). (b) Simulated electrical field of the same structure under reverse bias. (c) Simulated optical mode of 1x2 MMI splitter.

Epitaxial and waveguide optical modes were simulated with the commercial Lumerical MODE software, and waveguide components and devices such as MMI splitters and waveguide bends were simulated with both Lumerical FDTD and the 2.5D “varFDTD” solver available in Lumerical MODE [82]. Lumerical and MATLAB scripts were used to assemble and analyze simulations and their results [102], with typical modal simulation results shown in Figure 12(a) and FDTD propagation results for an MMI splitter shown in Figure 12(c).

The optical index and loss used in these simulations were determined from extensive literature investigations. For computational and implementational simplicity, data and physically derived equations from literature were fit in relevant wavelength ranges by simplified empirical equations.

The optical index of $Al_xGa_{1-x}As$ was determined from the physically derived description determined by Gehrsitz [103] and separately by Adachi [104], as well as measurements from Aspnes [105] and Papatryfonos [106]. Fitting was restricted to 300K and wavelengths between the bandgap and 1800 nm, with aluminum content x ranging from 0% to 50%. Over this region, it is well described by a simple 3-parameter Sellmeier equation in wavelength and cubic equation in x, shown in Figure 13:

$$n_{\text{AlGaAs, 300K}} = \left(3.461 + \frac{3.352\,\lambda^2}{\lambda^2 - 0.09152}\right)\left(0.4868 - 0.06087\,x + 0.05807\,x^2 - 0.08842\,x^3\right) \quad (3.1)$$

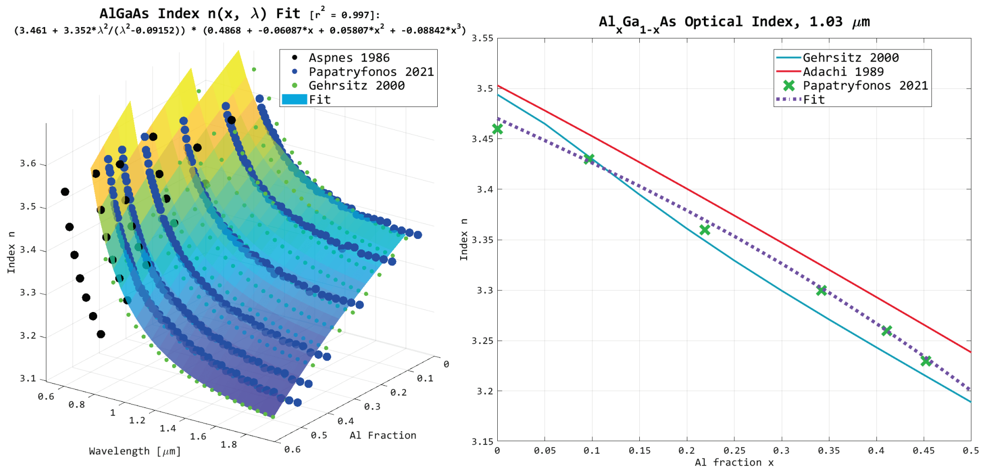

Figure 13: Fit of AlGaAs index at 300K to physically derived Gehrsitz equation and data from Aspnes and Papatryfonos.

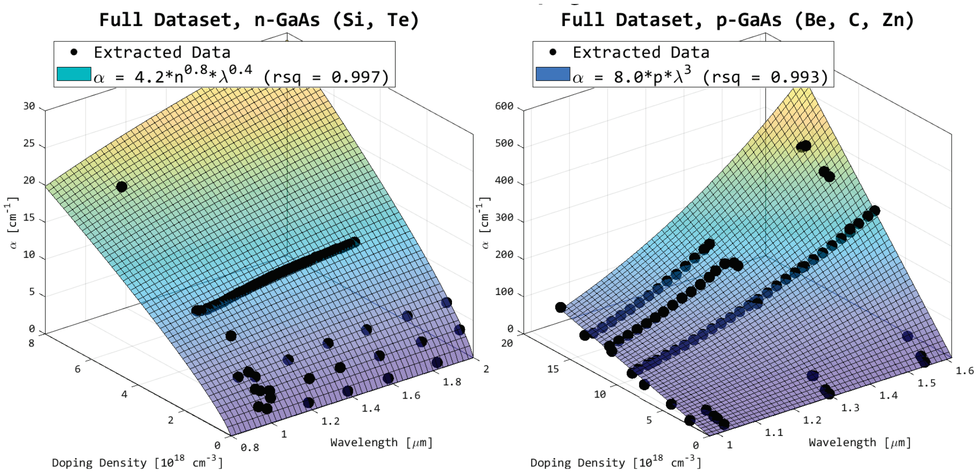

Figure 14: Empirical fit to literature data of GaAs optical absorption as a function of doping densities.

The optical loss of GaAs at various p and n doping levels was determined from consistent data in literature [94]– [99], as shown in Figure 14. A simple power-law empirical fit was used for implementation:

$$\alpha_{GaAs} = 4.2\,\mathrm{cm}^{-1}\left(\frac{N}{10^{18}\,\mathrm{cm}^{-3}}\right)^{0.8}(\lambda/\mu\mathrm{m})^{0.4} + 8\,\mathrm{cm}^{-1}\left(\frac{P}{10^{18}\,\mathrm{cm}^{-3}}\right)(\lambda/\mu\mathrm{m})^{3} \tag{3.2}$$

Consistent descriptions of the optical loss of AlGaAs at various doping levels were unable to be found in literature. Instead, an approximate scaling compared to GaAs is used by assuming the free-carrier scaling approximation:

$$\alpha_{FCA} \propto \mu^{-1}\,\mathrm{m}_{\mathrm{eff}}^{-1}\,\mathrm{n}^{-1} \tag{3.3}$$

Effective masses are available from Adachi [107], and hole mobility as a function of N and P is described simply in Sotoodeh [93], but AlGaAs electron mobility is difficult due to the crossover from a direct bandgap to indirect bandgap at around 40% aluminum content. Sotoodeh presents a more complex function for the electron mobility of doped AlGaAs obtained by scaling the electron mobility of UID AlGaAs by the same function as GaAs, with the doping reference point being changed to a power interpolation between GaAs and AlAs.

For use in calculations this requires a formula for the UID AlGaAs electron mobility; while Sotoodeh does not describe the function used, a reasonable fit to experimental data as a function of x for UID $\mathrm{Al_xGa_{1\text{-}x}As}$ [108] is obtained by a rational fit:

$$\mu_{\mathrm{e}} = 10^{\frac{8.76\,\mathrm{x}^2 - 8.73\,\mathrm{x} + 2.27}{\mathrm{x}^3 + 1.51\,\mathrm{x}^2 - 2.1\,\mathrm{x} + 0.592}} \tag{3.4}$$

Using the electron and hole mobility as a function of x and doping levels, the effective masses, and the relative optical indices obtained earlier, the FCA approximation provides a scaling function to generate approximate $\mathrm{Al_xGa_{1\text{-}x}As}$ optical absorption proportional to GaAs optical absorption. As the N and P scaling functions are very complex with dozens of terms, yet are based on relatively simple assumptions that are not expected to give exact results, the actual implementation is provided by simpler empirical fits to the FCA scaling to improve readability and potential errors transferring the results between code bases. Fit error was under 50% for N and under 10% for P:

$$\frac{\alpha_{\mathrm{AlGaAs}}(\mathrm{x,N})}{\alpha_{\mathrm{GaAs}}(\mathrm{N})} = \left(\frac{2.83\,x^2 - 1.935\,x + 0.363}{x^2 - 1.04\,x + 0.276}\right)(1 - 0.082\ \log_{10}(N)) \tag{3.5}$$

$$\frac{\alpha_{\mathrm{AlGaAs}}(\mathrm{x,P})}{\alpha_{\mathrm{GaAs}}(\mathrm{P})} = 1 + 1.71\ e^{-9.5\,(x-0.6)^2}\left(1 + \frac{(\log_{10} P)^2}{11.9} + \frac{(\log_{10} P)^3}{25} + \frac{(\log_{10} P)^4}{200}\right) \tag{3.6}$$

As these values are for use in optical mode simulations that are primarily for estimating *comparative* optical loss between designs, the uncertainty and error present in the AlGaAs optical loss fit was deemed acceptable.

The optical indices of other materials were generated from fits of literature data in a similar manner, but the results are not shown here. These materials include aluminum oxide (AlOx), InGaP, InGaAsP, Si_3N_4, SiO_2., and $LiNbO_3$. Optical loss was not determined for these materials, although for comparative simulation purposes the optical loss for InGaP and InGaAsP was set to the same as GaAs. Very few designs included AlOx or InGaP, and InGaAsP was only included in 50-nm-thick MQW structures, so the lack of accurate optical loss data for these materials was expected to have negligible impact on the design process.

3.1.2 ELECTRIC FIELDS

Electrical charge-transport simulations were used to determine carrier distributions and electric fields for phase modulator p-i-n junctions under reverse bias. These simulations were performed with the commercial Lumerical CHARGE software [109]. A combination of Lumerical and MATLAB scripts were used to assemble and analyze these simulations [102], with a typical result shown in Figure 12(b).

3.1.3 PHASE MODULATION

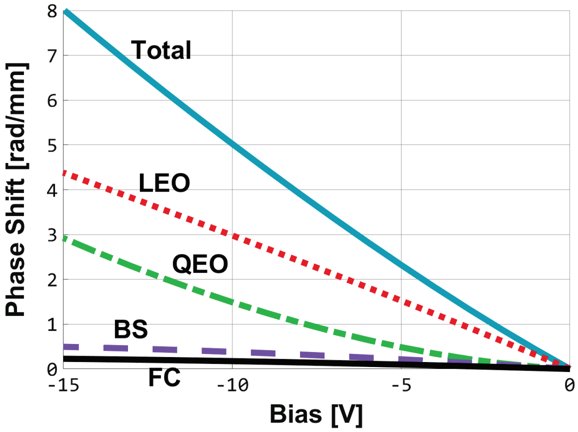

Figure 15: Phase modulation calculation from opto-electrical simulation results showing expected modulation at 1030 nm (cyan) for the modulators specified in Chapter 4, including contributions from linear electro-optic (LEO, red, dotted), quadratic electro-optic (QEO, green, dot-dashed), bandgap shift (BS, purple, dashed), and free carrier plasma (FC, black) effects.

The expected performance of GaAs-based phase modulators was calculated by applying the well-known effects summarized in Chapter 2. These were implemented with MATLAB code [102], which also combined the optical and electrical simulation results. For the optical and electrical fields shown in Figure 12(a,b), which is a 2-μm-wide phase modulating waveguide with the epitaxy specified in Chapter 4 simulated at 1030 nm wavelength, the phase modulation calculations predict 4.98 rad/mm TE phase modulation and 0.086 dB/mm RAM at -10 V bias. This changes to 8.08 rad/mm and 1.17 dB/mm at -15 V bias. Since all effects are modeled, the individual contributions can easily be determined;

Figure 15 presents the contributions of all modeled phase modulation effects for this structure.

3.1.4 ACTIVE DEVICES

The expected performance of both lasers and semiconductor optical amplifiers (SOAs) was modeled for the design of the active-passive OPA PIC described in Chapter 5. This first required modeling the MQW active regions.

Modeling and simulation of isolated InGaAs/GaAsP MQW structures was accomplished with the commercial Lumerical MQW tool [82] which performs full $k \cdot p$ calculations, and the results were checked against photoluminescence (PL) peak calculations from a spreadsheet implementation of the model presented in [110] for strained InGaAs/InGaAsP quantum wells. Figure 16 shows the results of a Lumerical MQW calculation for the epitaxy that is described in Chapter 5, including strain assuming a GaAs substrate.

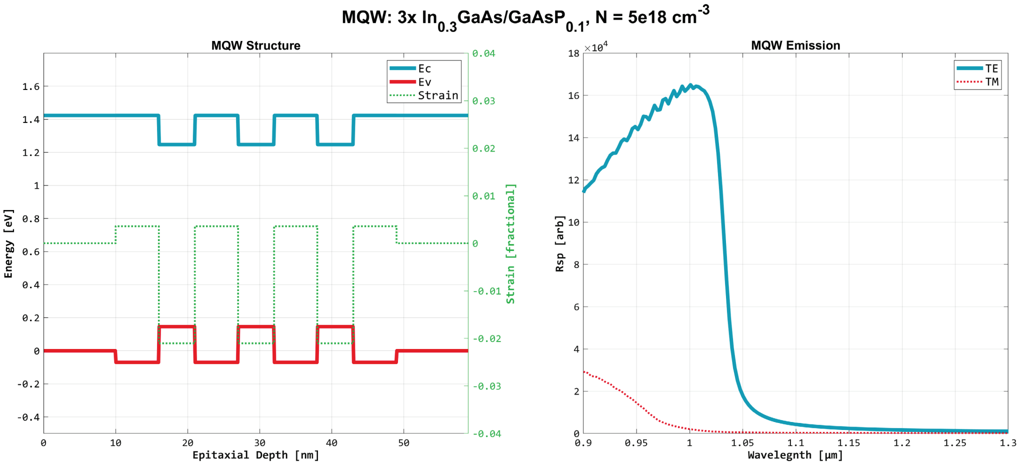

Figure 16: MQW simulation results for the epitaxy from Chapter 5, including the band structure (left) and strain (left, dotted green), and the spontaneous emission spectrum (right) at an arbitrarily-selected 5e18 cm^{-3} carrier density.

These MQW results were used to estimate SOA performance. To provide material gain estimates for SOA simulations, emission spectra were computed for the selected MQW structure at a variety of carrier densities. These results were also reduced to single-QW-equivalent material gain curves for flexibility in changing the number of quantum wells during SOA performance exploration. As shown in Figure 17, simulating the spectra at varying carrier densities produces a full 2D dataset that can provide the material gain as a function of both wavelength and carrier density.

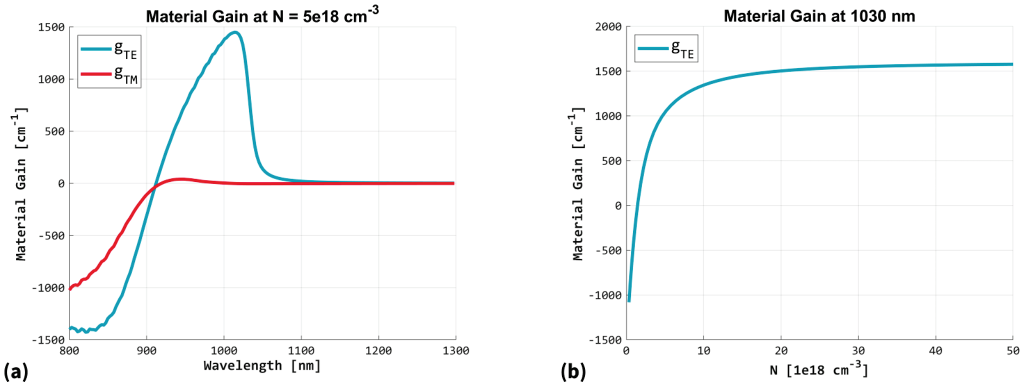

Figure 17: Single quantum well material gain as determined from Lumerical MQW simulation, displayed at (a) fixed number density, and (b) fixed wavelength.

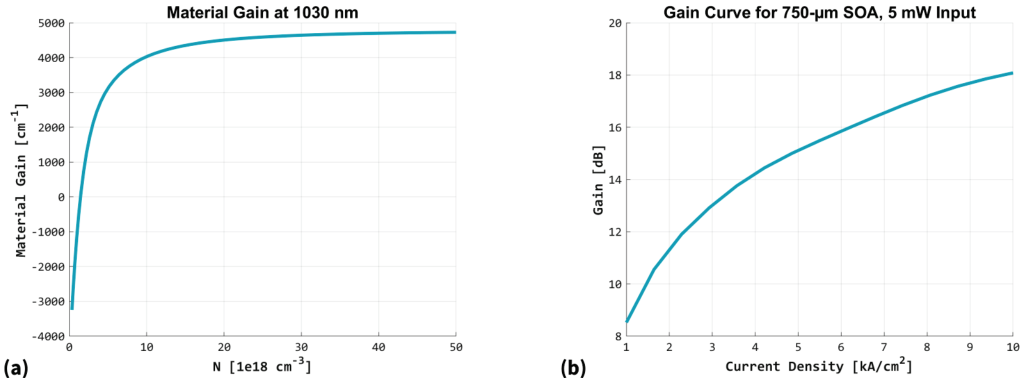

Figure 18: Inputs and results from SOA simulations, showing (a) assumed material gain for a given wavelength and 3 QW configuration, and (b) resulting gain curve assuming 5 mW input and 750 μm device length.

Performance was then calculated for specific SOA configurations with parameters including operating wavelength, effective electrical width estimated from device rib width, number of quantum wells (N_{qw}), device length, input power, and the gain overlap and passive loss provided by optical mode simulations of specific epitaxies. This performance calculation involved several steps. First, the material gain for the particular wavelength and N_{qw} is interpolated from the previous MQW results, as shown in Figure 18(a).

Secondly, the standard rate equations for semiconductor gain [111] are interpreted for the particular situation of single-pass SOA gain with a time-step and distance-step calculation method, resulting in coupled differential equations and associated definitions:

$$dN_c = dt\left(\frac{J}{q\,d} - A\,N_c + B\,N_c^2 + C\,N_c^3 - g\left(N_c, N_p\right)v_g\,N_p\right) \tag{3.7}$$

$$dN_p = \left(dt\,v_g\right)\,\left(N_P\left(\Gamma\,g\left(N_c, N_p\right) - \alpha_i\right) + \Gamma\,g_{sp}(N_c)\right) \tag{3.8}$$

$$g\left(N_c, N_p\right) = \frac{g(N_c)}{1+\epsilon\,N_p} \tag{3.9}$$

$$P\left(N_p, \Gamma\right) = Np\;h\nu\;v_g\;w\;d\;/\;\Gamma \tag{3.10}$$

N_c = carrier density, N_p = photon density

$g(N_c)$ = stimulated material gain, $g_{sp}(N_c)$ = spontaneous material gain

J = current density, α_i = intrinsic propagation loss

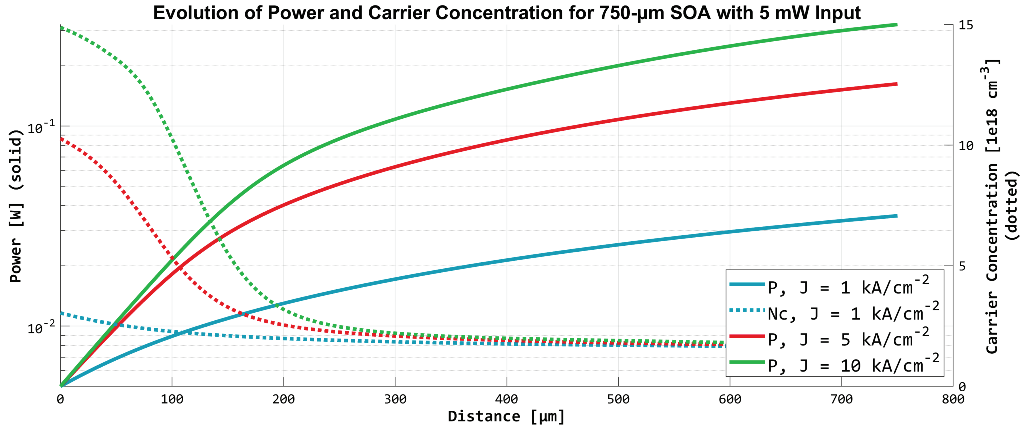

Figure 19: Longitudinal SOA simulation along the length of the device, showing both optical power (left y-axis, solid lines) and carrier density (right y-axis, dotted lines) for different input current conditions.

Typical values for $In_{0.2}Ga_{0.8}As$ QWs from [111] are used for the nonradiative recombination and gain compression coefficients in equations 3.7 and 3.9. These equations are then solved iteratively. Assuming constant J and P_{in} and unidirectional propagation, the length of the SOA is discretized into small distance steps, which are also inherently timesteps via the group index of refraction v_g. Starting at the SOA input, N_c is solved for $N_p(P_{in})$ via nonlinear numerical methods, then N_p is calculated for the next time-and-distance step, inherently propagating forward. This process is repeated until the end of the SOA is reached, resulting in predicted longitudinal evolutions of the power and carrier density as shown in Figure 19. By performing this process for multiple current densities, a gain curve such as Figure 18(b) is assembled by examining the power at the end of the SOA length. This numerical solution method can readily be applied to many different SOA configurations, enabling rapid exploration of the available SOA design tradeoffs.

Laser performance, in comparison, was simulated in a simpler manner. For a given material gain, intrinsic loss, N_{qw}, MQW overlap, wavelength, current density, and geometry, the left and right mirror complex reflectivities are calculated using the transmission matrix method as described in [111]. This is performed at a range of current densities to find the threshold current where $R = |r_L \cdot r_R| = 1$, as well as the spectrum and from that the side-mode suppression ratio. Figure 20 shows one such reflectivity and cavity mode spectrum for an arbitrarily selected laser simulation.

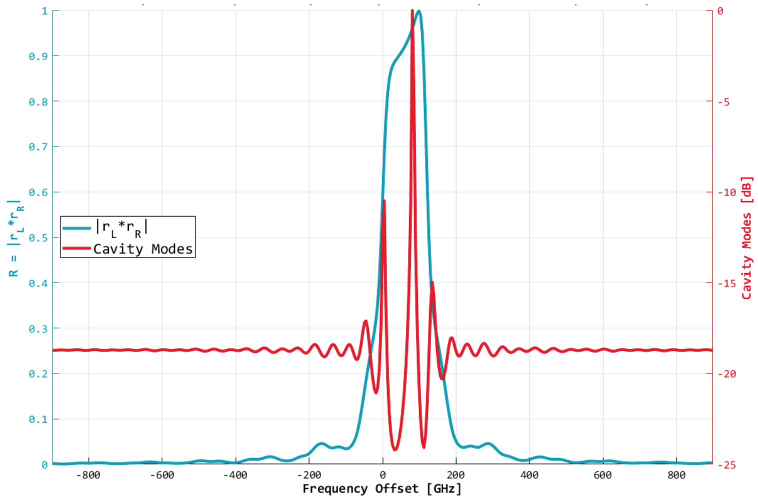

Figure 20: Example reflectivity (blue) and cavity mode spectrum (red) simulation for a specific laser geometry and parameter selection.

The difficulty in this method was primarily the determination of appropriate transmission matrices for nontrivial geometry. Gain-coupled DFB gratings were calculated via the standard uniform-propagation transmission matrices with complex gain and loss, and confirmed via Lumerical EME [82] simulation. Vertically coupled grating unit cell reflections were simulated directly with Lumerical EME. Laterally coupled gratings were calculated via a more complex discretized transmission matrix calculation on lithographically simulated geometry. More details are discussed in section 5.6.

3.2 Lithographic Mask Layout

Lithographic masks define the geometry of the PICs by determining which areas of the die are exposed to or protected from the subsequent etch steps. Devices and waveguides are constructed by careful arrangement of multiple masks, so the design of these is critical for proper PIC functionality after fabrication. The process of assembling or defining the geometry of a mask is known as “mask layout”, the laying-out of multiple geometrical components to form a full mask. These masks are typically specified in the GDSII (.gds) geometry file format, but may also be in the more modern Oasis (.oas) format.

All PICs presented here were laid out using a combination of the open-source “Nazca design” [112] Python-language layout library combined with custom utility functions and custom Nazca PDKs [113] created for the specific epitaxies and processes developed in this work. Nazca design generates GDSII files from mask layer and geometry specifications written in the Python programming language. The custom utility functions and PDKs were used to define common waveguide cross-sections, components, and devices customized for the specific epitaxies and processes involved.

3.3 Fabrication

All device fabrication presented in this dissertation was performed in the UCSB Nanofabrication facility [114], a state-of-the-art research fabrication facility for micro and nano-scale processing. The UCSB NanoFab provides a wide variety of equipment and processing facilities for researcher use, which is sufficient for nearly all processing steps of PIC fabrication. Some postprocessing was performed elsewhere; namely, a commercial vendor provided AR coating and device singulation, wire bonding and soldering was performed in the optical test laboratory, and the MOCVD regrowth in Chapter 5 was performed in a different UCSB facility.

Fabrication processes were conceptually developed in concert with mask layout arrangement and waveguide structure simulations, and were typically prototyped as simple schematic diagrams before the exact physical implementations were determined. The final detailed descriptions of all steps required for processing, so-called “process travelers,” were generated and maintained as Excel spreadsheets or Markdown documents. These process travelers include details such as the methods and ordering of cleaning samples, lithographic recipes and development times, and detailed etch recipes.

Several classes of tools are especially relevant to the fabrication processes developed in this dissertation. These include tools for dielectric deposition, lithography, dry etching, inspection, metal deposition, and wire bonding.

3.3.1 DIELECTRIC DEPOSITION

The UCSB NanoFab has several plasma enhanced chemical vapor deposition (PECVD) tools to deposit dielectric films, named PECVD1, PECVD2, and Unaxis PECVD, with the last being an inductively coupled plasma (ICP) enhanced PECVD process. PECVD1 was most frequently used throughout this work, and is a reliable tool that deposits acceptable quality films. However, the stress of these films tends to be higher, and spalling has been observed under heating. For the best quality films, the Unaxis ICP-PECVD tool should be used. The drawback of this tool is its unreliability, as it frequently experiences errors or is down for maintenance, and it also requires slower and less straightforward operation.

3.3.2 LITHOGRAPHY

The UCSB NanoFab has three relevant lithography systems: a GCA Autostep 200 i-line stepper with 0.8-1.0 μm effective resolution, a Heidelberg MLA150 maskless aligner with ~1.0 μm resolution, and an ASML 5500 deep UV stepper with ~200 nm resolution. The MLA150 was generally preferred over the GCA Autostep 200 for layers that did not require higher smoothness, as it is simple and fast to operate and does not require mask plates fabricated in advance. However, it generally presents a rougher lithographic result. This may possibly be ameliorated through further lithographic process development including exposure conditions, development time, and post-development reflow, but was not solved during this work. The ASML stepper provides the best quality lithography, but requires expensive masks and can only process full 4” wafers, so it has not been used in this work.

3.3.3 DRY ETCHING

Three different dry etching tools capable of inductively coupled plasma reactive ion etching (ICP-RIE) were used in this work, referred to as the Fluorine ICP, Oxford ICP, and Panasonic ICP #1. The Fluorine ICP was used for etching of dielectric films via CHF_3/CF_4 chemistry, and a recipe for this was developed and optimized. The Oxford ICP and Panasonic ICP #1 were used for dry etching of III-V compounds, primarily with Cl_2/N_2 chemistry. The Oxford ICP is a fast and repeatable system, but radial nonuniformity across the surface of samples has been observed, as well as high sensitivity to exposed etch area, likely due to the small etch chamber size. The Panasonic ICP #1 produces uniform etches regardless of exposed etch area, but has significant day-to-day variability in etch process results, possibly due to both the variety of different chemistries used with the tool as well as the frequent maintenance it requires.

3.3.4 INSPECTION

The UCSB NanoFab has two scanning electron microscopes (SEMs) and multiple optical microscopes, all of which were frequently utilized in this work to verify process results. A digital optical microscope was also used to produce mosaic images of final samples for whole-sample digital optical inspection.

3.3.5 METAL DEPOSITION

Several electron-beam (E-beam) thermal evaporation deposition tools are available in the UCSB NanoFab, with E-beams #1 and #3 utilized by this work. E-beam #3 possesses a load lock for quick pump-down, and stocks a wide variety of metals, but can only deposit at normal incidence. This is excellent for uniform metal deposition on a flat surface. E-beam #1 allows for an angled and rotating sample chuck, enabling uniform deposition on high-relief surfaces. A combination of the two systems was often used for depositing metal, with a base layer deposited via E-beam #3 followed by a thick E-beam #1 deposition on an angled and rotating chuck to ensure coverage of waveguide sidewalls.

3.3.6 WIRE BONDING AND SOLDERING

Wire bonding was performed with a manual ball-bond tool located in the optical testing laboratory. Soldering was performed on a co-located manual pick-and-place tool.

3.4 Characterization

Several different techniques were necessary to fully characterize the devices produced during this work. Primary measurements were the phase modulation efficiency of individual phase modulators, the electrical characteristics of all devices including leakage current, the performance of entire OPA devices, and the performance of individual SOAs. All of these measurements were performed in the UCSB optical testing laboratory except for OPA performance evaluation, which was characterized at an MKS-ESI facility.

3.4.1 FABRY-PEROT CHARACTERIZATION

To determine optical propagation loss, a common technique is to create a Fabry-Perot (FP) cavity out of a waveguide and measure the cavity fringes while the effective optical path length is changed [115]. If the FP cavity contains an internal phase modulator to change the effective path length, the full Airy transmission function of a FP cavity with two facets of equal reflectivity R and internal phase difference ϕ can describe the modulator-added phase modulation $\phi_{mod} = \phi - \phi_0$. In this case, the transmitted power fraction is:

$$P_{FP} = \frac{(1-R)^2\, e^{-\alpha_i L}}{1+R^2 e^{-2\,\alpha_i L} - 2\,R\,e^{-\alpha_i L}\cos(2\,\phi)} \tag{3.11}$$

Simplifying this to normalize over the $\phi = 0$ value,

$$\frac{P_{FP}}{P_{FP}(\phi=0)} = P_{norm} = \frac{\left(e^{\alpha_i L} - R\right)^2}{e^{2\,\alpha_i L} + R^2 - 2\,e^{\alpha_i L}\cos(2\phi)} \tag{3.12}$$

As this expression is a function of L, α_i, and ϕ, it can be fit to data collected from sweeping a FP cavity to determine both the propagation loss α_i and the modulation as a function of bias $\phi(V)$, as shown in Figure 21. Additionally, the insertion loss (IL) of specific components can be measured by including these in the FP waveguide cavity and extracting the additional loss associated experienced by these cavities compared to the plain FP waveguide cavity. A portion of a die developed for this type of testing is shown in Figure 22.

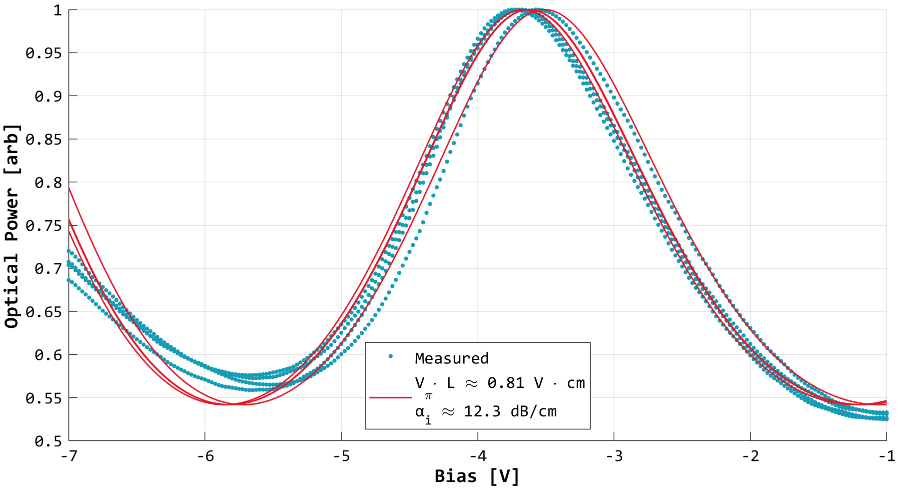

Figure 21: Multiple normalized transmission measurements of a Fabry-Perot waveguide cavity with a phase modulator (dotted blue), and associated simultaneous fit of propagation loss and quadratic phase modulation coefficients (solid red).

Figure 22: Micrograph of several Fabry-Perot waveguide cavity test structures designed to determine the insertion loss of various components.

An expression depending only on the contrast K and facet reflectivity R can also be derived by simplifying the expression for the transmission of a FP cavity to isolate the propagation loss α_i [115]:

$$\mathrm{K} = \frac{(P_{max} - P_{min})}{(P_{max} + P_{min})};\ \alpha_i = \ln\left(\frac{K\,R}{1 - \sqrt{1 - K^2}}\right)/L \tag{3.13}$$

This is useful for robustly obtaining propagation loss measurements from otherwise noisy data or by sweeping the FP cavity fringes with other methods, such as thermal or wavelength tuning.

3.4.2 PHASE MODULATION PERFORMANCE

Phase modulation efficiency and RAM were typically determined by measuring multiple individual phase modulators and assorted test structures. Measurement included edge coupling a lensed fiber into a cleaved-facet PIC input with a 3-axis fiber alignment stage, while the PIC under test rested on a copper block that was thermoelectrically cooled to 20°C. This setup is shown in Figure 23. Packaged 980 nm and 1030 nm fiber-coupled lasers and an O-band tunable laser provided light during all testing, and DC probes provided electrical connectivity.

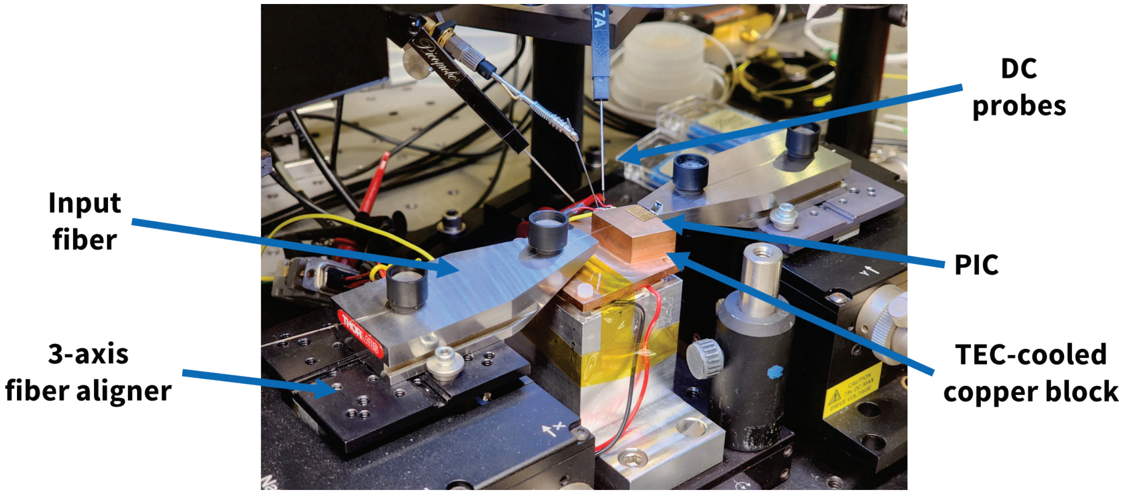

Figure 23: Photograph of equipment used to characterize phase modulators at UCSB.

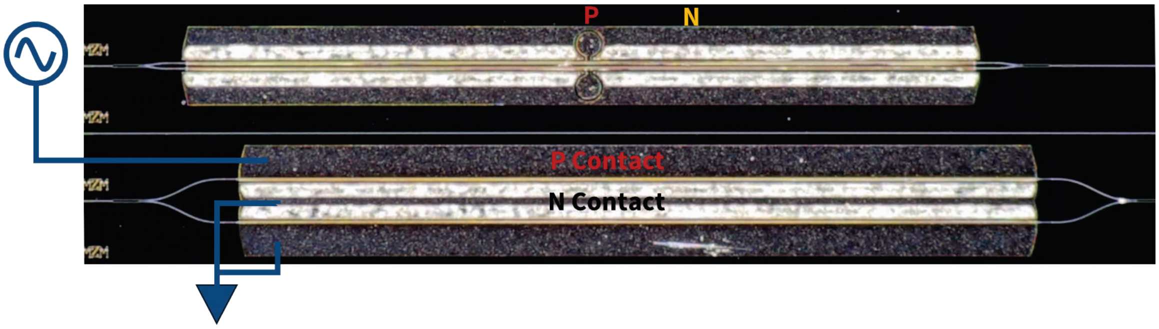

Figure 24: Labeled micrograph of MZM test PIC with two varieties of MZM structures.

Phase modulation performance was primarily characterized with Mach-Zehnder modulator (MZM) test PICs comprising a single input, a 1x2 MMI splitter, phase modulators on each arm, a 2x1 MMI splitter, and a single output, as shown in Figure 24 in two different variations. Single-sided operation was typically utilized for simplicity, with one arm swept and the other arm held at ground or a small DC bias. The electro-optic modulation response was found by rapidly sweeping the bias and recording the simultaneous bias and MZM transmission waveforms on a digital signal oscilloscope, then transforming these signals to transmission as a function of bias by matching timeseries data as shown in Figure 25. By using this simultaneous time-matched approach, data acquisition was completed at >100 kHz, thereby avoiding coupling noise present at acoustic frequencies.

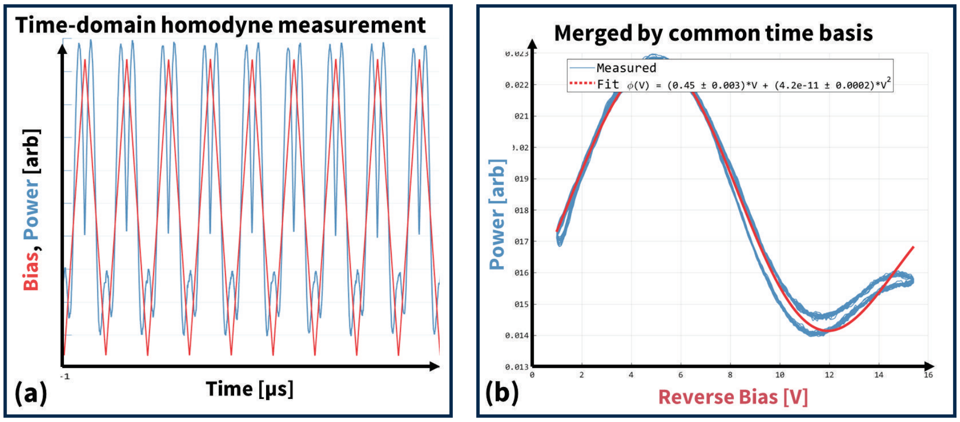

Figure 25: Illustration of MZM measurement method, with the (a) time domain measurement of applied bias (red) and transmitted power (blue) (b) transformed to power as a function of bias by matching timeseries data.

An accurate estimate of the phase modulation $\Delta\phi$ and RAM $\Delta\alpha$ as a function of bias was obtained by simultaneously fitting multiple normalized measurements to the analytical power transmission T of a single-sided unbalanced-loss MZM. The MZM was modeled as an input electric field E_0 that is split into two arms and then coherently recombined, with field E_1 left unmodulated and field E_2 passing through the phase modulator:

$$E_1 = (1-k)\,E_0;\; E_2 = k\,E_0\,e^{i\,\Delta\phi - \Delta\alpha/2} \tag{3.14}$$

$$\begin{aligned} T &= F\,|E_1 + E_2|^2/E_0^2 + (1-F) \\ &= 1 + F\,k\,(-2 + k + k\,e^{-\Delta\alpha}) - 2\,F\,(k-1)\,e^{-\Delta\alpha/2}\cos(\Delta\phi) \end{aligned} \tag{3.15}$$

where k is the splitting ratio and F is the fraction that is coherently recombinable. Fixed propagation losses and common phase evolution were ignored. To reduce the degrees of freedom, the phase modulation and RAM were empirically parameterized by physically motivated but arbitrary fitting functions of the bias potential V, with $V < 0$ in reverse biased operation:

$$\Delta\phi(V) = p_1(V_0 - V) + p_2(V_0 - V)^2 \tag{3.16}$$

$$\Delta\alpha(V) = \mathrm{a}_1\ \exp\big(a_2(V_1 - V)\big)\ (1 - \tanh[V - V_1])/2 \tag{3.17}$$

where $V_0 = 1.62$ V represents the intrinsic electrical field across the p-i-n junction with a value chosen from charge-transport simulations. Parameters $k, F, V_1, p_1, p_2, a_1,$ and a_2 were fit at each measured wavelength. The choice of the $\Delta\phi$ function was motivated by considering the LEO and QEO effects as the primary sources of phase modulation, and the small carrier effects as sufficiently characterized by a quadratic fit. The RAM parameterization $\Delta\alpha$ includes a $\tanh$ function to behave as constant until some turn-on bias V_1, below which it exponentially increases. The fits are valid only within the limits of measurement, V ≥ -12 V and $\Delta\alpha$ ≤ 6 dB. A typical result of one of these fits is displayed in Figure 26 with a single measurement from the multi-measurement fit plotted.

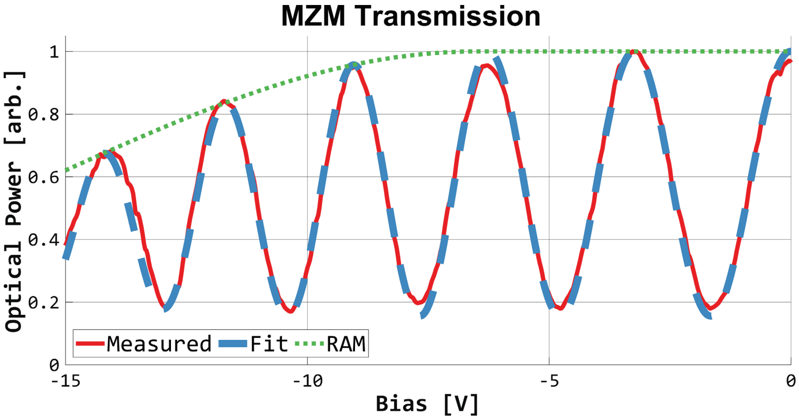

Figure 26: MZM measurement result, with data in red, fitting function in blue, and RAM envelope in green. Data from device in Chapter 4.

To confirm MZM results, a self-heterodyne measurement technique was also used at 1030 nm on individual phase modulators in separate test devices as well as on single channels of OPA PICs. In this technique, the phase modulator is treated as a single arm of a fiber-optic MZM while the other arm is offset by 150 MHz with an acousto-optic modulator (AOM) [116]. Figure 27 shows a diagram of this arrangement. The laser output is split with a fiber-optic splitter, one output is coupled into the PIC and out of one modulator, and the other output is frequency shifted with the fiber-coupled AOM. After recombining in a fiber-optic splitter, the output of the photodiode is equivalent to a phase-shift-keyed (PSK) signal with a carrier frequency equal to the AOM shift and the phase shift equal to the phase applied by the modulator. The PSK waveform can then be decoded with standard IQ demodulation techniques to extract the relative phase shift. By dithering the applied modulation bias with a small amplitude around a DC offset, precise measurements of the phase modulation's first and second derivative and the first derivative of RAM with respect to bias can be obtained at any AC modulation frequency that is less than half the AOM frequency.

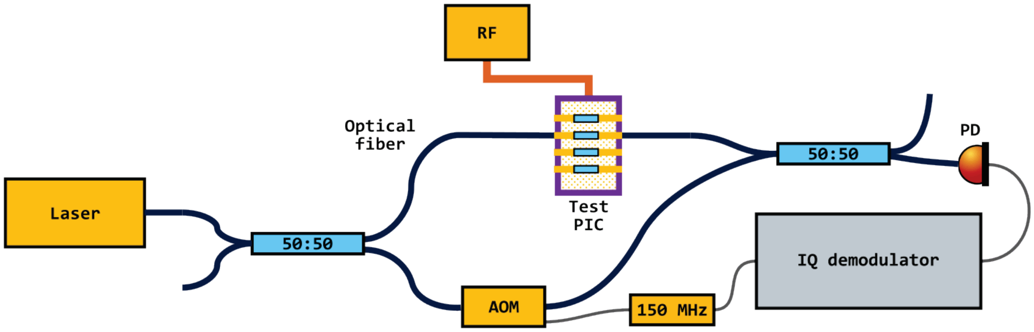

Figure 27: Diagram of self-heterodyne measurement technique.

3.4.3 ELECTRICAL PERFORMANCE

Electrical characterization included using the DC probes shown in Figure 24 to perform current-voltage testing on whole samples before cleaving, singulated PICs, and carrier-mounted PICs, and also included S11 and S12 measurements of printed circuit board (PCB)-mounted PICs, performed with a network analyzer by MKS-ESI.

3.4.4 OPA PERFORMANCE

Key metrics for OPA performance are the full-width half-maximum beamwidth, the grating-lobe-free steering range within which the beam can be unambiguously directed without confusion with a grating lobe, and the sidelobe level (SLL) or background level. From the beamwidth and steering range, the number of uniquely addressable points can be computed, which is a scale-free metric that does not depend on the linear transformations possible with optical lens systems. The number of addressable points is approximately the number of channels for dense linear arrays with ideal beam quality; sparse arrays with nonuniform channel spacings are able to trade worsened SLL for more addressable points.

Analytically, the steering range can be estimated by $\arcsin(\lambda/d)$ and the beamwidth by that of an aperture equivalent to the OPA width, $\sim\lambda/D$, where λ is the free-space wavelength, d is the distance between emitters, and D is the width of the OPA. The envelope of the steered lobe is determined by the single-emitter beam pattern.

The ultimate SLL of a uniform array is 13 dB, limited by the sinc^2 function of the far-field pattern of a uniform aperture [117], and cannot be reduced without nonuniform emitter spacings or output powers.

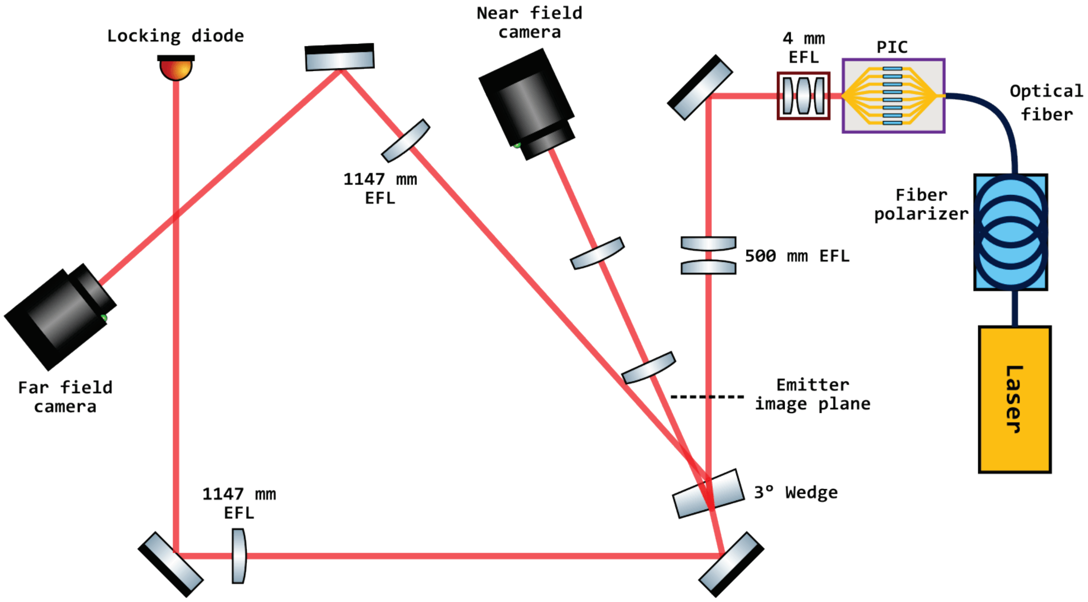

Figure 28: Schematic of OPA optical measurement setup. Not to scale.

The phased-array performance and output pattern of fabricated OPA PICs was evaluated at MKS-ESI facilities using the experimental setup shown in Figure 28. A PIC mounted on a carrier and a PCB is secured to an optical bench, and a lensed fiber on a 3-axis fiber alignment stage couples a 1064 nm laser into the PIC's input facet. The output of the PIC is captured by a 4 mm effective focal length (EFL) objective lens with a 0.65 numerical aperture, and then a 500 mm EFL relay lens re-images the emitter plane to a 500 μm effective emitter spacing.

Past the reimaged emitter plane, the beam is split with a 3° wedge prism; one surface reflection travels through a pair of relay lenses that reproduce the intermediate focal plane on a monitoring camera. The other surface reflection is propagated to the far field and collimated onto an Ophir LT665 beam profiling camera with a 1147 mm EFL lens, while an identical lens images the transmitted far field beam onto a photodiode. The beam profiling camera may be moved to the near field position for near field data collection.

The output phase of each channel is offset by an unknown amount due to differing path lengths and fabrication imperfections, so the LOCSET algorithm [118] is used to cohere the OPA output by applying the requisite phase modulation to each channel to maximize the signal on the far-field photodiode. To steer the output, the photodiode is moved by a micrometer, and the LOCSET algorithm adjusts emitter phases to shift the peak of the beam to the new location. The positional beam profile is converted to an angular profile at the OPA output by backing out the optical transformations: $\theta_{OPA} = \frac{x_{camera}}{1147\ \mathrm{mm}} \cdot \frac{500}{4}$. Data is captured at the 4.54-μm pixel pitch of the beam profilometer, corresponding to 0.028° angular resolution at the OPA output.

3.4.5 ACTIVE DEVICE PERFORMANCE

From the light-current-voltage (LIV) behavior of simple FP lasers of varying lengths, a significant amount of information about the material properties and device performance can be extracted [111]. A single LI measurement can determine the threshold current I_{th} and differential quantum efficiency η_d. Assuming a cleaved-facet FP laser with two identical facets, η_d can be determined by:

$$\eta_d = 2\left(\frac{q}{h\,\nu}\right)\frac{dP_0}{dI} \quad (I > I_{th}) \tag{3.18}$$

where q is the electron charge, h is Plank’s constant, and ν is the optical frequency, and the factor of 2 accounts for the emission from both facets. By measuring FP lasers of several different lengths and computing η_d for each, the internal loss $\langle\alpha_i\rangle$ and injection efficiency η_i can be found by the relation:

$$\frac{1}{\eta_d} = \frac{\langle\alpha_i\rangle\, L}{\eta_i \ln(1/R)} + \frac{1}{\eta_i} \tag{3.19}$$

where R is the mean mirror reflectivity and L is the cavity length. The slope and intercept of multiple η_d measurements at different L thus determine $\langle\alpha_i\rangle$ and η_i . To determine the fundamental $\langle\alpha_i\rangle$ of the material, broad area lasers may be measured with pulsed current injection to avoid the effects of lateral current spreading, carrier leakage, and self-heating that will otherwise influence the effective $\langle\alpha_i\rangle$ of a waveguide laser.

By using an active-passive waveguide FP lasers instead of purely active FP lasers, the propagation loss of the passive section can also be extracted by varying the length of the passive section instead of the active section, although the slightly different indices of refraction in the passive and active regions will complicate the analysis somewhat, as the mirror reflectivities can no longer be assumed to be identical [111].

With the internal loss $\langle\alpha_i\rangle$ and calculated QW confinement factor Γ_{QW}, the threshold modal gain can easily be calculated:

$$\Gamma\, g_{th} = \langle\alpha_i\rangle + \frac{1}{L}\ln\left(\frac{1}{R}\right) \tag{3.20}$$

Finding g_{th} for devices of different lengths, which will occur at different threshold currents I_{th}, the threshold current density, material gain, and transparency current density can be determined [111]:

$$J_{th} = \frac{\eta_i \, I_{th}}{w \, L} \tag{3.21}$$

$$J_{th} = J_{tr} \, e^{g_{th}/g_0} \tag{3.22}$$

where w is the width of the active region. The results of this measurement can be compared to simulated values to determine the MQW simulation accuracy and predict performance of various device configurations.

3.5 Chapter Summary

Chapter 3 has described the methods for device simulation, lithographic mask layout, fabrication process development, and device characterization. Detailed descriptions were provided that included the sources of modeling data, software tools used for simulation and layout, hardware tools used for fabrication, and techniques and equations used for characterization of devices. The methods and resources described here will be used throughout the remainder of this dissertation to produce simulations, develop fabrication processes and fabricate devices, and obtain results to judge the effectiveness of the developed devices.

Chapter 4

OPA PIC with Phase Control

To demonstrate the feasibility of a GaAs OPA PIC platform, a GaAs PIC platform optimized for phase modulators was developed, and several GaAs OPA PICs with phase control were produced. The OPA PIC design consists of an edge-coupled input, a 1x16 splitter, 16 equal channels with 3-mm-long phase modulators, wire bond pads for each channel, and a dense 4-μm-pitch output facet forming a one-dimensional 16-channel optical phased array. The waveguides in all sections were 2 μm wide. The design was limited to 16 channels to simplify integration and testing, but is readily scalable to significantly higher channel count.

4.1 Purpose

16-channel OPA PICs were specifically designed to demonstrate the feasibility of creating integrated OPAs on a GaAs platform. As such, they include all required parts of an OPA and are themselves fully functional OPAs when illuminated with an external laser. No gain material was present, but the components and epitaxy were engineered for compatibility with simple monolithic integration of conventional GaAs-based quantum wells or quantum dots in the 880-1300 nm range [70]– [72]. The design wavelength of all structures was 1030 nm.

4.2 *Preview of Results*

Several iterations of OPA PICs were produced, all based on the same overall design, but with minor layout variations. The first iteration consisted of an OPA PIC with a 7 mm x 2 mm footprint, shown in Figure 29. Initial testing using direct probing of only a few channels confirmed OPA operation by producing movement in the randomized grating lobes of the output the bias of two channels was slowly altered. This initial verification was performed with a 45° turning mirror after the OPA output to allow observation of the output's far field with an inspection camera. Figure 30 shows this setup and images of the grating lobes.

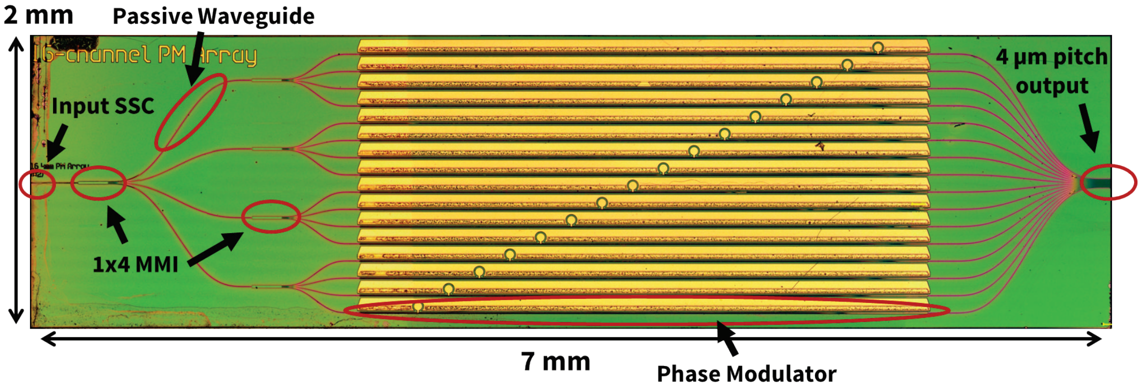

Figure 29: The first iteration of OPA PIC. P-pads were too small for reliable wire bonding.

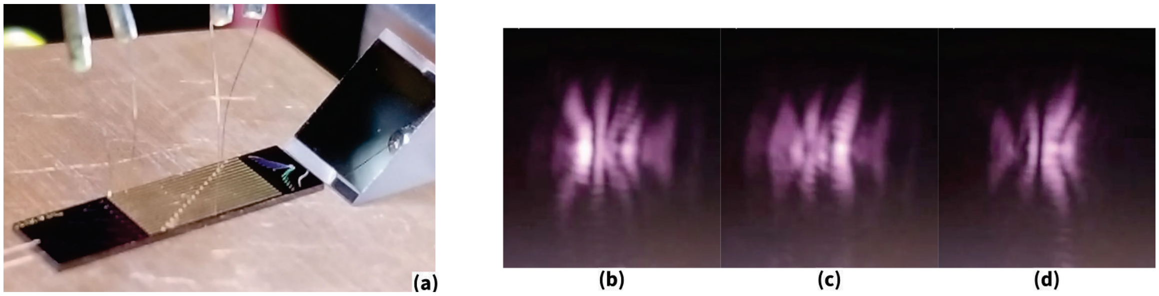

Figure 30: Early OPA output testing with two channels directly probed: (a) photograph of OPA PIC with visible DC probes, input lensed fiber, and 45° turning mirror for output observation, (b,c,d) grating lobes at successively greater biases.

Separate 4-mm-long phase modulators were also fabricated at the same time and demonstrated single-sided $V_\pi \cdot L$ modulation efficiency ranging from 0.5 V · cm to 1.22 V · cm at wavelengths from 980 nm to 1360 nm. While measured single-device performance was excellent and many of the OPA PICs had full optical performance, an oversight during mask layout resulted in P-pads on the OPA PICs that were too small for reliable wire bonding. Because of this, no OPA PICs were successfully mounted and wirebonded while maintaining full electrical connectivity.

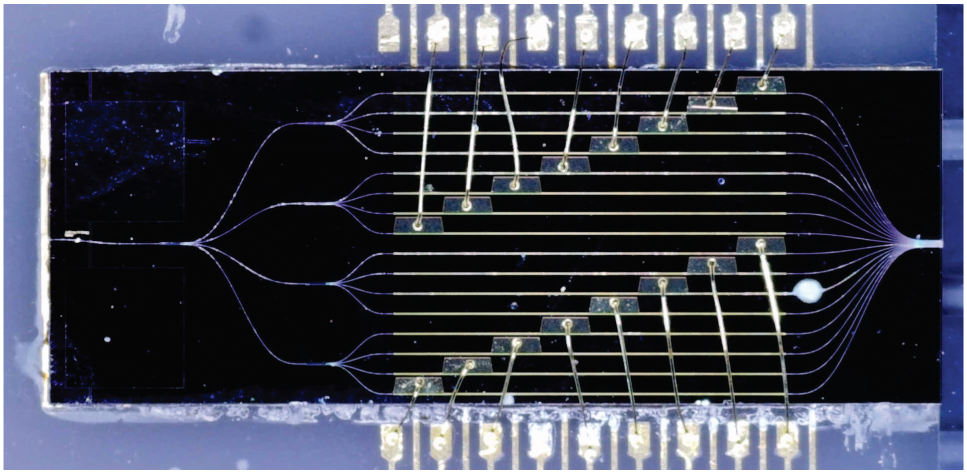

Figure 31: The second iteration of OPA PIC, shown wire bonded to a carrier.

To rectify this oversight, a second iteration was quickly produced with wider channel spacing to allow for larger wire bond pads, as shown in Figure 31, and this was successful. For rapid fabrication, the n-connectivity was provided by a back-side n-pad and the AR coating was performed in house via a simple silicon nitride PECVD deposition. While performant in many cases, some channels experienced spalling of this AR coating, developing cracks and accumulations of contaminants as shown in Figure 32. This reduced the second iteration's optical yield, such that no devices had both full electrical and optical functionality in all 16 channels.

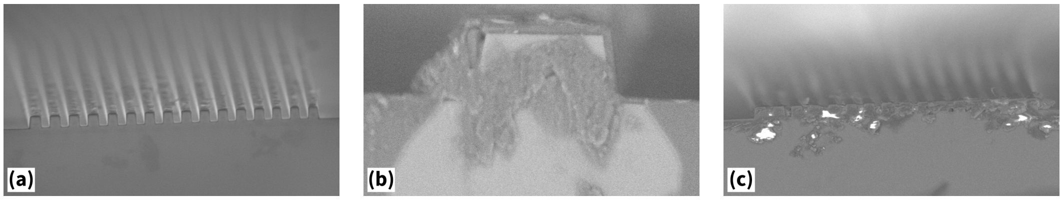

Figure 32: AR-coated facets from the second iteration OPA PIC: (a) good output facets, (b) spalled AR coating on an input facet, (c) contaminated output facets.

A third iteration was developed to rectify the previous yielding issues, resulting in an OPA PIC with a 5.2 mm x 1.2 mm footprint, shown in Figure 33. Several design and process updates were incorporated here, including a 30 μm modulator pitch with wire bond pads broken out to the side. This design successfully resolved the electrical and optical problems experienced in the first two iterations, and all further mentions of the OPA PIC with phase control design refer to this third iteration.

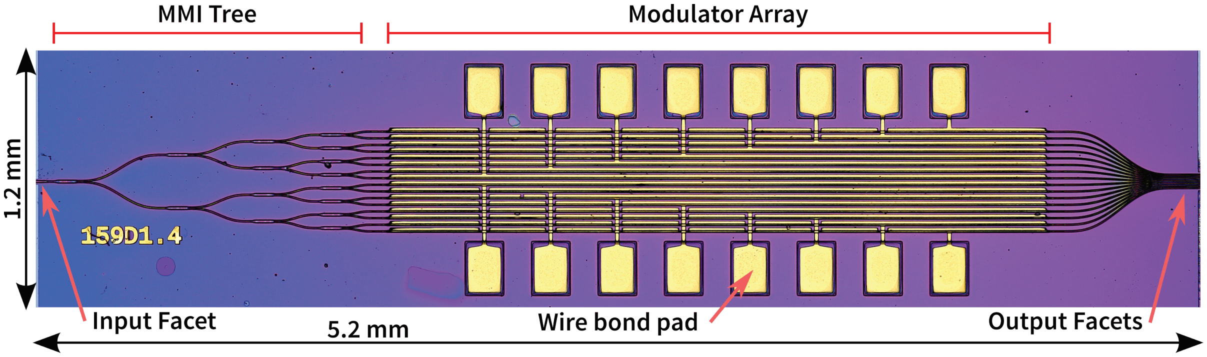

Figure 33: Optical micrograph of fabricated third iteration OPA PIC with phase control.

The 16-channel 1-dimensional OPA output of this device demonstrated a 0.92° beamwidth with 15.3° grating-lobe-free steering range, 12 dB sidelobe level, and greater than 770 MHz single-element electro-optical bandwidth operating at 1064 nm. The integrated phase modulators demonstrated single-sided $V_\pi \cdot L$ efficiency of 0.7 V·cm, RAM below 0.5 dB for greater than 4π phase modulation [119], and DC power consumption of less than 5 μW at 4π modulation depth. A detailed publication reporting the design, fabrication, and performance of this device has been published in *Optics Express* [120].

4.3 Epitaxy Design

The epitaxy of the OPA PICs was optimized for phase modulators ideally suited for OPA applications. This requires low propagation loss to enable channel count and output power scaling, low RAM for continuous beamforming over the entire steering range, and high electro-optical bandwidth for rapid beam scanning. To meet these requirements, the modulators were designed with a GaAs-based P-p-i-n-N double heterostructure for reverse biased operation, detailed in Table 1. The refractive indices and assumed material losses used for simulation are also listed, with the sources previously detailed in section 3.1.1.

Table 1: OPA PIC epitaxial layer structure.

Material	Thickness [nm]	Doping [cm^{-3}]	Refractive Index at 1030 nm	Material Loss at 1030 nm [dB/cm]
GaAs	300	(p) 1e19	3.4653	140
$Al_{0.2}Ga_{0.8}As$	1000	(p) 1e18	3.4046	15
$Al_{0.4}Ga_{0.6}As$	200	(p) 4e17	3.3551	19
$Al_{0.4}Ga_{0.6}As$	200	(p) 2e17	3.3551	11
GaAs	100	(p) 2e17	3.4653	7.2
GaAs	500	UID	3.4653	0.04
GaAs	100	(n) 2e17	3.4653	8.0
$Al_{0.3}Ga_{0.7}As$	200	(n) 2e17	3.3811	13
$Al_{0.2}Ga_{0.8}As$	400	(n) 4e17	3.4046	21
$Al_{0.2}Ga_{0.8}As$	1000	(n) 2e18	3.4046	100
GaAs	300	(n) 3e18	3.4653	120
GaAs	Substrate	(n) 1e18	3.4653	40

With a reverse bias applied, this structure yields a high overlap between a nearly linear electric field along the $[001]$ direction and the optical mode, as shown in Figure 34(a). This high overlap efficiently utilizes the strong linear and quadratic electro-optic effects of GaAs for TE modes propagating in the $[1\bar{1}0]$ direction as detailed in section 2.4.1. Additional modulation is available from free carrier effects, but to reduce RAM, these effects are avoided by reverse-biased operation. Figure 34(b) reports the expected phase modulation contributions at 1030 nm for a modulator based on this design. Low optical absorption and RAM are achieved by realizing an 85% overlap between the optical field and the GaAs guiding region, and only a 19% overlap with free carriers at a bias of -10 V.

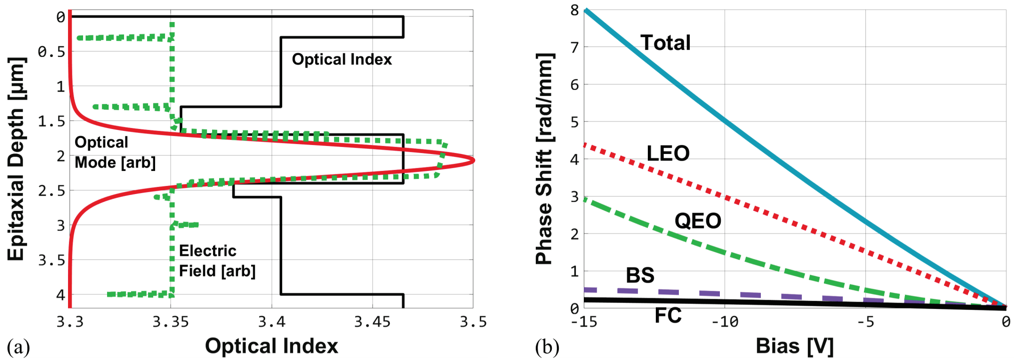

Figure 34: 1D simulations showing (a) optical index (black), optical mode (red), and electric field (green, dotted), (b) expected phase modulation at 1030 nm (cyan) for this design, including contributions from linear electro-optic (LEO, red, dotted), quadratic electro-optic (QEO, green, dot-dashed), bandgap shift (BS, purple, dashed), and free carrier plasma (FC, black) effects.

4.4 Component Design

An OPA has several basic requirements: a laser source, distribution to multiple channels, phase control, and output coupling. For this OPA PIC demonstration, the laser source is off chip, so an input coupler is required instead. These components are provided on this PIC by an efficient input coupler, a passive waveguide structure and 1x2 MMI splitters to route and split light where needed, a phase modulator, and an output facet.

Preliminary design exploration as well as experience with the previous fabrications of similar PICs determined that all components were best constructed of deep ridge waveguides, with schematic cross-sections shown in Figure 35. Deep ridge construction was primarily chosen to allow bending, as required by the fan-out transition from a single input to multiple parallel channels. Shallow rib waveguides, in contrast, have very weak confinement and thus very large bend radii. Reverse-biased phase modulators are not at risk of sidewall recombination, so the deep ridge construction has no strong drawbacks. The only concern with deep ridge construction is sidewall smoothness, which must be optimized to avoid excessive propagation loss from sidewall scattering.

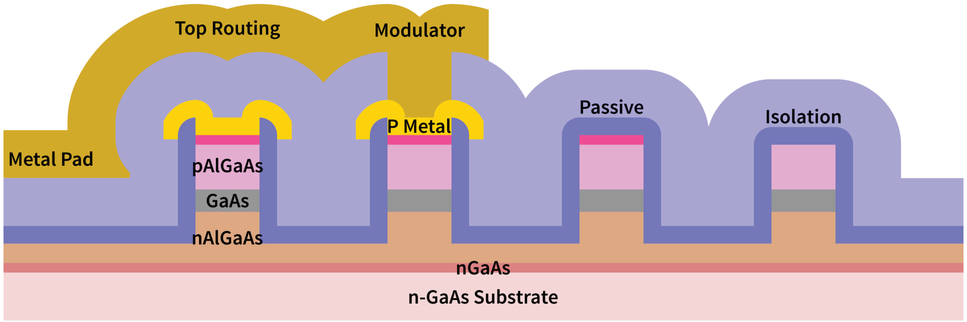

Figure 35: Cross-section schematic of epitaxy and assorted waveguide structures.

4.4.1 PASSIVE WAVEGUIDES

The passive waveguides are formed by a single deep ridge etch approximately 4 μm deep. A 2.5-μm-thick material composed of alternating layers of silicon dioxide (SiO_2) and silicon nitride (SiN) is present over the entire PIC to provide electrical passivation and isolation, and protection from environmental effects. This material is visible as dark and light blue shading in Figure 35.

A 2 μm waveguide width is chosen for fabrication simplicity and lithographic resolution constraints; the i-line steppers used in fabrication can achieve approximately 0.8 μm resolution at best, and 1.0 μm resolution in typical usage. This width does not provide inherently single mode waveguides, but single-mode operation is weakly achieved by MMI splitter loss and bend loss that is stronger for higher order modes than the fundamental mode. Strict single-mode operation requires waveguides roughly 0.5 μm wide, which requires a difficult-to-fabricate aspect ratio given the etch depth.

These 2-μm-wide passive waveguides are used to route the light between other components. Short segments of the waveguides on either end of the phase modulators are turned into electrical isolation regions by removing the highly conductive top p-GaAs layer, preventing the bias applied to the modulator p-contacts from propagating into the surrounding passive waveguide sections and causing undesired phase modulation. The right half of Figure 35 illustrates these passive components, and Figure 36(a) shows the simulated fundamental TE mode. The fundamental TE optical mode has a $1/e^2$ Gaussian mode field diameter (MFD) of approximately 0.95 μm in the vertical direction (normal to the epitaxial surface), and 1.5 μm in the lateral direction (parallel to the surface) with an effective mode area of 1.18 μm^2. Expected waveguide loss is 4.1 dB/cm, primarily from optical overlap with doped regions.

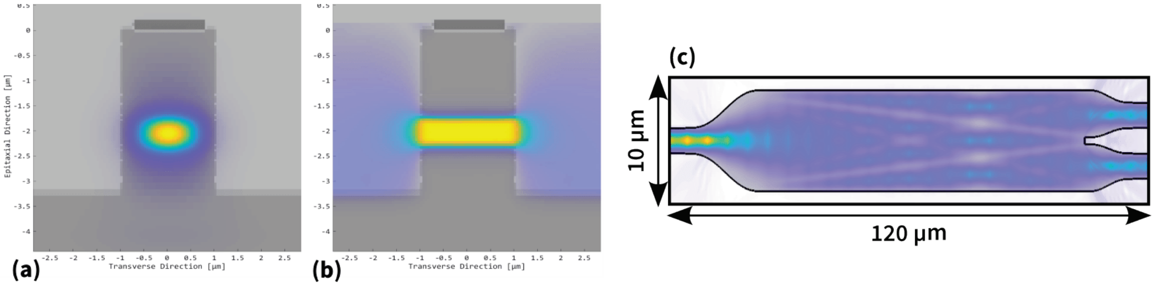

Figure 36: (a) Simulated fundamental TE optical mode of modulator and passive waveguides (color) and waveguide structure (shaded grey). (b) Simulated electrical field of phase modulator at -10 V bias. (c) Simulated optical fields of 1x2 MMI splitter.

Cleaved waveguide facets with antireflection (AR) coating form the single input and 16 outputs. Input light is edge-coupled from a lensed fiber with a 2 μm spot size. As this couples poorly to a 2-μm-wide waveguide, with an expected 5 dB coupling loss, a spot size converter is created by using a 4.8-μm-wide waveguide at the input facet and tapering it to the nominal 2 μm width over a 60 μm length, resulting in a spot size converter with an expected 3 dB coupling loss.

The MMI splitters forming the 1x16 splitter share the same passive waveguide structure, with geometry initially determined by standard high contrast MMI ratios [121]. 3D FDTD simulation of the epitaxial structure was used to slightly modify the geometry for optimal performance, as shown in Figure 36(c).

Center-fed 1x2 MMI splitters were selected due to their robust tolerance and wide bandwidth, and have simulated excess optical loss under 3 dB from 920 nm to 1280 nm. 1x4 MMI splitters were also successfully implemented with a 280 μm shorter tree, but are not as broadband (1000-1180 nm) and have tighter fabrication tolerances.

4.4.2 PHASE MODULATORS

The phase modulators are implemented by the same structure as the passive waveguides, with the addition of P-contacts on top and an N-contact on the back side of the thinned, conductive GaAs substrate. Vias through the isolation material are formed on top of the phase modulator ridges to access the P-contacts, and routing to wire bond pads is achieved by metal deposited on top of the isolation material. The P-contacts are therefore present along the entire length of the modulators, and are connected to the top routing metal by the top vias. The routing metal then connects to large wire bond pads, crossing above other modulators where needed, as shown in the left half of Figure 35. The cross-modulator routing can also be seen in Figure 33.

A p-i-n diode is thus formed vertically through the waveguide, with the P-contact on top connected through the top p-AlGaAs cladding to the p-GaAs, the N-contact connected through the substrate and lower n-AlGaAs cladding to the n-GaAs, and the unintentionally doped (UID) middle GaAs layer forming the intrinsic region in the optical guiding layer. When reverse biased, this gives rise to the nearly linear electric field overlapping the optical mode, visible in Figure 34(a) and Figure 36(b).

Using the simulated optical and electrical fields shown in Figure 36 and the methods to determine the phase modulation described in section 3.1.3, at -10 V bias the expected phase modulation of the TE0 mode is 5 rad/mm with 0.09 dB/mm RAM.

4.5 Mask Layout

These components were assembled together into a 5.3 mm x 6.7 mm die, shown in Figure 37. Each die contains 4 separate 16-channel OPA PIC devices, two each with 1x2 MMI splitter trees and 1x4 MMI splitter trees. Each 16-channel device consists of a spot-size converter for the edge-coupled input, a 1x16 splitter, 16 equal channels on a 30 μm pitch with 3-mm-long phase modulators and wire bond pads broken out to the side, and a dense 4-μm-pitch output facet forming a one-dimensional 16-channel optical phased array.

Fabry-Perot test structures are included on the top (image left) of the die, and MZM test structures are included on the bottom (image right) of the die. Between 6 and 15 dies were present in each processed sample.

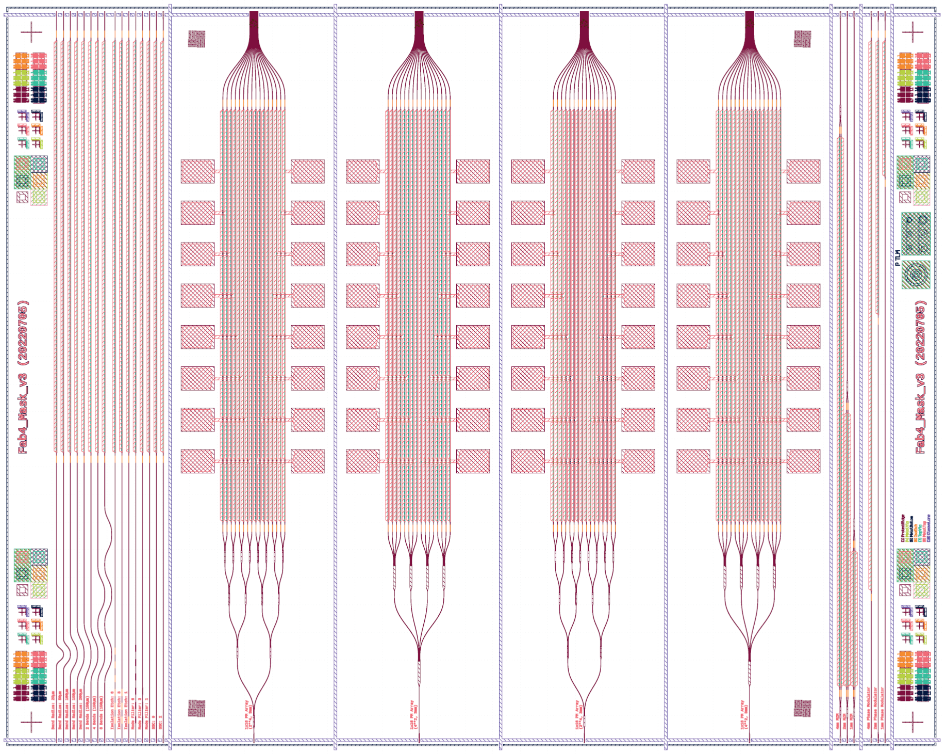

Figure 37: Mask geometry for OPA PIC die.

4.5.1 TRACE WIDTH RC OPTIMIZATION

As a minor design choice, the width of the metal pad of the phase modulators was selected to minimize the resistance-capacitance (RC) time constant. Since the phase modulators are treated as lumped-element devices, the RC time constant is the limiting factor for electro-optic bandwidth. For these devices, the resistance of the metal trace, assumed to be gold with $\rho_{Au} \approx 2.4 \cdot 10^{-8}$ Ω·cm, is significantly lower than that of the top layer of p+GaAs, with $\rho \approx 10^{-2}$ Ω·cm, so the p+GaAs resistance can be neglected.

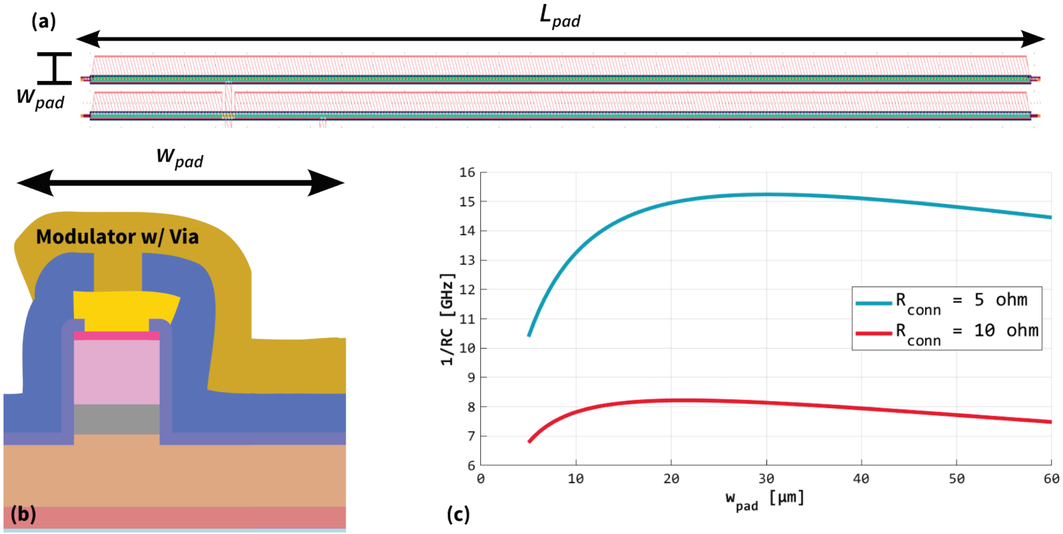

Figure 38: (a) Mask layout schematic of two phase modulators with the relevant parameters indicated, not to scale. L_{pad} is chosen by other considerations. (b) Cross-section schematic with the relevant parameter w_{pad} indicated. (c) Plot of the dependence of the RC time constant on parameter w_{pad} for two different connection resistancesR_{conn}, showing ideal w_{pad} between 15 μm and 30 μm.

Thus, the effective resistance and capacitance of the reverse-biased diode is:

$$R \cdot C = \left(R_{conn} + R_{pad}\right)\left(C_{junction} + C_{pad}\right) \tag{4.1}$$

Where R_{conn} is the connection series resistance between the trace and the point of connection to a transmission line, $C_{junction}$ is the junction capacitance of the modulators themselves, determined from charge-transport simulation to be approximately 5 pF/mm, and C_{pad} is the capacitance of the metal pad. Assuming the majority of the pad is on the field and not on the waveguide, it is effectively a capacitor formed by the pad, the isolation dielectric, and the n+GaAs layer of epitaxy below the guiding layer. This is illustrated in Figure 38(a,b). The relevant quantities are then:

$$R_{pa} = \frac{\rho_{Au}\, L_{pad}}{t_{pad}\, w_{pad}}; \;\; C_{pad} = \kappa_{SiN/SiO} \frac{\epsilon_0\, L_{pad}}{t_{SiN/SiO}} \tag{4.2}$$

With L_{pad} set by other design considerations and R_{conn} as an estimated but unknown quantity, w_{pad} is then the only free parameter. Maximizing $(R{\cdot}C)^{-1}$ finds an optimal $w_{pad,optimal} \approx \frac{68}{\sqrt{R_{conn}}}$ between 15 μm and 30 μm as shown in Figure 38(c), for reasonable values of R_{conn}. As $(R{\cdot}C)^{-1}$ only slowly decreases at over-large w_{pad}, a conservative value of 20 μm was selected for the pad width.

4.6 Fabrication Process

The fabrication process was designed for low fabrication complexity compared to typical III-V processes, and consisted of seven mask sets, two GaAs etches, and two metal lift-off steps. Figure 39 shows schematic diagrams of the primary fabrication process steps.

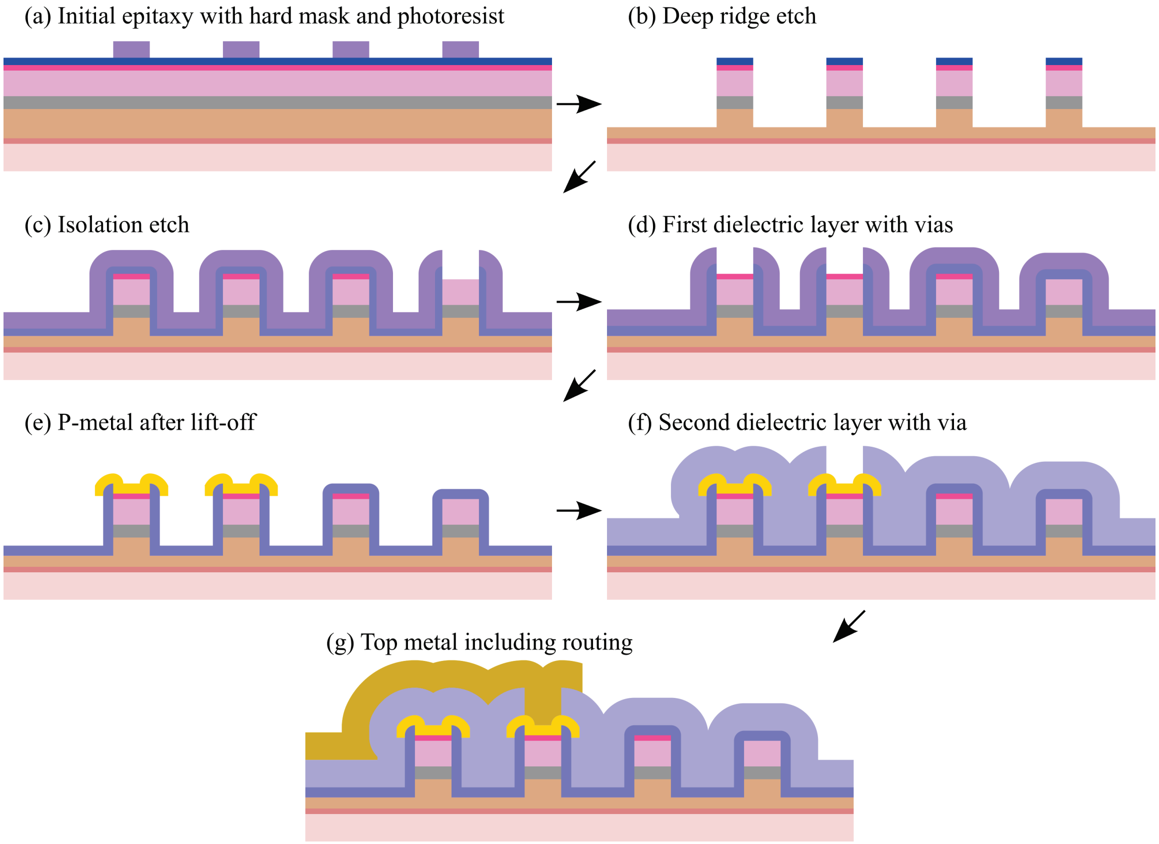

Figure 39: Schematic diagrams of primary fabrication process steps. (a) Initial epitaxy with hard mask (blue) and patterned photoresist (purple). (b) Deep ridge etch. (c) Isolation etch. (d) First dielectric layer (light blue) with p-via openings. (e) P-metal (yellow) after lift-off. (f) Second dielectric layer (lighter blue) with via opening. (g) Top metal (dark yellow) including cross-modulator routing.

The process begins with the deposition of a 400 nm SiO_2 hard mask on clean epitaxy via PECVD. Photoresist is patterned on top of this by an i-line stepper, defining the waveguide pattern. Unprotected regions of the hard mask are removed by ICP-RIE with CHF_3/CF_4

chemistry, and the waveguides are defined by a 4-μm-deep Cl_2/N_2 ICP-RIE etch. Figure 40 shows the typical waveguide sidewalls immediately after etching, which display only slight roughness with <100 nm scale. This roughness stems from lithographic roughness, and could be improved with additional lithography process development.

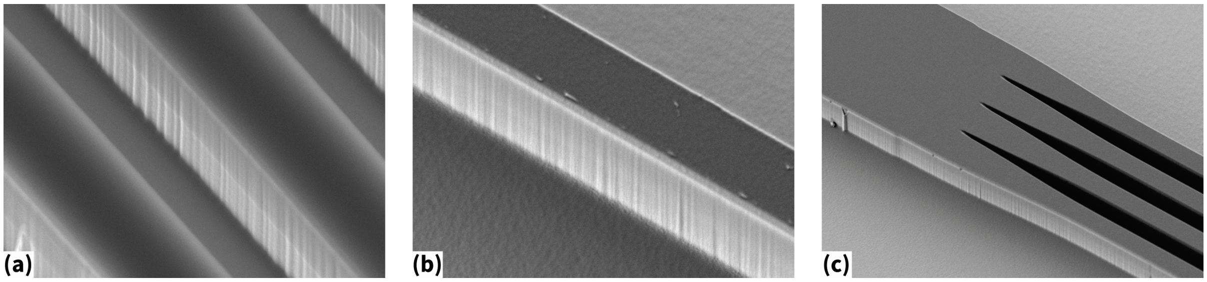

Figure 40: SEM images of selected waveguides immediately after deep ridge etch.

After removing the waveguide hard mask with buffered HF (BHF), another hard mask is deposited and patterned, and a $BCl_3/SF_6/N_2$ selective ICP-RIE etch is used to remove the top p+GaAs layer in the electrical isolation regions without etching the top AlGaAs cladding, as shown in Figure 41(a). The isolation-etch hard mask is removed by BHF and the devices are passivated with 5 nm Al_2O_3 and 10 nm SiO_2 by atomic layer deposition, on top of which the first dielectric isolation layer of 550 nm total thickness is deposited in alternating SiO_2 and SiN layers via PECVD.

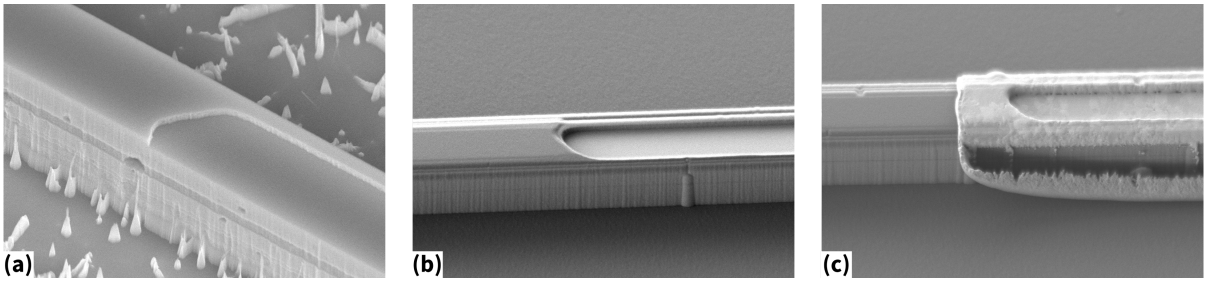

Figure 41: SEM images of (a) isolation etch on a waveguide, (b) top metal via over phase modulator, and (c) P-metal applied to opened via.

The first dielectric isolation layer is selectively opened above the modulator waveguides by a photoresist mask and CHF_3/CF_4 ICP-RIE etch, shown in Figure 41(b), and a lift-off mask is defined with negative photoresist. After depositing 20/40/500 nm of Ti/Pt/Au with electron beam deposition, the metal is lifted off to define the lower metal layer, forming the modulators' top P-metal contacts as shown in Figure 41(c). Another PECVD step forms the second dielectric isolation layer with 2 μm total thickness of alternating SiO_2 and SiN layers, and vias are opened to the first metal layer by another ICP-RIE etch on a photoresist mask. The second lift-off step with 20/3000 nm of Ti/Au then forms the top metal layer for routing and wire bond pads. Shown in Figure 42(a) is a cross-modulator trace formed by this second lift-off step. A final lithography and ICP-RIE etch defines cleave lanes by removing all dielectric layers from selected areas, shown in Figure 42(b). To complete fabrication, the substrate is thinned to approximately 200 μm, 10/50/100/20/500 nm of Ni/Ge/Au/Ni/Au N-metal is deposited on the back side, and devices are rapidly thermally annealed in forming gas at 400°C then 480°C for 10 seconds each.

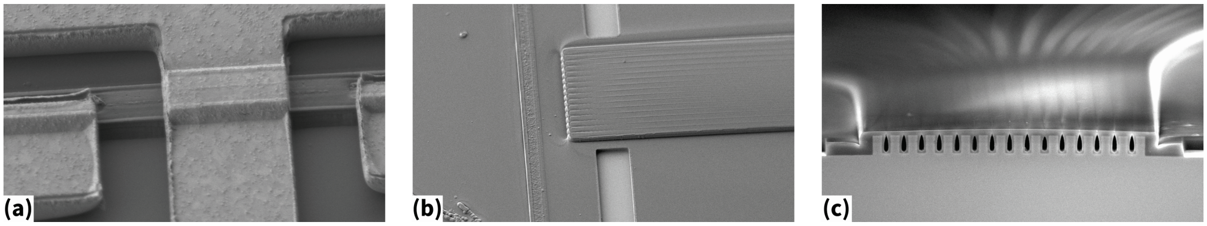

Figure 42: SEM images of (a) top metal cross-modulator routing, (b) opened cleave lanes near the output facet, and (c) output facet after AR coating.

After electrical testing to determine initial yield, selected dies are separated, facets are formed by mechanical cleaving, AR coatings are applied to the facets, and individual PICs are singulated. Figure 42(c) shows a typical cleaved and AR coated output facet, and Figure 43(a) illustrates the scale of a singulated 16-channel PIC. Individual PICs are then mounted to aluminum nitride (AlN) carriers with electrical traces and wire bonded. The PIC-on-carriers are then soldered and wire bonded to PCBs as shown in Figure 43(b).

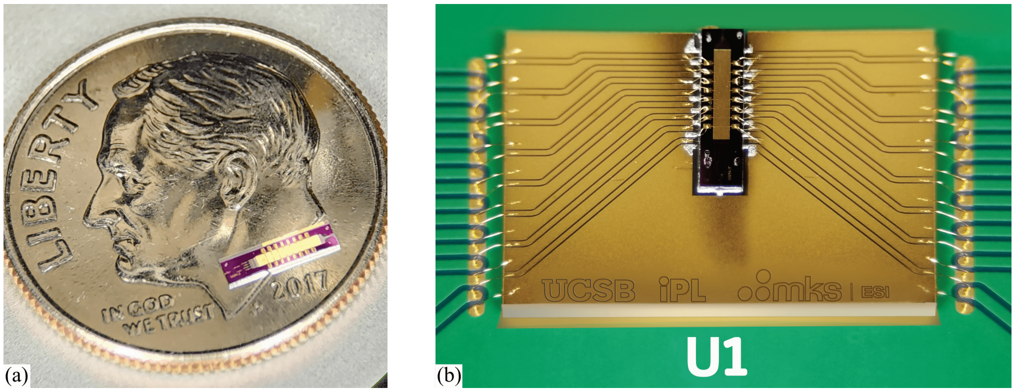

Figure 43: (a) Photograph of 16-channel PIC on US dime. (b) Photograph of PIC-on-carrier on PCB, retouched for clarity.

4.7 Fabrication Review

Several samples were produced by this fabrication process, containing a number of OPA PICs. These were optically inspected, electrically tested, and optically tested to determine full electrical functionality, optical insertion loss, and ultimately device yield. Three fully functional PICs were packaged and shipped to the OPA testing facility.

4.7.1 VERIFICATION

Optical inspection was performed with a digital optical microscope with scanning capability, fully imaging each sample at 200X magnification. The resulting images were then inspected to find broken waveguides, as shown in Figure 44.

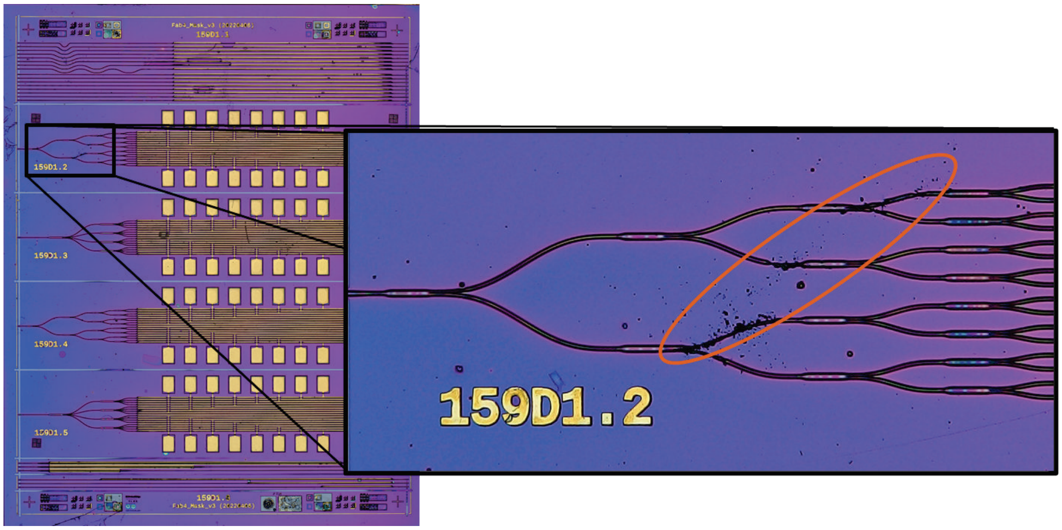

Figure 44: Detection of broken waveguides in full-sample micrograph.

Electrical verification and optical insertion loss measurements were performed in the optical testing laboratory both before and after carrier and PCB assembly. Electrical testing first verified expected current-voltage (IV) curve characteristics for each electrical channel. Optical transmission was initially tested with an inspection camera viewing the output of each device as the input was coupled to a 1030 nm laser with a lensed fiber. Devices which showed multiple output channels were optically tested in detail by sequentially measuring the total optical insertion loss of each channel with a 2-μm-MDF lensed fiber on the input and output, thus verifying full optical functionality. The total optical insertion loss from the input to a single output channel varied from 23 dB to 26 dB.

The overall yield of the this OPA PIC design was 16% in terms of fully functional devices. Neglecting one-off mistakes and easily improvable processes, the expected future yield is 39% or better.

4.7.2 NOTABLE PROCESS STEPS

Several fabrication steps produced suboptimal results that reduced functional device yield. The highest impact of these that were not isolated events, e.g. accidental sample breakage, were the dependence of the Oxford ICP etch on exposed area that was discovered during final sample processing, and insufficiently thick photoresist when opening top vias.

The Oxford ICP was used in this fabrication for deep ridge Cl_2/N_2 etching, and a recipe for a high quality etch was developed using small ~1 mm^2 samples with results exemplified by Figure 45(a). However, during the etching of the larger final samples, a significant dependence on exposed GaAs area was discovered, resulting in one sample with a “grassy” surface shown in Figure 45(b,c). The process was adequately adjusted to compensate during the etching of the two other final samples, but the devices on the poorly etched sample evinced 2-6 dB higher total IL.

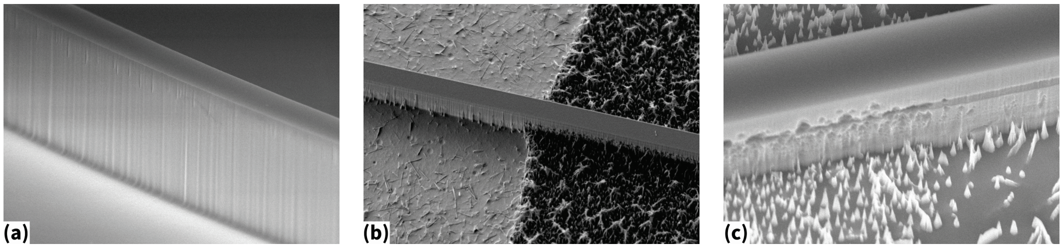

Figure 45: SEM images of (a) deep ridge etch as developed on small test samples, (b,c) “grassy” result of deep ridge on larger real sample.

Another step that was inadequately tested prior to fabrication was the top via lithography. After opening the initial top vias with, it was discovered that the photoresist was insufficiently thick on most waveguide segments, leading to full removal of the hard mask and slight etching of the top GaAs layers, as shown in Figure 46(a). Larger structures such as the MMI splitters were able to retain sufficient photoresist to avoid etching, but photoresist thickness variations on the edges effects caused uneven erosion in these cases, seen in Figure 46(b). The inadvertent removal necessitated stripping and reapplying the dielectric before proceeding. The same problem recurred in the final top via etch through the much thicker isolation layer, shown in Figure 46(c).

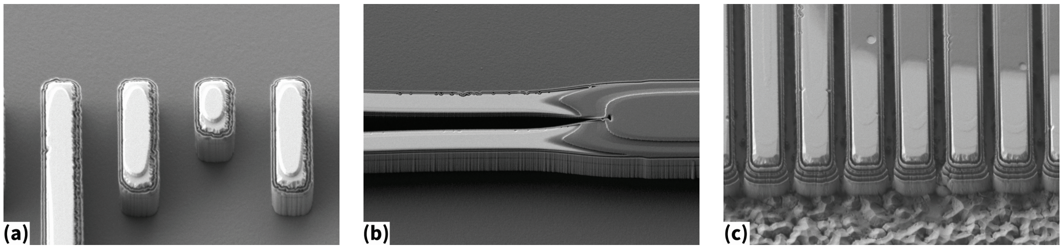

Figure 46: SEM images of (a) unintended removal of top hard mask and partial etching of top GaAs layers due to insufficiently thick PR during top via opening, (b) partially retained hard mask during the same process, (c) unintended removal of top hard mask during final via etch.

Both of these steps were subsequently improved for the next fabrication detailed in Chapter 5 below, but bear careful examination for future processing. The variation in Cl_2/N_2 etch behavior was solved by moving to the Panasonic ICP #1 tool, a larger ICP-RIE tool with less area dependence but more temporal variation. The unintentional dielectric etching during top via opening was solved by using thicker photoresist.

4.8 Characterization

4.8.1 PROPAGATION LOSS

The total insertion loss (IL) of the full 16-channel OPA PICs was measured to determine approximate propagation loss and component excess loss (EL). The expected IL from a lensed fiber coupled to the input to a lensed fiber coupled to a single output is 22 dB. This is composed of 3 dB from lensed fiber coupling at each facet, 1 dB from the MMI splitter tree, 12 dB from the 1/16 splitting, and 3 dB from propagation. The measured IL of the first generation OPA PIC was 20-24 dB depending on the specific device. The measured IL of the third generation OPA PIC was 23-26 dB depending on the specific device. These insertion losses compare favorably to the expected values, indicating propagation loss close to expected, and low excess loss from the assorted PIC components.

The propagation loss of the epitaxy was also characterized directly using the FP waveguide-based measurement technique described in section 3.4.1. Measured on an initial test fabrication utilizing straight cleaved-facet shallow rib waveguides, the results are reported in Figure 47.

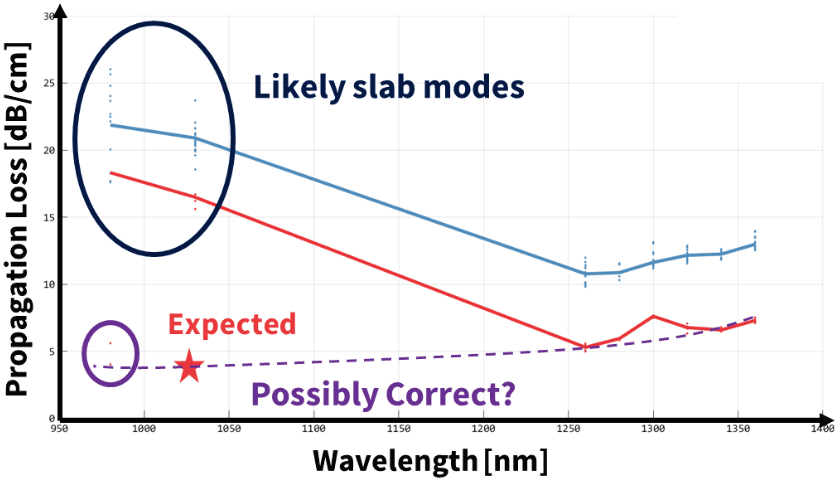

Figure 47: Fabry-Perot waveguide-based propagation loss measurements of an initial test fabrication at various wavelengths, with different polarizations in red and blue. The dotted purple line shows that an extrapolation of the measured loss at long wavelengths matches the expected performance and several measurements at short wavelengths.

Expected propagation loss at 1030 nm was 4.1 dB/cm. While most of the measurements were significantly above this, the long-wavelength measurements and several 980 nm measurements were in the correct range. The most likely explanation for the higher measurements at low wavelengths is that the slab modes were being measured, i.e., propagation through the lower cladding or substrate, which have high expected loss due to high doping. Extrapolating the long-wavelength data to the lower 980 nm measurements indicates a likely value of ~4.5 dB/cm, in line with the expected propagation loss. The low OPA PIC IL values clearly indicate that the higher propagation loss numbers are not measuring the waveguide propagation loss.

4.8.2 PHASE MODULATOR OPTICAL PERFORMANCE

The phase modulator optical performance was primarily characterized by 4-mm-long MZM devices produced during the first generation fabrication, shown in Figure 48, but was also verified for the 3-mm-long OPA PIC modulators by the self-heterodyne measurement technique described in section 3.4.2. This technique was applied directly to the fully mounted 1x16 OPA PICs, and the results agreed with the MZM measurements.

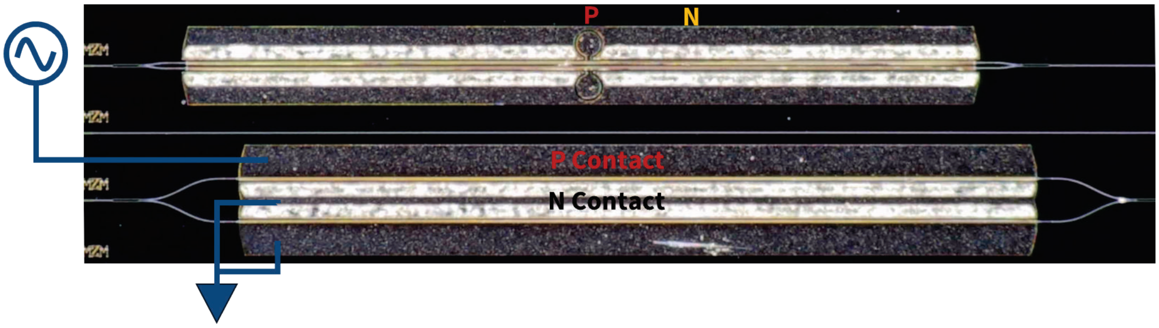

Figure 48: Annotated micrograph of MZM test structures produced during the first generation fabrication and used for phase modulator characterization.

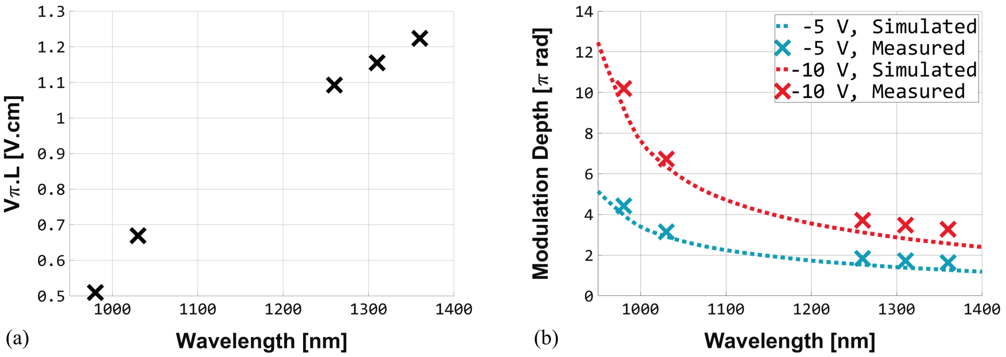

Figure 49: (a) 4-mm-long phase modulator efficiency at various wavelengths. (b) Simulated (lines) and measured (crosses) phase modulation of 4-mm-long devices at various wavelengths and biases.

Tested at wavelengths from 980 nm to 1360 nm, the 4-mm-long devices in the MZM test PICs demonstrated single-sided $V_\pi \cdot L$ modulation efficiency ranging from 0.5 V·cm to 1.22 V·cm for the TE optical mode, as shown in Figure 49(a). RAM is negligible until the onset of Franz-Keldysh electroabsorption, reaching 0.5 dB at a bias of -4.2 V at 980 nm (>3.5π rad), -7.6 V at 1030 nm (~5π rad), and equipment-limited -12 V at 1260 nm (>4.5π rad) and longer, as shown in length-normalized values in Figure 50.

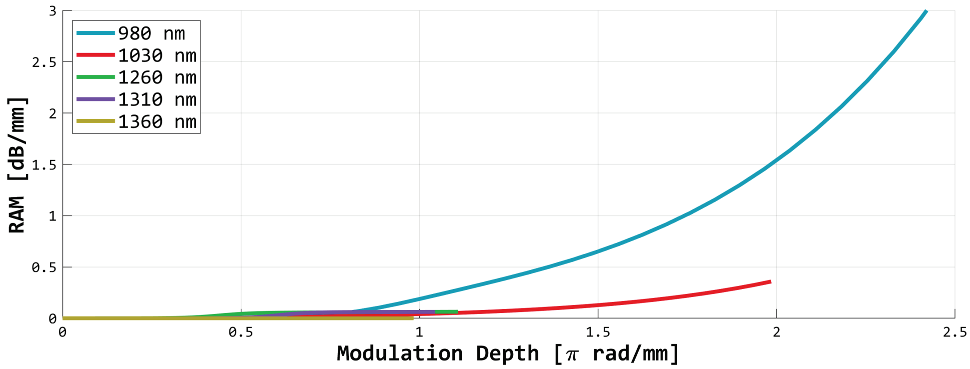

Figure 50: RAM as a function of modulation depth calculated from tested MZM structure data; both are functions of applied bias, which is equipment limited to -12 V.

By simulating the electric and optical fields of these modulators and applying well-known literature values for the various GaAs phase modulation effects as described in section 3.1, the expected performance of these modulators is calculated. Without adjusting any model values, the expected performance shown in Figure 49(b) is in very good agreement with measurements across the full bias and wavelength range. The slight underestimate may be due to free carrier effects, especially at longer wavelengths where the electro-optic effects are weak, as literature coefficients for free carrier effects are inconsistent.

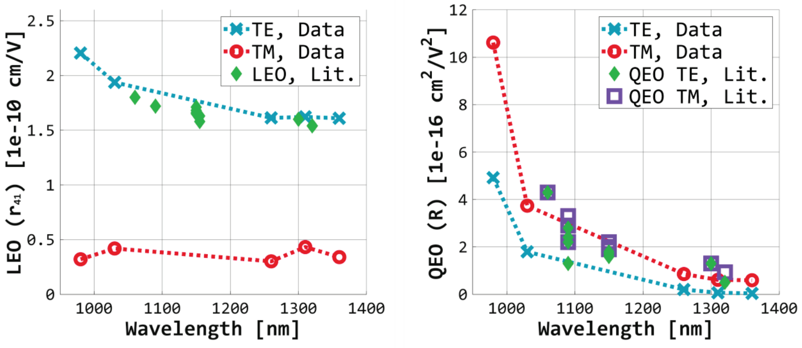

(a) (b)

Figure 51: (a) Measured linear modulation efficiency and expected electro-optic coefficients from literature. (b) Measured quadratic modulation efficiency and expected electro-optic coefficients from literature.

Directly comparing the quadratic fit of the phase modulation efficiency to the linear and quadratic electro-optic coefficients from literature [75], [76], [84], the measured result agrees well as shown in Figure 51. This comparison relies on simulated values for the electrical field in the optical guiding layer, which roughly agrees with a simple assumption of applying the bias voltage directly across the p-i-n GaAs layers. The nonzero linear terms for TM polarization are attributed to the built-in junction field, carrier effects that were not broken out for this comparison, and imperfect polarization that was not strictly controlled.

4.8.3 PHASE MODULATOR ELECTRICAL PERFORMANCE

Detailed input-reflection (S11) electrical measurements were performed on several PCB-mounted PICs at the OPA testing facility. The expected electrical transmission (S12) and relative contributions of the packaging and PIC were determined by separately characterizing the PCB and applying a lumped-element model to fit the resistance, capacitance, and inductance of the PCB, carrier, PIC, and wire bonds to the S11 measurements. From this, the PIC modulators were determined to have 5 ± 3 Ω series resistance and 3.6 ± 0.2 pF capacitance. The expected 3 dB electrical bandwidth of the phase modulators on mounted PICs is 700 MHz, and minor changes to the PCB were identified that should increase this to 1.4 GHz.

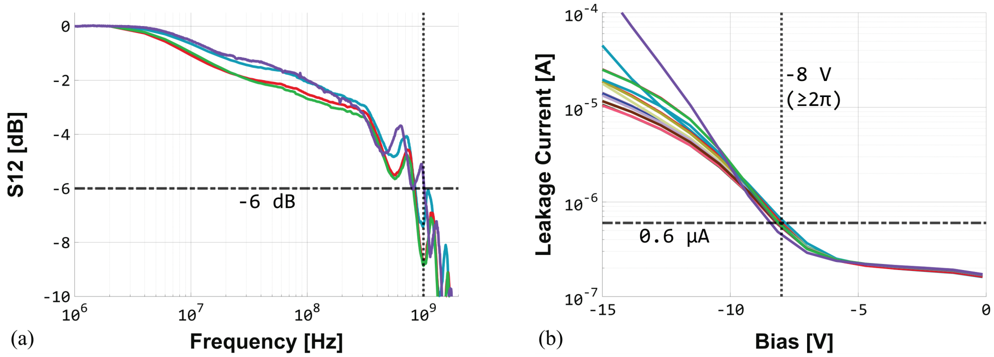

Figure 52: (a) Electro-optical response of 4 channels of a selected PIC. (b) DC leakage current under reverse bias for all 16 channels of a selected PIC.

Direct electro-optical responsivity was characterized at the OPA testing facility by modulating a single channel and measuring the photodiode response at a selected point in the far-field output, demonstrating a 6 dB bandwidth between 770 MHz and 1 GHz for several channels of a selected PIC as shown in Figure 52(a). This agrees with the simulated electrical bandwidth, as power modulation relates to the square of the phase modulation for small signals.

The modulation bandwidth of these 3-mm-long phase modulators is ultimately limited by their capacitance, and is thereby reducible by shortening the modulators. At 1030 nm, modulators only 1 mm long could provide a full 2π phase shift with 1 dB RAM. GaAs is also amenable to traveling-wave electrode designs exceeding 40 GHz bandwidth [122]– [124].

DC electrical testing of the 3-mm-long modulators on a selected PIC, plotted in Figure 52(b), shows leakage currents under 0.6 μA at -8 V bias for all measured modulators, corresponding to less than 5 μW DC power and at least 2π modulation depth at all tested wavelengths. The full 16-channel PIC thus requires under 80 μW to hold any steering angle.

4.8.4 PHASE MODULATOR PERFORMANCE COMPARISON

As indicated in Table 2, the optical and electrical metrics achieved by this OPA-optimized phase modulator design are competitive with most InP, SiPh, and LNOI phase modulators from literature, demonstrating higher speed than SiPh thermal modulators, lower RAM than carrier-injection modulators, and higher $V_\pi \cdot L$ modulation efficiency than LNOI modulators at similar wavelengths.

Table 2: Phase modulator performance comparison.

Year	Platform	Wavelength [nm]	Method [a]	Length [mm]	$V_\pi \cdot L$ [b] [V·cm]	RAM @ 2π [dB]	EO Bandwidth
This work	GaAs	980-1360	EO	3, 4	0.5-1.22	<0.5	1 GHz
2020 [81]	GaAs	980	EO	5	1.15	-	20 MHz
2014 [125]	GaAs	780	EO	2	1.5	-	13 MHz
2013 [126]	GaAs	1550	EO	7	0.42	1	-
2008 [127]	GaAs	1550	EO	7	0.3	<1	-
1998 [128]	GaAs	1310	EO	2	0.52	~3	2.5 GHz [c]
1991 [80]	GaAs	1064	EO	1.8	1.9	-	2 GHz [c]
1990 [84]	GaAs	1090	EO	5.3	1.3	~3	-
2021 [129]	InP	1550	carrier	0.8	0.2 mA·cm	-	1 GHz [c]
2013 [64]	InP	1520-1570	carrier	0.2	0.2 mA·cm	1.5	100 MHz
2023 [59]	InP	1550	EO	3.5	1.02	-	-
2022 [61]	InP	1480-1550	EO	2.5	1.2	<0.5	-
2014 [123]	InP	1550	EO	10	1.6	-	67 GHz
2020 [60]	InP	4600	thermal	2.35	53 mW·cm	-	-
2023 [130]	LNOI	784	EO	8	1.6	-	100 GHz
2023 [131]	LNOI	850	EO	5.5	1.56	-	>20 GHz
2023 [131]	LNOI	1550	EO	5.5	2.58	-	>40 GHz
2023 [132]	LNOI	400-700	EO	8	0.34-0.96	-	>20 GHz
2021 [133]	LNOI	1064	EO	7	3.82	-	-
2018 [134]	LNOI	1550	EO	5	4.4	0.1	100 GHz
2019 [135]	LNOI + SiPh	1550	EO	3	4.4	-	70 GHz
2018 [136]	LNOI + SiPh	1550	EO	5	13.4	-	106 GHz
2020 [41]	SiPh	1550	carrier	0.5	0.03	5	324 MHz
2019 [56]	SiPh + III-V	1450-1650	EO	5	0.18-0.7	0.1-0.15	1.65 GHz
2013 [137]	SiPh	1550	EO	0.75	2	3.2	27 GHz
2008 [138]	SiPh	1550	EO	1	6	2.8	30 GHz
2022 [47]	SiPh	1550	thermal	1.5	0.7 mW·cm	-	18 kHz
2020 [139]	SiPh	488	thermal	-	-	-	50 kHz
2020 [140]	SiPh	1560	thermal	0.5	0.8 mW·cm	-	200 kHz
2019 [53]	SiPh	1550	thermal	-	-	2.4	10 kHz
2018 [141]	SiPh	1550	thermal	0.44	1.1 mW·cm	-	-
2014 [142]	SiPh	1480-1580	thermal	-	-	~0	7.3 kHz
2011 [143]	SiPh	1555	thermal	-	-	-	-

[a] “EO” = electro-optic reverse biased, “carrier” = carrier injection, “thermal” = thermo-optic effect

[b] Single-sided; doubled where push-pull is reported. [c] Not measured, expected RC limit reported.

4.8.5 OPTICAL PHASED ARRAY PERFORMANCE

In the case of this OPA PIC design tested at $\lambda = 1064$ nm, $d = 4$ μm, and $D = (16-1)\cdot d = 60$ μm, the expected steering range is 15° and expected beamwidth is ~1°, and the number of addressable points is ~15. These estimates are confirmed by directly propagating the simulated output facet optical mode to the far field [144]; the simulated steering range is 15.2° with a 0.85° beamwidth for ~17 addressable points, and the simulated SLL is 13 dB as expected for a uniform array.

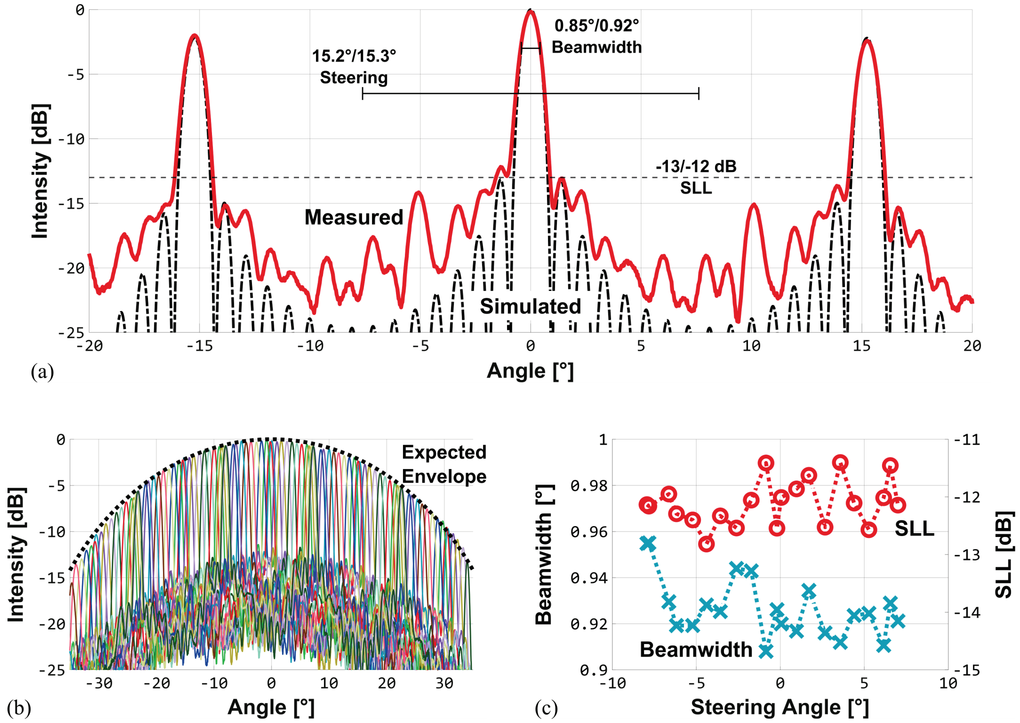

Figure 53: (a) Simulated (black, dashed) and measured (red, solid) beam profiles with indicated simulated/measured beam width, steering range, and sidelobe level. (b) Measured beam profiles at 21 different steering angles (colored, solid), compared to expected envelope (black, dotted). (c) Beamwidth (left, crosses) and sidelobe level (right, circles) at measured steering angles.

A selected OPA PIC was evaluated at the OPA testing facility with the method described in section 3.4.4, and Figure 53(a) shows the measured beam profile at 0° steering compared to the expected performance. Measured beamwidth was 0.92° with 15.3° steering range and 12 dB SLL, differing from simulation by only 8%, 0.7%, and 1 dB respectively. Capturing further beam profiles at additional steering angles, shown in Figure 53(b), the PIC output reproduced the expected envelope and maintained performance with 0.93° ± 0.01° beamwidth and 12.1 ± 0.4 dB SLL across the entire grating-lobe-free steering range as indicated in Figure 53(c).

The slight difference between expected and measured steering range may be due to minor imprecision in the measurement optics, pattern scale errors during fabrication, or a combination. Fabrication scale error is expected to be under 1%. The higher beamwidth and inferior SLL can be partially attributed to slightly mismatched subaperture phases, as indicated by the lack of uniform sidelobes, and nonuniform channel powers.

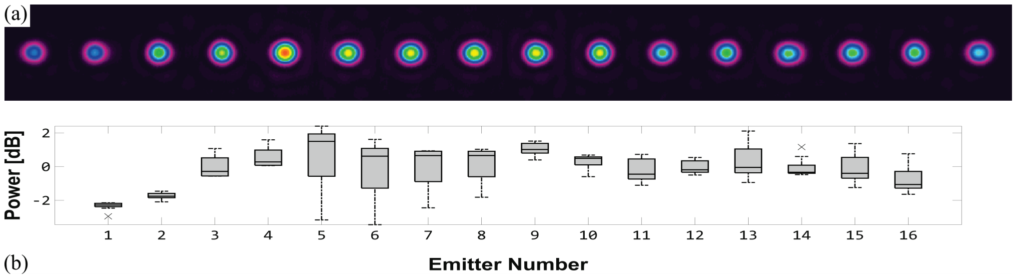

Figure 54: (a) Typical image of PIC output facets. (b) Distribution of per-channel output power for 12 separate input fiber alignments with median (line), 25th to 75th percentile limits (box), 10th to 90th percentile limits (whiskers), and outliers (crosses).

The near field beam profile was also captured. A typical output facet image, Figure 54(a), shows that power is not evenly distributed amongst all channels. The uniformity exhibits dependence on input fiber position: comparing the per-channel output power across 12 different input alignments in Figure 54(b), the mean emitter-to-emitter standard deviation across the array is 1.2 dB, and the mean deviation of a single emitter at different input alignments is 0.76 dB. The variation with input alignment and excess power in the center, taken together, indicates likely multi-mode coupling into the MMI splitter tree.

Table 3: Optical phased array performance comparison.

Year	Platform	Wavelength [nm]	Channels	Steering Range [°]	Beamwidth [°]	Addressable Points	SLL [dB]
This work	GaAs	980 – 1360[a]	16	15.3	0.92	16	12
2020 [81]	GaAs	980	15	30	4.7	6	8
1991 [80]	GaAs	1064	10	20	2	10	-
2023 [59]	InP	1550	32	35	0.46	76	8.2
2022 [63]	InP	1550	30	17	1.49	11	-
2022 [61]	InP	1480 – 1550	8	17.8	2.5	7	12.8
2021 [129]	InP	1550	100	8.88	0.11	80	6.3
2020 [60]	InP	4600	32	23	0.6	38	-
2013 [64]	InP	1520-1570	8	1.7	0.2	8	10
2023 [145]	LNOI	1500-1600	16	24	2	12	10
2023 [146]	SiPh	1550	120	25	0.31	80	15.1
2023 [147]	SiPh	1550	16	120	≥6.6[b]	<18[b]	10.9
2022 [46]	SiPh	1550	8192	100	0.01	10000	10
2022 [47]	SiPh	1550	256	45.6	0.154	296	10.8
2020 [140]	SiPh	1560	32	18	0.63	28	10
2020 [139]	SiPh	488	64	50	0.17	294	6.05
2020 [48]	SiPh	1525-1600	512	70	0.15	467	7.5
2020 [41]	SiPh	1550	8×8	8.9×2.2	0.92×0.32	66	8.8
2019 [56]	SiPh + III-V	1450-1650	32	22, 51	0.78, 1.75	28, 29	16
2019 [148]	SiPh	1550	128 (2D)	16×16	0.8×0.8	400	12
2018 [141]	SiPh	1550	1024	22.5	0.03	750	9
2016 [149]	SiPh	1260 – 1360	128	80	0.14	570	-
2014 [142]	SiPh	1480 – 1580	16	19.6	1.1	17	10
2014 [150]	SiPh	1550	16	51	3.3	15	-
2011 [143]	SiPh	1555	16	14	1.6	8	10

[a] Results reported for 1064 nm. [b] Extracted from reported figure.

The performance of this OPA is comparable to or better than most other results in the literature, as summarized in Table 3. The SLL of 12 dB is close to the theoretical 13 dB ultimate performance of a uniform linear array and better than the majority of reported results. Beam quality for a uniform array can be judged by comparing the number of addressable points to the number of channels, and this PIC compares favorably to other uniform arrays. Nonuniform arrays can achieve higher addressable points by sacrificing SLL. This PIC also demonstrates operation at 1064 nm, which has not been widely demonstrated for OPAs, and is attractive for expanding the potential applications of OPAs.

4.9 Chapter Summary

A 16-channel GaAs-based OPA was successfully produced, with demonstrated 0.92° beamwidth, 15.3° grating-lobe-free steering range, and 12 dB SLL in close agreement with theoretical results and comparable or superior to most other results in the literature. Individual 4-mm-long phase modulators tested from 980 nm to 1360 nm exhibited single-sided $V_\pi \cdot L$ modulation efficiency of 1.22 V·cm and better with under 0.5 dB RAM, surpassing the OPA-relevant performance of most InP, SiPh, and LNOI phase modulators at similar wavelengths. 3-mm-long phase modulators in the OPA show less than 5 μW DC electrical power and greater than 770 MHz electro-optical bandwidth when mounted on a carrier and PCB. The success of this GaAs PIC platform for OPAs demonstrated the feasibility of a monolithic GaAs OPA platform, and set the stage for the active-passive epitaxy in the following Chapter 5 that enables both phase control and per-channel gain.

Chapter 5

Active-Passive OPA PIC

After the successful fabrication and characterization of the OPA PIC with phase control in Chapter 4 demonstrated the feasibility of a GaAs-based OPA PIC, the next step in developing a monolithic GaAs OPA PIC platform was the integration of gain. This required a new epitaxy design and associated redevelopment of the fabrication process and PIC components to support both active and passive devices.

An OPA PIC design based on this active-passive platform was developed, incorporating both phase control and per-channel gain. The light source was kept off-chip to reduce initial development risk. The primary difference between this device and the previous OPA PIC is the integration of SOAs after each channel. These enable the possibility of high total output power with either an external laser or an on-chip integrated laser.

This PIC was restricted to 8 channels to simplify integration and testing by reusing the 16-channel electrical control developed for the OPA PIC presented in Chapter 4, but is readily scalable to significantly higher channel count. Potential scaling limitations are discussed in section 6.6.

5.1 Purpose

This 8-channel PIC was specifically designed to demonstrate the possibility of fully monolithically integrated OPAs on a GaAs platform. Building on the previous device's modulator-optimized epitaxy, it adds an active layer that is suitable for integrated lasers and SOAs. The devices themselves include all required parts of a fully integrated OPA except for the on-chip laser, which was omitted to reduce fabrication risk. Lasers of a compatible design were fabricated in the same process on a different die, discussed in section 5.6, and are straightforwardly integrable with the developed OPA PIC design. The design wavelength of the epitaxy and all structures is 1030 nm.

5.2 Preview of Results

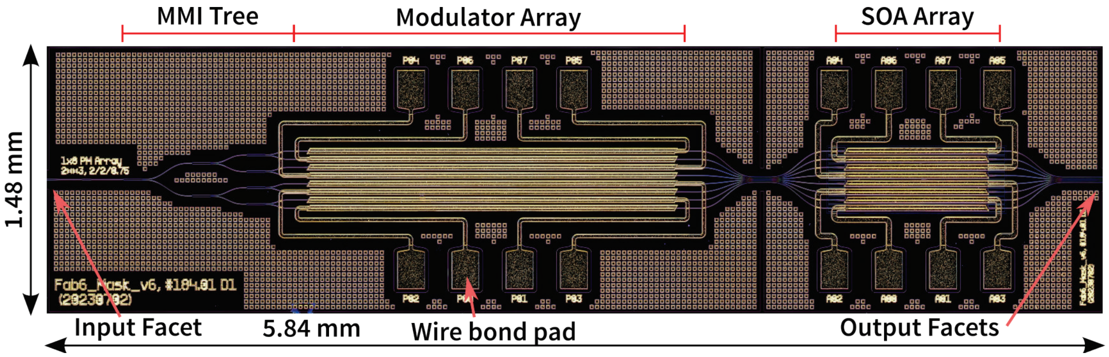

Figure 55: Optical micrograph of fabricated active-passive OPA PIC.

The first design utilizing the new active-passive platform successfully produced devices with a 5.84 mm x 1.48 mm footprint, consisting of an edge-coupled input, a 1x8 splitter, 8 equal channels on a 45 µm pitch with 2-mm-long phase modulators and 750-µm-long SOAs, and a 4-µm-pitch output facet forming a one-dimensional 8-channel optical phased array, as shown in Figure 55. The waveguides consist of a mix of deep ridge and shallow rib waveguides and transitions between the two types. The waveguides are reduced to a 4 μm pitch between the modulator and SOA arrays to provide the option to cleave out either modulator-only or modulator-and-SOA devices.

While the OPA PICs have not yet been fully characterized, initial testing of separate 1-mm-long phase modulators fabricated at the same time demonstrated single-sided $V_\pi \cdot L$ modulation efficiency of 0.8 V·cm at 1030 nm wavelength, although the precision of this result is low. This is worse than the expected 0.6 V·cm efficiency, but further analysis indicated that the realized top cladding contains a lower aluminum content than the design, changing the expected efficiency to 0.7 V·cm, closer to the measured performance. Further characterization of the fabricated device efficiency is expected to improve precision and provide results at additional wavelengths.

5.3 Active-Passive Integration in GaAs

A fully monolithic GaAs OPA PIC requires the integration of active material into the PIC, so some method of active-passive integration is required. In the case of these OPA PICs, the same epitaxy is used for both the passive waveguide regions and the modulator waveguide regions, so only two different areas of epitaxy are required for active-passive integration. This is possible because the modulator waveguide epitaxy was already optimized for low propagation loss.

Common active-passive integration methods for III-V materials include offset quantum wells, selective area regrowth, butt-joint regrowth, and non-regrowth-based quantum well intermixing. Vertical multi-guide or twin-guide platforms are also possible for both active-passive separation and edge-coupled mode conversion, but are less common. These techniques are illustrated in Figure 56 and explained in more detail below. Variations on each method also exist.

Regardless of the method, critical considerations are the modal overlap or alternatively coupling between active and passive regions, and the optical mode overlap with the gain layers in the active section.

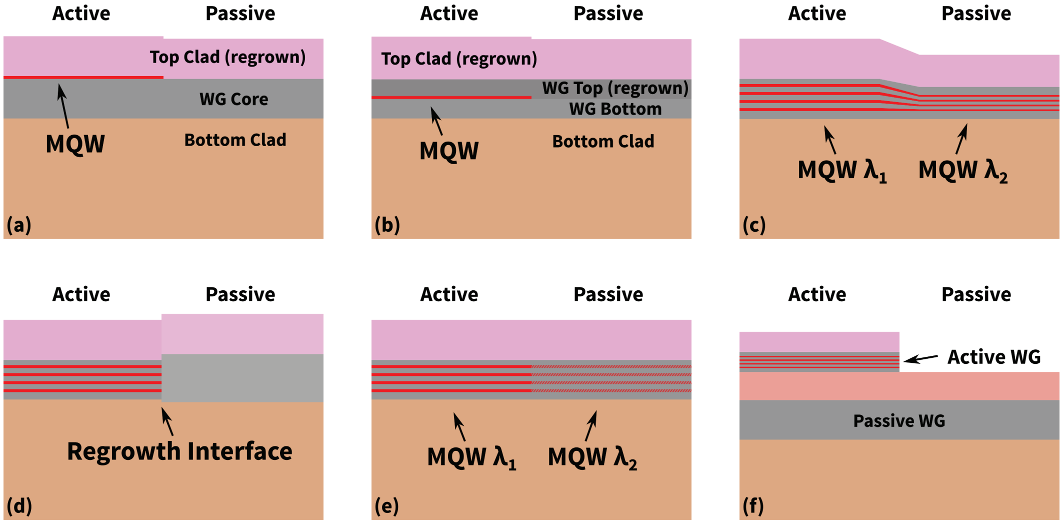

Figure 56: Illustration of different III-V active-passive integration methods: (a) offset quantum wells, (b) centered quantum wells, (c) selective area growth, (d) butt-joint regrowth, (e) quantum well intermixing, (f) vertical twin-guide.

5.3.1 OFFSET QUANTUM WELLS

The offset quantum well method shown in Figure 56(a) is a regrowth approach that utilizes QWs or MQWs located immediately above the waveguide, initially without top cladding. The active material is then selectively removed above the passive regions, and a blanket regrowth deposits the top portion of the epitaxy uniformly above both the active and passive regions, typically top cladding and a p-contact layer.

This method is relatively simple, requiring only a single blanket regrowth step, and the small difference in height between the two regions results in efficient coupling between active and passive waveguides. However, locating the QWs at the edge of the waveguide core typically results in a low overlap between active material and the optical mode, reducing possible modal gain.

A less common variant of this is centered quantum wells as in Figure 56(b), where the same process occurs but the top half of the waveguide core is part of the blanket regrowth. This moves the QWs to the peak of the optical mode and thereby improves QW confinement, but requires a high quality regrowth to avoid adding excess optical loss at the regrowth interface in the waveguide core. This is the approach adopted below in section 5.4.

5.3.2 SELECTIVE AREA GROWTH

In the selective area growth method shown in Figure 56(c), the wafer is patterned with a dielectric mask before the waveguide core and MQW regions are grown. This takes advantage of differing transport properties of the growth reactants in proximity to the dielectric patterns and dielectric fill factor, enabling different growth rates of materials in different regions. This can shift the bandgap of the MQW in selected areas to be shorter than the operational wavelength, allowing passive propagation in that region, without any regrowth interfaces in the waveguide core or MQW regions. The primary drawbacks of this method are the limited range of bandgap shift that can be achieved, as well as the careful calibration required for the dielectric mask.

5.3.3 BUTT-JOINT REGROWTH

The butt-joint regrowth method shown in Figure 56(d) is a commonly used technique due to the flexibility it provides in per-component epitaxy design combined with high coupling between components [151]. Multiple regrowth steps are required for this approach: first, the entire active region epitaxy including top cladding is grown as the original epitaxy. The active regions are then selectively removed where they are undesired, with the desired regions keeping an SiO2 mask. Secondly, the passive waveguide sections are grown from the bottom cladding up to the same height as the first growth, selectively growing in the unmasked regions; this enables a completely separate passive epitaxy, typically with much lower or no intentional doping to reduce free carrier absorption in the passive sections. This process can be repeated as many times as desired for multiple different component-level epitaxies. Finally, any remaining top cladding or p-contact layers are deposited with a blanket regrowth step.

Drawbacks of this method include the complexity and potential yield concerns arising from many regrowth steps, as well difficulties that can arise from growth at the borders of different regions. However, large semiconductor foundries with highly repeatable processes prefer it for the flexibility it provides in terms of component design [152].

5.3.4 QUANTUM WELL INTERMIXING

Quantum well intermixing, shown in Figure 56(e), is an active-passive integration method that avoids any regrowth steps. Starting with a uniform active epitaxy, selective areas are exposed to ion implantation and high temperature annealing that induces diffusion between the QW layers, altering the structure and shifting the bandgap of the QWs to higher energies. The absorption band of the intermixed regions is thus moved away from the design wavelength, creating passive waveguide regions [153]. Multiple different bandgap regions can also be created by repeated application of the ion implantation and annealing process [152].

Since there is no regrowth or etching involved in this process, there is no discontinuity between the active and passive regions, and so they suffer negligible transition loss. However, careful calibration and control of the intermixing process is required to avoid variation between and within samples, and the maximum bandgap shift is limited.

5.3.5 VERTICAL MULTI-GUIDE

Vertical twin-guide or multi-guide active-passive integration, shown in Figure 56(f), utilizes multiple independently designed waveguide layers that are vertically offset from one another [154]– [160]. In this way individual waveguides can be optimized for specific applications without needing to match modes or be concerned with implications of regrowth across the boundaries. The processing complexity and possible interface issues associated with regrowth steps are also eliminated. However, potentially complex couplers for vertical transitions must be developed in tandem with the final epitaxial design, and additional processing steps are generally required to fabricate these.

While this technique has been explored for decades, the complexity of vertical transition elements compared to the ease of multiple-regrowth methods in large well-controlled foundries has prevented significant uptake for industrial use. It remains a niche technique most useful for smaller facilities without well controlled regrowth capability.

5.4 Active-Passive Epitaxy Design

For this active-passive design, two of the simpler active-passive integration methods were studied: selective MQW removal with a blanket regrowth, and a twin-guide structure.

Several potential twin guide structures were explored through epitaxy and process development up to the component design stage, with reasonable performance simulated for several components, but the complexity of vertical transitions was high. Due to the high vertical transition complexity and significant change in overall structure from the previous modulator and passive epitaxy, which required significant process design changes, the risk and timeline of a twin guide design was determined to be too high compared to other active-passive integration methods. Future developments may better explore a twin guide design with more time to devote to earlier stages of process development and test.

A selective MQW removal with blanket regrowth processes was selected due to its reasonable processing simplicity with in-house MOCVD regrowth and its resulting similarity to the previous epitaxy, enabling design and process reuse. After detailed exploration of potential epitaxial structures and resulting components, a *centered* MQW design was selected, where the top half of the guiding region is also regrown. While this is unusual, the thick guiding region selected for an optimal phase modulation structure with low propagation loss results in a significantly lower optical overlap with the MQW structure than is typical for active designs. With the centered MQW epitaxy described below, the gain overlap is still only 3.5%. Offsetting the MQWs to the top of the guiding region reduces the overlap to an unusably low value.

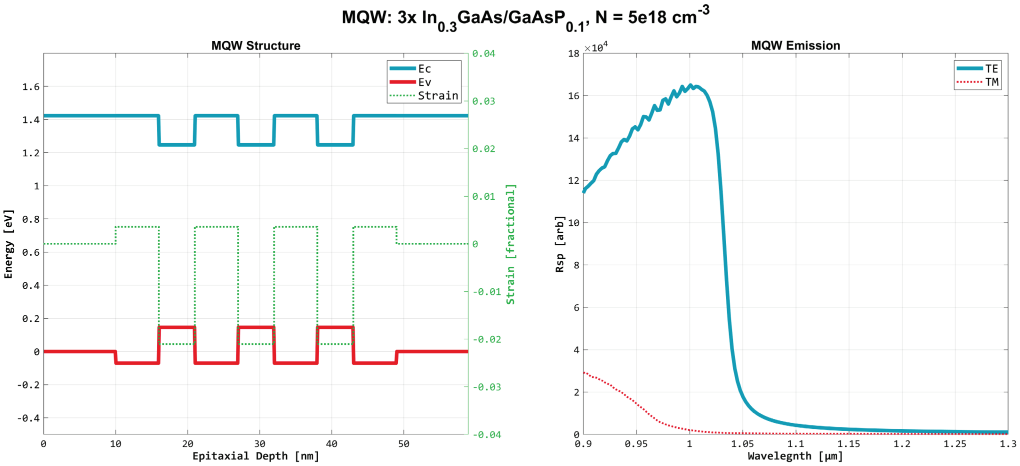

Figure 57: MQW simulation results for the active-passive epitaxy, including the band structure (left), strain (left, dotted green), and the spontaneous emission spectrum (right) at an arbitrarily-selected 5e18 cm^{-3} carrier density.

The active layer was developed for a targeted operational wavelength of 1030 nm. Common designs in the 880 nm to 1100 nm range use strained $In_xGa_{1-x}As$ quantum wells [72]. Based on previous work at the same 1030 nm design wavelength [70], [161], [162], similar QW parameters were explored using the methods detailed in section 3.1.4. 5 nm thick QWs with approximately 30% indium content were selected, and barriers were chosen to have 10% phosphide content and 6 nm thickness to provide strain compensation, resulting in a

$GaAs_{0.90}P/In_{0.30}GaAs$ MQW design with an approximately 1020 nm photoluminescence (PL) peak, selected to target optimal 1030 nm operation under self-heating during operation. Three QWs were chosen for the MQW layer to provide reasonable gain while avoiding potential cumulative strain from higher numbers of QWs. The simulated band structure and PL emission with moderate current injection are shown in Figure 57. The final indium composition was tuned during MOCVD growth by the epitaxial vendor to hit the PL target, resulting in $In_{0.262}GaAs$ QWs in the target.

The optical guiding layers for this epitaxy are significantly thicker than typical gain epitaxies due to their dual-use as electro-optic phase modulators and passive waveguides, so a centered MQW was selected instead of a more-typical offset MQW design in order to increase modal overlap with the gain region. The active regions are formed in areas where the MQWs are not removed, with the regrowth occurring directly on top of the original epitaxy. This creates a double heterostructure with centered MQWs. The guiding layers are lightly p- and n-doped at $10^{-16}\ \mathrm{cm}^{-3}$ to provide electrical conductivity to the MQW layer while keeping optical propagation losses as low as possible and enabling the UID-like operation that is necessary for the reverse biased phase modulators.

The passive and modulator regions are formed where the MQWs are selectively removed by an etch process, and are thus composed of the portion of the pre-regrowth epitaxy that is not removed and the regrown layers on top. Together these constitute a GaAs-based P-p-i-n-N double heterostructure for reverse biased operation that is very similar to the previous modulator-optimized epitaxy.

Table 4: Active-Passive OPA PIC epitaxial layer structure.

Description	Material	Thickness [nm]	Doping [cm^{-3}]
Upper contact [R]	GaAs [R]	200	(p) 1e19
Upper cladding [R]	$Al_{0.3}Ga_{0.7}As$ [R]	900	(p) 2e17
P electrode [R]	GaAs [R]	100	(p) 1e17
Upper guide [R]	GaAs [R]	300	(p) 5e16
MQW cap [SR]	GaAs [SR]	10	(p) 5e16
MQW (N=3) [SR]	$GaAs_{0.90}P_{0.10}/In_{0.262}Ga_{0.738}As$ [SR]	39	UID
Lower guide	GaAs	300	(n) 5e16
N electrode	GaAs	100	(n) 1e17
Lower cladding	$Al_{0.3}Ga_{0.7}As$	1000	(n) 2e17
Buffer	GaAs	1500	(n) 3e18
Substrate	GaAs	650 µm	n-type

[SR] = Selectively removed, [R] = Regrown

The finalized active-passive epitaxy is optimized for phase modulator performance, easy active-passive processing, and active-region performance as needed for OPA applications. This includes low propagation loss, low RAM and high electro-optical bandwidth in the phase modulators, moderate gain overlap in the active region for high SOA gain combined with high saturation power, and a gain peak near the 1030 nm design wavelength. The epitaxial structure is detailed in Table 4.

5.5 Component Design

This active-passive design uses both shallow rib and deep ridge waveguides. The deep ridge construction is used for passive waveguides and phase modulators, similar to the previous design without gain. A shallow rib design with a rib etch that does not penetrate the optically guiding region is used for active regions, both to avoid carrier recombination on sidewalls for efficient gain and to increase the modal area for higher saturation power.

Schematic cross sections of the active, passive, and modulating waveguides are shown in Figure 58, and optical and electrical simulations are shown in Figure 59.

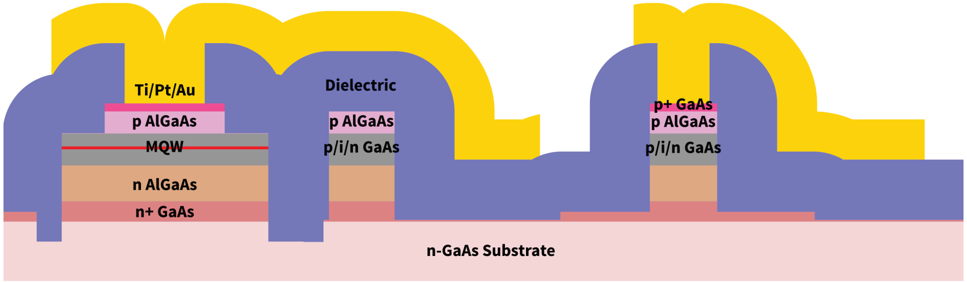

Figure 58: Cross-section schematic of active-passive epitaxy and waveguide structures.

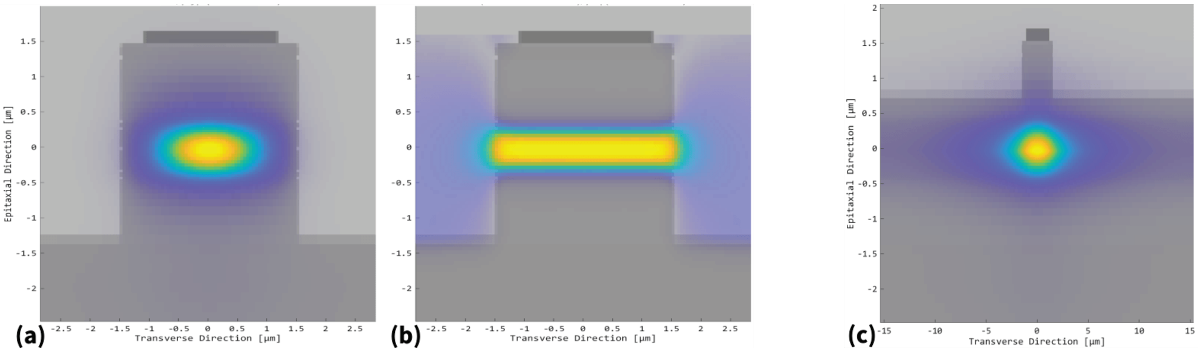

Figure 59: (a) Simulated fundamental TE optical mode of phase modulator waveguides (color) and waveguide structure (shaded grey). (b) Simulated electrical field of phase modulator at -10 V bias. (c) Simulated optical mode of active region, note different horizontal scale.

5.5.1 PASSIVE WAVEGUIDES

The passive waveguides are formed by a single deep ridge etch of at least 2.7 µm. A 1.5-µm-thick material composed of alternating layers of silicon dioxide (SiO_2) and silicon nitride (SiN) is present over the entire PIC to provide electrical passivation and isolation, and protection from environmental effects.

A 2 µm waveguide width is chosen for the passive waveguides, similar to the previous design. These passive waveguides are used to route the light between other components.

One device in each die uses 1.5-µm-wide passive waveguides in case they show better performance. All portions of these passive waveguides have the highly conductive top p-GaAs layer removed in order to electrically isolate them from the active and modulating waveguide segments. The center waveguide in Figure 58 illustrates the cross-section of this passive waveguide. The fundamental TE mode of the passive waveguides is very similar to that of the 3-µm-wide modulating waveguide in Figure 59(a). For the 2-µm-wide waveguides, the fundamental TE optical mode has a $1/e^2$ Gaussian MFD of approximately 1.0 µm in the vertical direction (normal to the epitaxial surface), and 1.5 µm in the lateral direction (parallel to the surface), with an effective mode area of 1.24 μm^2. Passive waveguide loss is expected to be 6.5 dB/cm, dominated by interaction with doped layers.

5.5.2 PHASE MODULATORS

The phase modulators are implemented by the same waveguide structure as the deep ridge passive waveguides, with the addition of P-contacts on top and an N-contact on the back side of the thinned, conductive substrate. A width of 3 µm was selected for the phase modulators in this design to robustly guarantee that the P-vias are aligned on top of the waveguides. They are connected to passive waveguides with 30-µm-long adiabatic tapers.

Vias through the isolation material are formed on top of the phase modulator ridges to access the P-contacts, and routing to wire bond pads is achieved by metal deposited on top of the isolation material, as shown on the right half of Figure 58.

A p-i-n diode is thus formed vertically through the waveguide, with the P-contact on top connected through the top p-AlGaAs cladding to the p-GaAs, the N-contact connected through the substrate and lower n-AlGaAs cladding to the n-GaAs, and the lightly doped middle GaAs layers forming the intrinsic region as the optical guiding layer. When reverse biased, this gives rise to the nearly linear electric field overlapping the optical mode shown in Figure 59(b).

Using the simulated optical and electrical fields shown in Figure 59(a,b) and the methods to determine the phase modulation described in section 3.1.3, at -10 V bias the expected phase modulation of the TE0 mode is 5.0 rad/mm with 0.24 dB/mm RAM.

5.5.3 ACTIVE REGIONS

For increased effective mode area and reduced sidewall interaction, the active regions are formed by shallow rib waveguides with a 3 μm width and ~0.8 μm rib etch depth, as shown in the left half of Figure 58 and in Figure 59(c). The final implementation uses a 34 μm mesa width, which is wider than the extent of any expected fundamental optical mode.

The expected MQW overlap is 3.5% to 3.6%, depending on the exact shallow rib depth between 0.75 μm and 1.0 μm. The $1/e^2$ Gaussian MFD is 1.0 μm in the vertical direction and nominally 3.5 μm in the lateral direction, but this varies significantly with exact shallow rib etch depth. Effective modal areas are 3.4-9 μm^2 depending on rib etch depth.

With this geometry and the selected MQW structure, the simulation method detailed in section 3.1.4 predicts the gain of a 750-μm-long SOA with 5 mW optical input power to be roughly 15 dB at 5 kA/cm^2 current density. The full gain curve is shown in Figure 60, along with the assumed material gain from the MQW simulation of section 5.4.

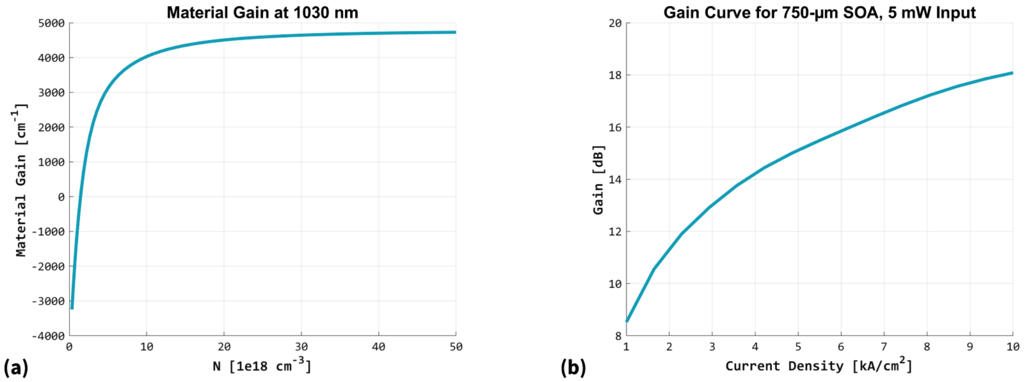

Figure 60: Inputs and results from SOA simulations, showing (a) assumed material gain for a given wavelength and 3 QW configuration, and (b) resulting gain curve assuming 5 mW input and 750 μm device length.

5.5.4 ADDITIONAL COMPONENTS

Several additional components are necessary in addition to passive waveguides, phase modulators, and SOAs.

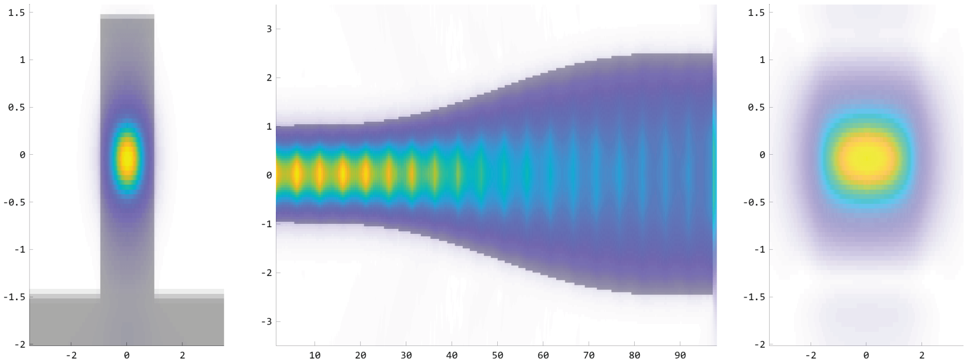

Figure 61: 3D FDTD simulation of spot size converter from 2 μm wide deep ridge waveguide to optimally match a 2 μm MFD lensed fiber, with an expected 2.85 dB IL and 0.4 dB EL; deep ridge cross-section (left), plan view (middle), and output cross-section (right).

Cleaved waveguide facets with AR coating form the single input and 8 outputs. Input light is edge-coupled from a lensed fiber with a 2 μm spot size. As this couples poorly to a

2-μm-wide waveguide, with an expected 5 dB coupling loss, a spot size converter is created by using a 5-μm-wide waveguide at the input facet and tapering it to the nominal 2 μm width over a 60 μm length, resulting in a spot size converter with an expected 2.85 dB coupling loss as shown in Figure 61.

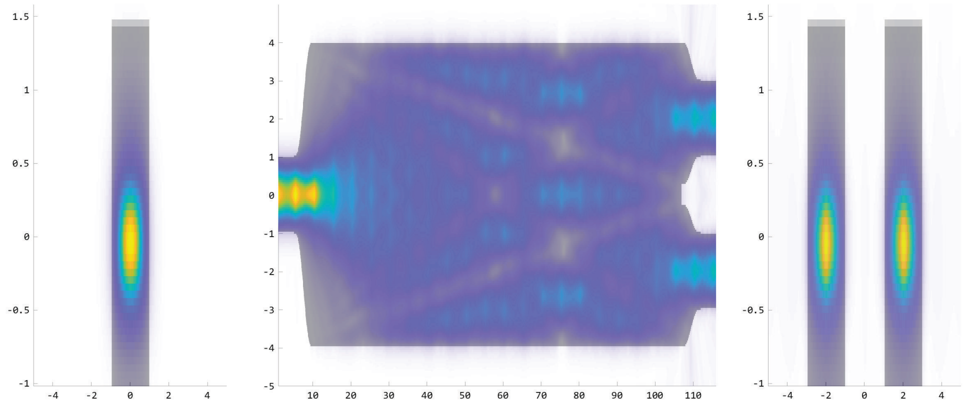

Figure 62: 3D FDTD simulation of 1x2 MMI splitter with expected 0.03 dB IL; single input cross-section (left), plan view (middle), and dual output cross-section (right).

The 1x2 MMI splitters forming the 1x8 splitter share the same structure as the passive waveguides, with geometry initially determined by standard high contrast MMI ratios [121]. 3D FDTD simulation of the epitaxial structure was used to slightly modify the geometry for optimal performance. An FDTD simulation of the resulting geometry is shown in Figure 62.

Differing from the previous design with only passive and modulator waveguides, the active-passive design also requires conversion between shallow rib waveguides and deep ridge waveguides. To achieve this, a double-taper structure was developed, with a rapid taper from mesa width to 6 μm width over a 10 μm length, followed by a slow taper down to a 2 μm width over a 90 μm length, as shown in Figure 63. This shallow-deep transition

(SDT) structure has an expected insertion loss under 0.04 dB, although fabrication imperfections will likely result in higher losses.

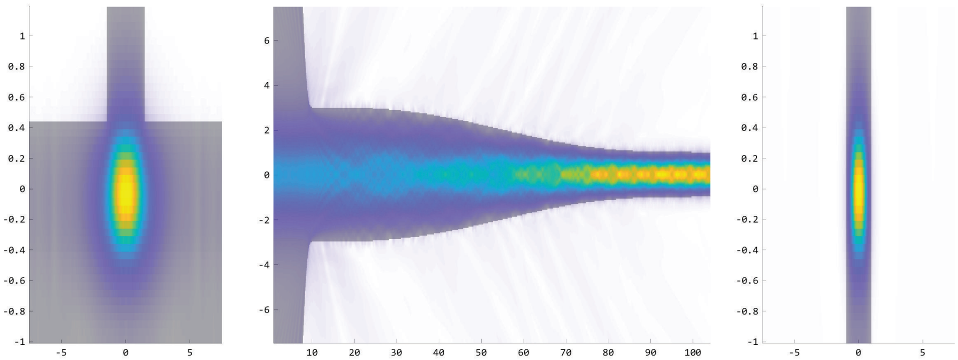

Figure 63: 3D FDTD simulation of SDT with expected <0.04 dB IL; shallow input cross-section (left), plan view (middle), and output cross-section (right).

5.6 High-Order Lasers

Several potential laser designs were developed for inclusion in the active-passive fabrication. Using the techniques described in section 3.1.4 to simulate MQW performance and predict laser performance, three different types of lasers were designed, modeled, and laid out as test structures in the active-passive fabrication. All three designs utilized high-order Bragg gratings with grating period $\Delta_{\mathrm{gr}} = \frac{N\,\lambda}{2\,n_{eff}}$ and order $N = 9$ to form either distributed Bragg reflector (DBR) mirrors or create distributed feedback (DFB) lasers.

5.6.1 PURPOSE

The purpose of using high order gratings instead of first-order gratings is to simplify the fabrication process. First-order gratings for 1030 nm light in GaAs waveguides have a half-period or minimum feature size of approximately 0.07 µm, and thus require the use of electron-beam lithography as a separate processing step. 9th-order gratings, however, have feature sizes of 0.66 µm. This is fabricable with careful i-line lithography, which allows a single lithographic mask to simultaneously define the laser gratings and waveguides. Previous research has used high-order gratings for the same reason [163], [164].

5.6.2 DESIGN

Prior to simulating laser grating designs, the achievable lithographic resolution of the i-line lithography tools was measured. Resolution test patterns were fabricated using the full lithography and etching process, and then SEM imaged. The lithographic process was also computationally simulated by a combination of Gaussian kernel convolution followed by greyscale thresholding. A variety of simulated values were compared to the real patterns, as shown in Figure 64. The achievable resolution with the available i-line lithographic instruments is estimated to be 0.6 µm to 0.8 µm depending on the exact process.

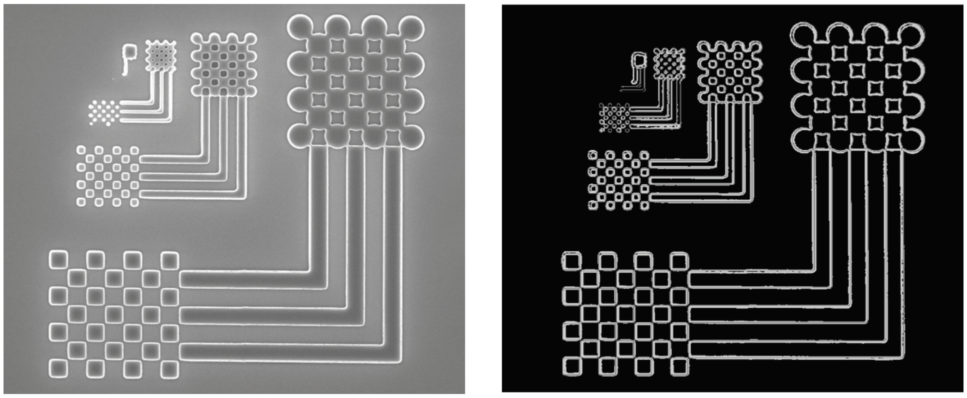

Figure 64: Lithographic resolution test pattern, with SEM image (left) and simulated 0.7 µm Gaussian spot size convolution followed by 60% thresholding (right).

The achievable resolution was then used to set the minimum feature size, which determined a 9th-order grating as the smallest practically reproducible grating period.

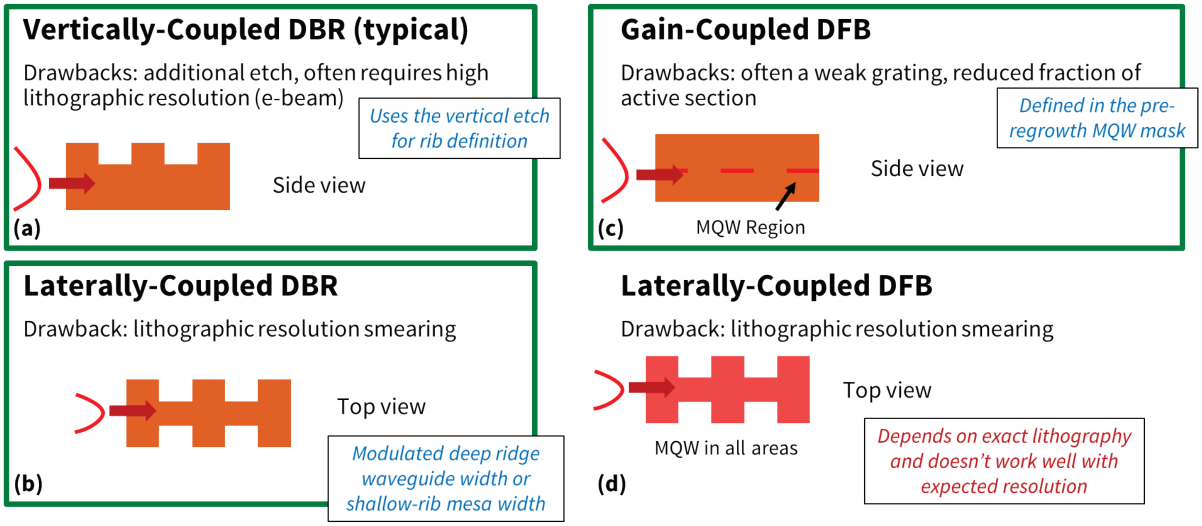

Figure 65: Diagram of DBR (left) and DFB (right) gratings: (a) vertically-coupled DBRs utilizing waveguide height variation, (b) laterally-coupled DBR utilizing waveguide width variation, (c) gain-coupled DFB utilizing MQW presence variation, and (d) laterally-coupled DFB using laser waveguide width variation. Methods (a), (b), and (c) were selected for inclusion on this fabrication due to their expected achievability.

Several varieties of laser mirror gratings were then explored, illustrated in Figure 65. DBR gratings are typically implemented as vertically coupled structures where alterations of the waveguide height produce the effective refractive index changes required for accumulated reflections [111]. These often require an additional etch to define the gratings. Laterally coupled DBR gratings, using a modulated waveguide width to produce effective refractive index differences [165]– [169], are able to simplify fabrication by using the waveguide-defining etch to form the grating. These structures can also form DFBs. Gain-coupled DFBs modulate the presence or absence of gain material to form the grating.

Each of these were simulated via TMM as discussed in section 3.1.4. To determine the appropriate reflection and transmission coefficients, a few different specific methods were used. For the gain-coupled DFB, straight waveguide segments with the complex effective index of the passive and active waveguides were used. For the vertically coupled DBR, a single period of each grating variation was simulated with Lumerical EME [82] to determine the unit-cell reflection and transmission across a range of potential etch depths, assuming that fabrication would faithfully reproduce the straight boundaries.

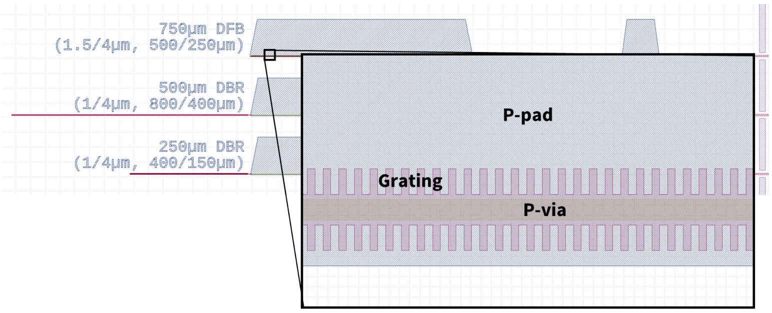

Figure 66: Ideal geometry of 9th-order laterally-coupled DFB and DBR design.

For the laterally coupled structures, however, a more complex scheme was used. First the effective index of the waveguide at varying widths was simulated and fit to a simple empirical function. The physical geometry of each variation of laterally coupled designs was then produced, with an example illustrated in Figure 66. This ideal geometry was then convolved with a Gaussian kernel of the estimated achievable resolution, and the achievable width as a function of distance was determined, as shown in Figure 67.

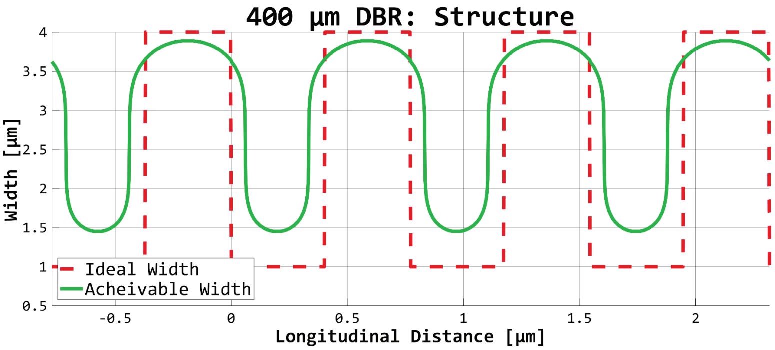

Figure 67: Simulated ideal and achievable laterally-coupled DBR geometry with realistic 0.8-μm-MFD i-line stepper resolution.

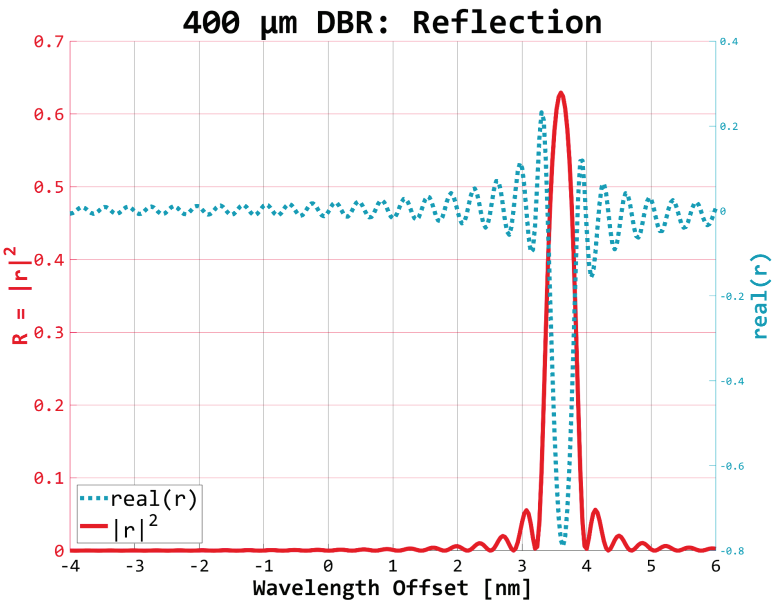

Figure 68: Simulated reflection spectrum of lithographically-achievable 9th-order deep-ridge laterally-coupled DBR with 400 µm length.

The reflection and transmission coefficients of the entire mirror were then calculated by finely discretizing the longitudinal distance and using the waveguide width and associated effective index at each point to perform the transmission matrix calculations, resulting in expected physically-realizable reflection spectra as shown in Figure 68.

After exploring the design parameter space of each type of grating design, including grating order, etch depth, waveguide widths, and potential variations in lithographic resolution, three laser designs were selected. A vertically coupled DBR using the shallow rib etch (discussed below in section 5.8) to define the gratings, a laterally coupled DBR using modulation of shallow-rib waveguide mesa widths, and a gain-coupled DFB were determined to have potentially realizable performance. Each design was implemented as test structures with several length variations.

5.7 Mask Layout

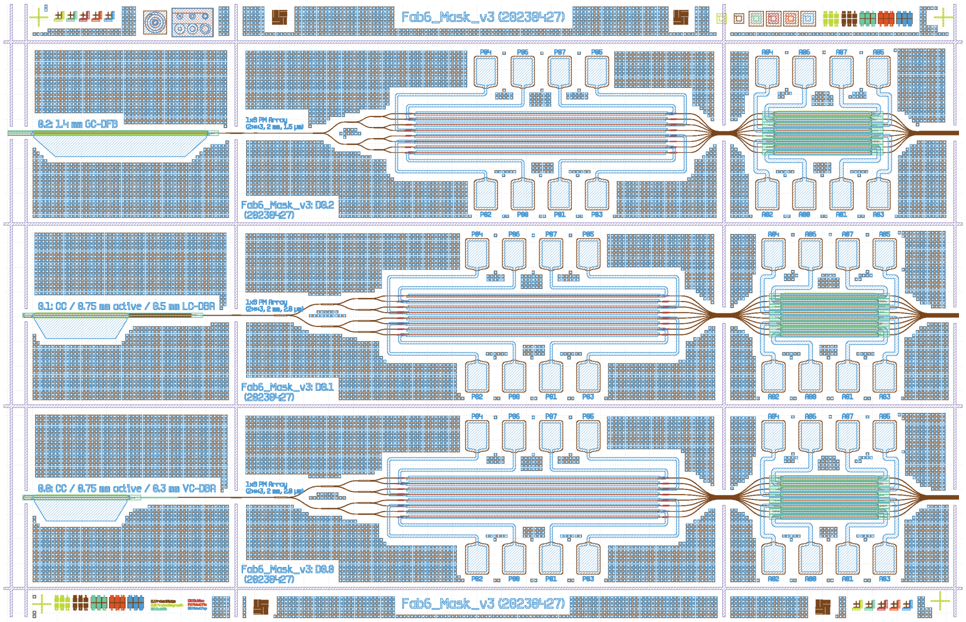

Figure 69: Active-passive design mask geometry for one die.

These components were assembled together into a 7.7 mm x 5 mm die, shown in Figure 69. Each die contains 3 separate 8-channel devices. Differing from the previous design, these devices also include experimental 9th-order DBR or DFB lasers before the phase modulators, with 3 laser variations per die, although to reduce the risk of this fabrication these were removed before final postprocessing. Following the lasers, each 8-channel device consists of an optional cleave lane with a spot-size converter for the potential edge-coupled input, a 1x8 splitter, 8 equal channels on a 45 µm pitch with 2-mm-long phase modulators with wire bond pads broken out to the sides, and 750-µm-long SOAs with wire bond pads broken out to the sides. All channels are collapsed to a dense 4-µm-pitch between the phase modulators and SOAs as well as after the SOAs, such that the output facet can be formed either before or after the SOAs.

5.8 *Fabrication Process*

Compared to the previous design, the process in the active-passive design was both more and less complex. The double-layer metallization and isolation from the previous design was dropped for simplicity, with electrical connections to the wire bond pads made from the ends of the devices instead of crossing devices. However, there were additional requirements from the MQW selective removal etch and integration of shallow rib waveguide segments that increased complexity.

The final fabrication process consisted of six masks, four GaAs etches, and one metal lift-off step. Figure 80 shows schematic diagrams of the primary fabrication process steps.

(a) Initial epitaxy with hard mask and photoresist

(b) MQW etch

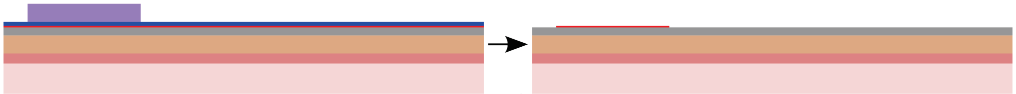

(c) Blanket regrowth

(d) Shallow rib etch

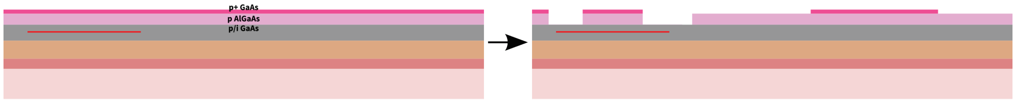

(e) PR and hard mask etch for deep ridge pattern

(f) BHF dip for sidewall hard mask removal

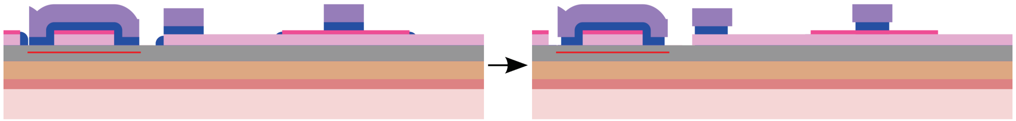

(g) Deep ridge etch, passivation, and P-via

(h) Top metal deposition and lift-off

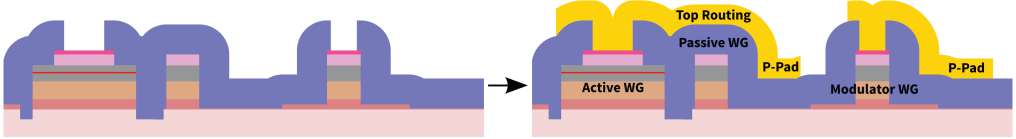

Figure 70: Schematic diagrams of primary fabrication process steps. (a) Initial epitaxy with hard mask (blue) and patterned photoresist (purple). (b) MQW etch. (c) Blanket regrowth. (d) Shallow rib etch. (e) Hard mask etch for deep ridge layer, note remaining hard mask (blue) on sidewalls. (f) 10 s long BHF soak to remove remaining hard mask from sidewalls. (g) Deep ridge etch and dielectric layer deposition (light blue). (h) Top metal (yellow) after lift-off including P-metal and routing.

The process begins with the deposition of a 200 nm SiO_2 hard mask on clean epitaxy via PECVD. Photoresist is patterned on top of this by the MLA150 maskless aligner, defining alignment marks. These alignment marks are etched into the hard mask by ICP-RIE with CHF_3/CF_4 chemistry, and remaining photoresist is removed. Photoresist is again patterned on top of the hard mask with an i-line stepper, defining the MQW region. Unprotected regions of the hard mask are then removed by ICP-RIE with CHF_3/CF_4 chemistry as shown in Figure 71(a), and the MQW layer outside of the areas protected by hard mask is removed by a 55-nm-deep $Cl_2/H_2/Ar/CH_4$ ICP-RIE etch, shown in Figure 71(b). After removing the hard mask with BHF, the surface is oxidized with a UV ozone generation tool in preparation for regrowth. Immediately before regrowth, the surface oxide is removed with a short BHF soak and the samples are loaded into an MOCVD reactor. The top III-V layers are then deposited by a MOCVD blanket regrowth process. Note that the MOCVD reactor can only hold two samples at a time, so they were regrown in pairs.

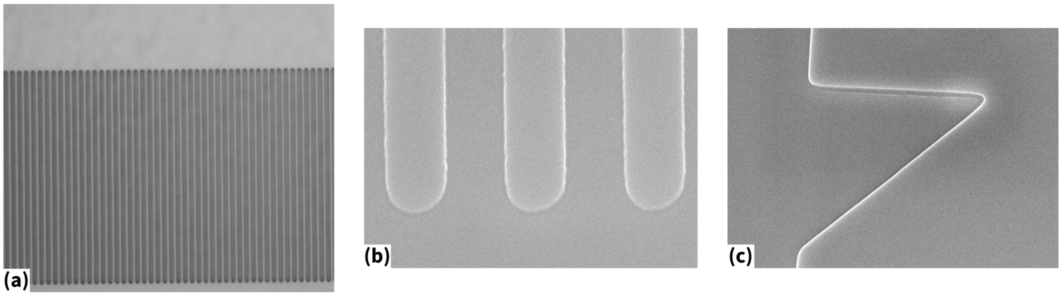

Figure 71: (a) Micrograph of a 9th-order DFB MQW grating with a ~1.2 μm period defined by etched hard mask. (b) SEM image of the resulting MQW regions after the 55-nm-deep MQW etch. (c) SEM image of the isolation region border, with an angled interface transition over future waveguide location.

After regrowth, the top p+GaAs layer is removed outside of modulator and active regions by a combination of a photoresist mask, MLA150 maskless aligner lithography, and

200-nm-deep ICP-RIE etch with $BCl_3/SF_6/N_2$ chemistry, with a result shown in Figure 71(c). The shallow rib etch regions are then defined with photoresist and i-line lithography, and etched by a timed Cl_2/N_2 ICP-RIE etch, with typical results as shown in Figure 72(a). 400 nm of hard mask is then deposited via PECVD and patterned with photoresist and i-line lithography, followed by CHF_3/CF_4 ICP-RIE etching to expose the III-V surface in the deep ridge pattern. To remove the hard mask that remains on vertical features from the shallow rib etch, a 10 s long BHF soak is performed, resulting in a slightly undercut hard mask under the photoresist as in Figure 72(b); unfortunately narrow structures are sometimes lifted free by this as shown in Figure 72(c).

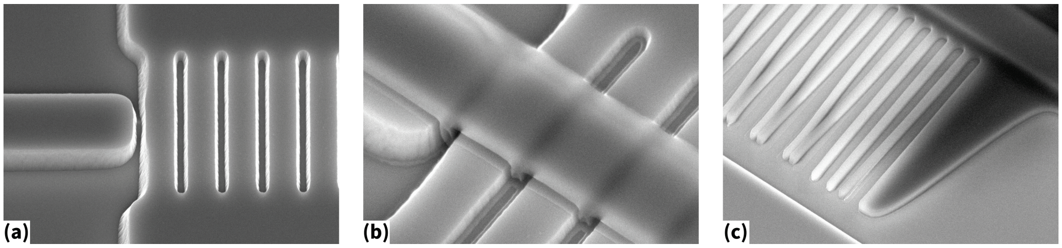

Figure 72: (a) Vertically coupled DBR grating after shallow rib etch. (b) Photoresist and undercut hard mask for deep ridge etch mask after 10 s long BHF soak. (c) Disrupted laterally coupled DBR structure after 10 s long BHF soak.

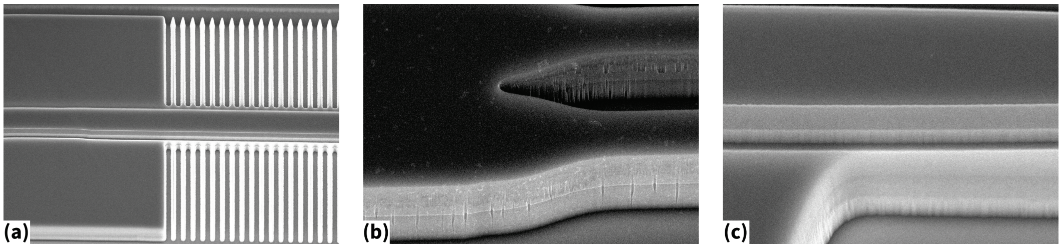

Figure 73: SEM images of structures after deep ridge etch: (a) LC-DBR mirror with modulated mesa width, (b) 1x2 MMI output, (c) corner of SDT structure.

The photoresist is then removed, deep ridges are formed with a timed Cl_2/N_2 ICP-RIE etch, and the hard mask is removed by a BHF soak, resulting in deep ridge structures with typical results shown in Figure 73. The observed differences are due to varying etch quality from run to run in the utilized Panasonic ICP tool.

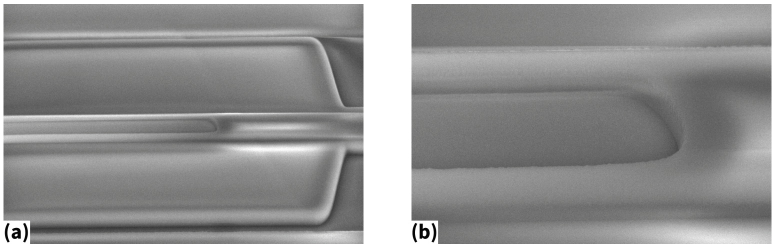

Figure 74: (a) SOA and beginning of SDT structure with 1.5-μm-thick dielectric isolation layer applied and opened top via. (b) Closeup of opened via.

The samples are then passivated with 5 nm Al_2O_3 and 10 nm SiO_2 by atomic layer deposition, on top of which the dielectric isolation layer of 1.5 μm total thickness is deposited in alternating SiO_2 and SiN layers via PECVD. The SiO_2 and SiN layer thicknesses are selected to reduce net strain as best as possible. This isolation layer is selectively opened above the modulator and active waveguides and cleave lanes by a photoresist mask, MLA150 maskless lithography, and a CHF_3/CF_4 ICP-RIE etch, shown in Figure 74.

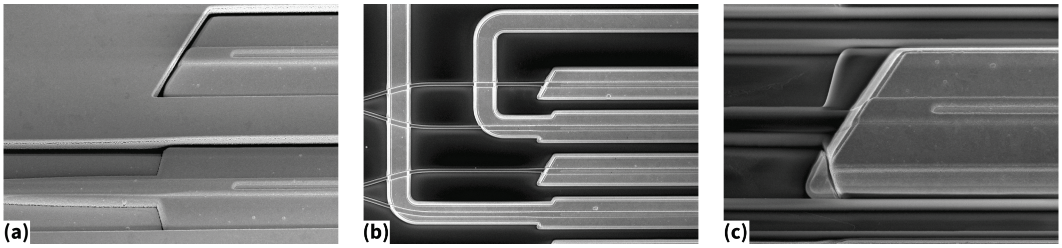

Figure 75: (a) Sample after metal deposition, before lift-off. (b) Top metal traces after lift-off. (c) Metal pad over SOA after lift-off.

A lift-off mask is defined with bi-layer photoresist and MLA150 maskless lithography, on top of which 20/40/4000 nm of Ti/Pt/Au is deposited by electron beam deposition, using a rotating chuck angled at ~30° off normal incidence to promote sidewall coverage, with typical results shown in Figure 75(a). The metal is then lifted off to define the metal layer, forming the modulators' top metal contacts as well as the routing metal, shown in Figure 75(b,c). An unusually thick metal layer was selected to guarantee connectivity where the top metal traces route over deep ridge edges; due to self-shadowing during deposition, these regions as shown in Figure 76 often have small crevices with less clear connectivity. To complete fabrication, the substrate is thinned to approximately 200 µm, 10/50/100/20/500 nm of Ni/Ge/Au/Ni/Au N-metal is deposited on the back side, and devices are rapidly thermally annealed in forming gas at 400°C then 480°C for 10 seconds each.

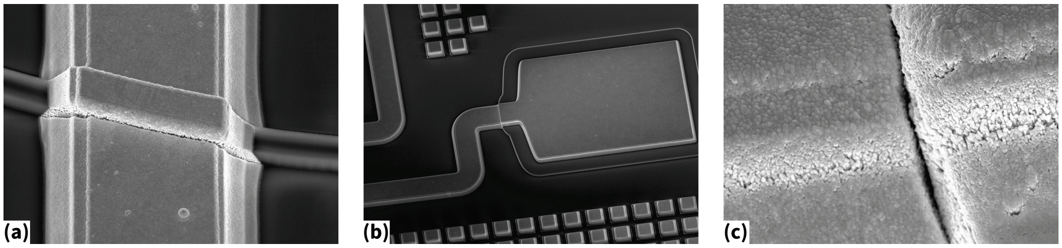

Figure 76: (a) Top metal routing over waveguide. (b) Top metal trace leading to raised wire bond pad(c) Close-up of transition across height step showing crevice.

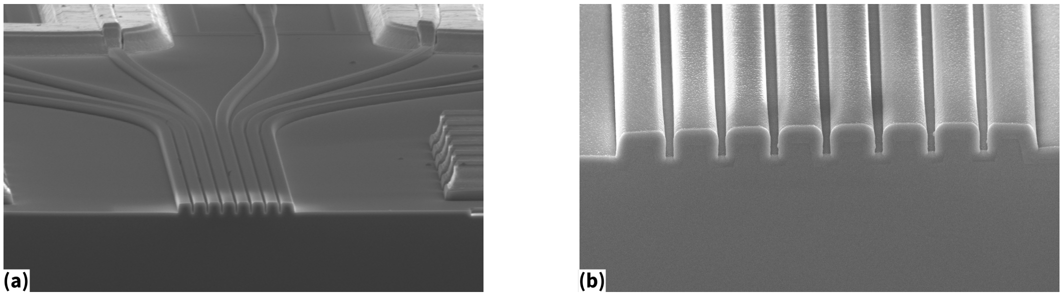

Figure 77: SEM image of AR-coated output facet of singulated device: (a) wide isometric view of facet and nearby waveguide routing, and (b) close view of facet.

After electrical testing to determine initial yield, selected dies are separated, facets are formed by mechanical cleaving, AR coatings are applied to the facets, and individual PICs are singulated. Figure 77 shows a typical cleaved and AR coated output facet, and Figure 78(a) illustrates the scale of a singulated 8-channel PIC. Individual PICs are then mounted to aluminum nitride (AlN) carriers with electrical traces and wire bonded. The PIC-on-carriers are then soldered and wire bonded to PCBs as shown in Figure 78(b).

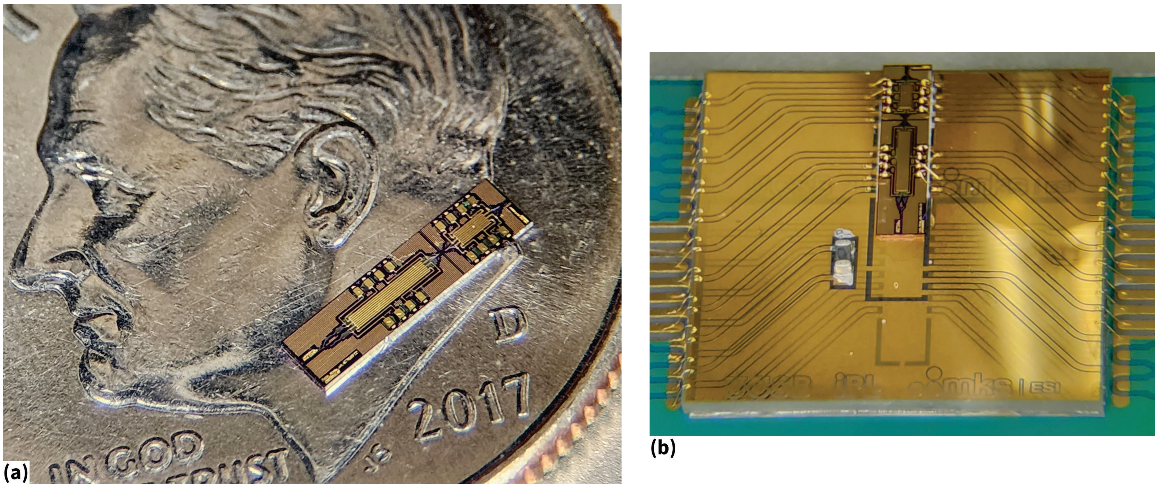

Figure 78: (a) Micrograph of singulated active-passive device on a dime. (b) Micrograph of PIC mounted on carrier on PCB and wire bonded.

5.9 Fabrication Review

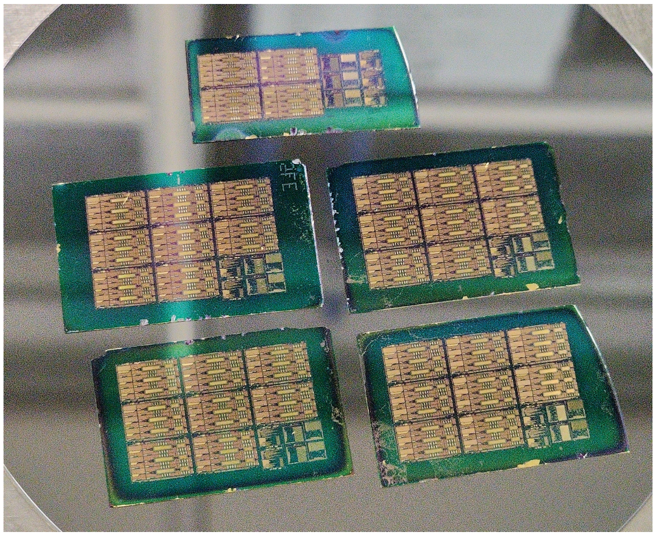

Figure 79: Photograph of successfully fabricated samples.

The active-passive fabrication produced several full samples containing a number of PICs, shown in Figure 79. These were optically inspected, electrically tested, and optically tested to determine electrical functionality, optical insertion loss, and ultimately device yield. One PIC with 8 fully functional electrical and optical channels and one PIC with 8 fully functional electrical and 7 optical channels were packaged and shipped to the OPA testing facility. Due to a processing error, the electrical yield was small enough that no additional fully functional devices were obtained.

5.9.1 VERIFICATION

Initial optical inspection was performed with a digital optical microscope with scanning capability, fully imaging each sample at 200X magnification, as shown in Figure 80. The results were then digitally inspected for waveguide breakage, finding 7 damaged devices out of 108 total devices, for a device-level yield of 94%. During further postprocessing, handling errors resulted in a loss of 9 dies, removing 27 devices for an initial yield of 72% comprising 78 visibly good devices out of 108 fabricated devices.

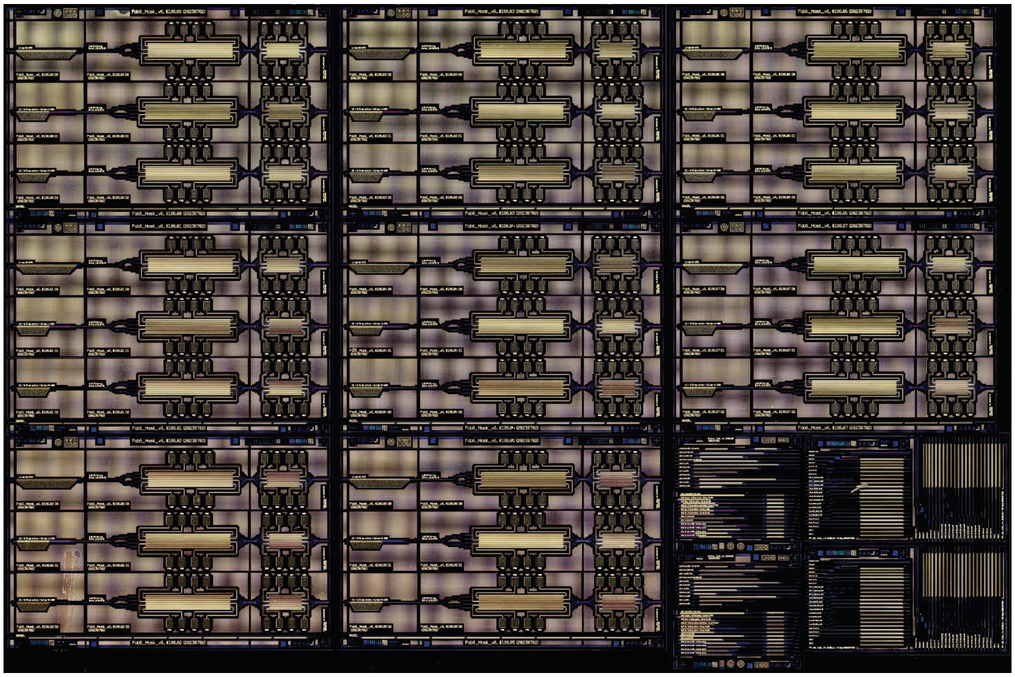

Figure 80: Typical micrograph of processed active-passive sample, showing 8 device dies and 4 test dies.

Further verification was performed in the optical testing laboratory both before and after carrier and PCB assembly. Electrical testing revealed that two full samples of 8 dies each, or 48 devices, were electrically non-functional, reducing yield by 43 percentage points.

Sparse electrical measurement of the diode current-voltage (IV) behavior of the remaining three samples revealed only 10 of 19 tested devices with 100% functional phase modulator and SOA channels, reducing estimated yield to approximately 13%. The nonfunctional devices were a mix of single-shorted-channel devices and high-resistivity channels, and 3 dies of one sample with 5 full dies were all highly resistive.

The precise cause of the low electrical yield is unknown at this time, but further investigation reported in section 5.11 indicates the regrowth composition is unlikely to be the cause. Insufficient removal of the lower layer of the bilayer photoresist in the p-metal liftoff step is a likely cause, but further process testing is required to verify this.

Optical transmission testing of each device was initially performed with an inspection camera viewing the output via a 45° turning mirror while each device's input was coupled to a 1030 nm laser with a 2-μm-MDF lensed fiber. Devices which showed multiple output channels were then optically tested in detail by sequentially measuring the total optical insertion loss of each channel with a lensed fiber on both the input and output, thereby verifying full optical functionality. The total optical insertion loss from the input to a single output channel varied from 24 dB to 30 dB. The 750-μm-long SOAs were not biased for this measurement, and were expected to contribute 2 dB of absorption.

5.9.2 NOTABLE PROCESS STEPS

Several parts of the fabrication process were particularly notable as deserving of extra attention or improvement in future fabrication runs.

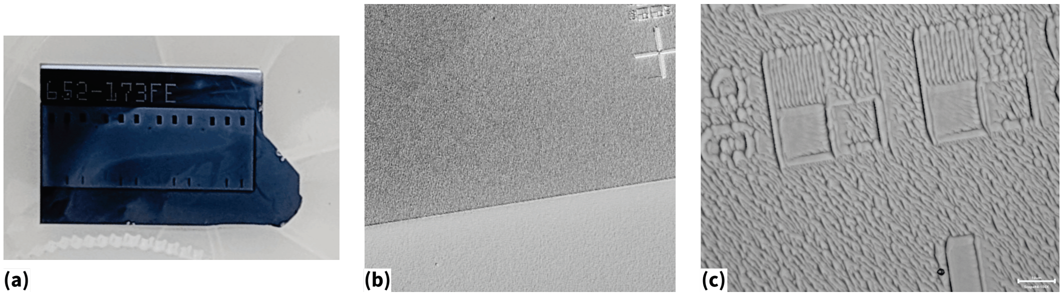

Figure 81: (a) Photograph, (b) 20X micrograph, and (c) 100X micrograph of insufficiently rinsed and dried sample after regrowth. Note the “cloudy” regions in (a) corresponding to surface roughness in (b,c).

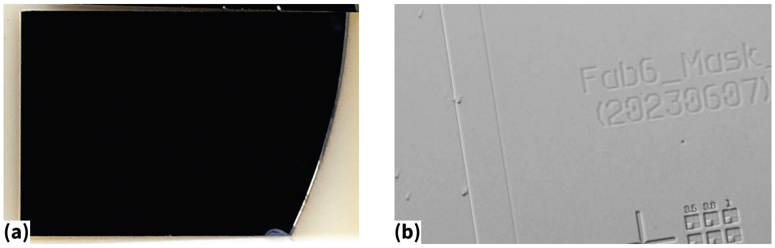

Figure 82: (a) Photograph and (b) 20X micrograph of properly rinsed and dried sample after regrowth. Note lack of cloudy regions in (a) and smooth surface in (b).

Before regrowth, the samples must be well rinsed with deionized water (DI) after the BHF soak. If samples are not sufficiently well rinsed and dried with pressurized nitrogen, water residue may disrupt the regrowth. This can be seen in Figure 81, showing an insufficiently cleaned and dried sample after regrowth with resulting significant surface roughness, while Figure 82 shows a well cleaned sample. The critical dependence of this step was discovered during test regrowths, so the samples in the primary fabrication were sufficiently cleaned and displayed good regrowth quality.

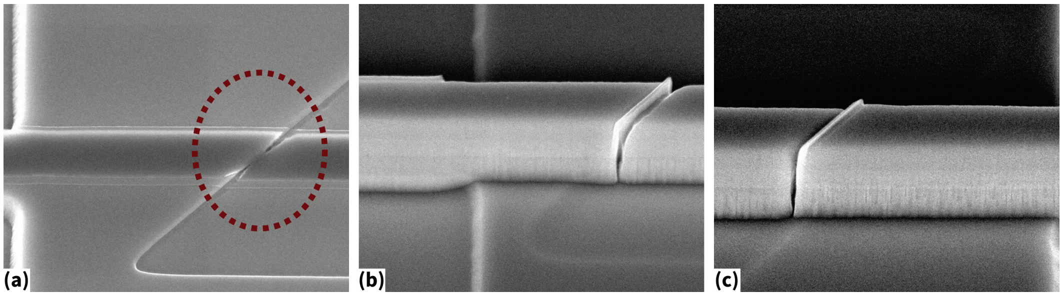

Figure 83: SEM images showing (a) Erosion of deep ridge hard mask after 10 s long BHF soak, indicated area circled and (b,c) resulting waveguides after deep ridge etch.

One potential problem in the fabrication process is that the 10 s long BHF soak after deep ridge hard mask etch produced slight erosions of the hard mask where it transitioned over the 200 nm vertical steps created by the electrical isolation etch, resulting in disruptions to the waveguide after the deep ridge etch as shown in Figure 83. Future fabrications should address this by either moving the electrical isolation step to a later than the deep ridge etch, or by using photoresist instead of hard mask for the deep ridge etch if worse resolution in the deep ridge geometry is acceptable.

The top metal deposition step which also forms the p-metal contacts is a likely source of reduced electrical yield. While not definitively identified, it is possible that insufficiently removed photoresist separated the top metal from the top p-GaAs layer, creating a resistive contact. Overexposure, longer development times, and additional oxygen ion cleaning may be necessary. Deposition of a very thin p-metal layer at an earlier step before the waveguide etches may also eliminate this problem. Care to avoid local overexposure around the p-metal on further lithography steps will then be required.

Overall, no other particular fabrication step was found to produce suboptimal results, except for occasional user error. In particular, the two primary issues identified in the previous OPA PIC fabrications without gain were corrected by (1) using the Panasonic ICP tool for Cl_2/N_2 etching instead of the Oxford ICP tool, and (2) using thicker photoresist and for the top via etch and verifying functionality on test samples before processing the final samples. However, the Panasonic ICP tool did experience noticeable day-to-day etch rate variation, such that some etches were required to be repeated. Future fabrications should verify the etch rate immediately before sample processing.

5.10 Characterization

5.10.1 PROPAGATION LOSS

The total IL of the full 8-channel OPA PICs was measured to determine approximate propagation loss and component EL. The expected IL from a lensed fiber coupled to the input to a lensed fiber coupled to a single output is 22 dB. This is composed of 2.85 dB from lensed fiber coupling at each facet, 1 dB from the MMI splitter tree, 9 dB from the 1/8 splitting, 3.8 dB from propagation, and 2.3 dB from absorption in the unpumped 750-µm-long SOA. The measured IL of the fabricated active-passive OPA PICs was 24-30 dB depending on the specific device.

These insertion losses are moderately higher than the expected values, indicating excess propagation loss in either the passive or active regions, possibly due to the regrowth interface present in the middle of the guiding region, or additional EL from the passive components including the MMIs, bends, and SDTs.

The propagation loss of the epitaxy was characterized directly using the FP waveguide-based measurement technique described in section 3.4.1. A separate die composed of FP waveguide cavities containing assorted numbers and types of components, shown in Figure 84, was fabricated to characterize both the propagation loss and the EL of various components. This includes measurement of the propagation loss of straight waveguides.

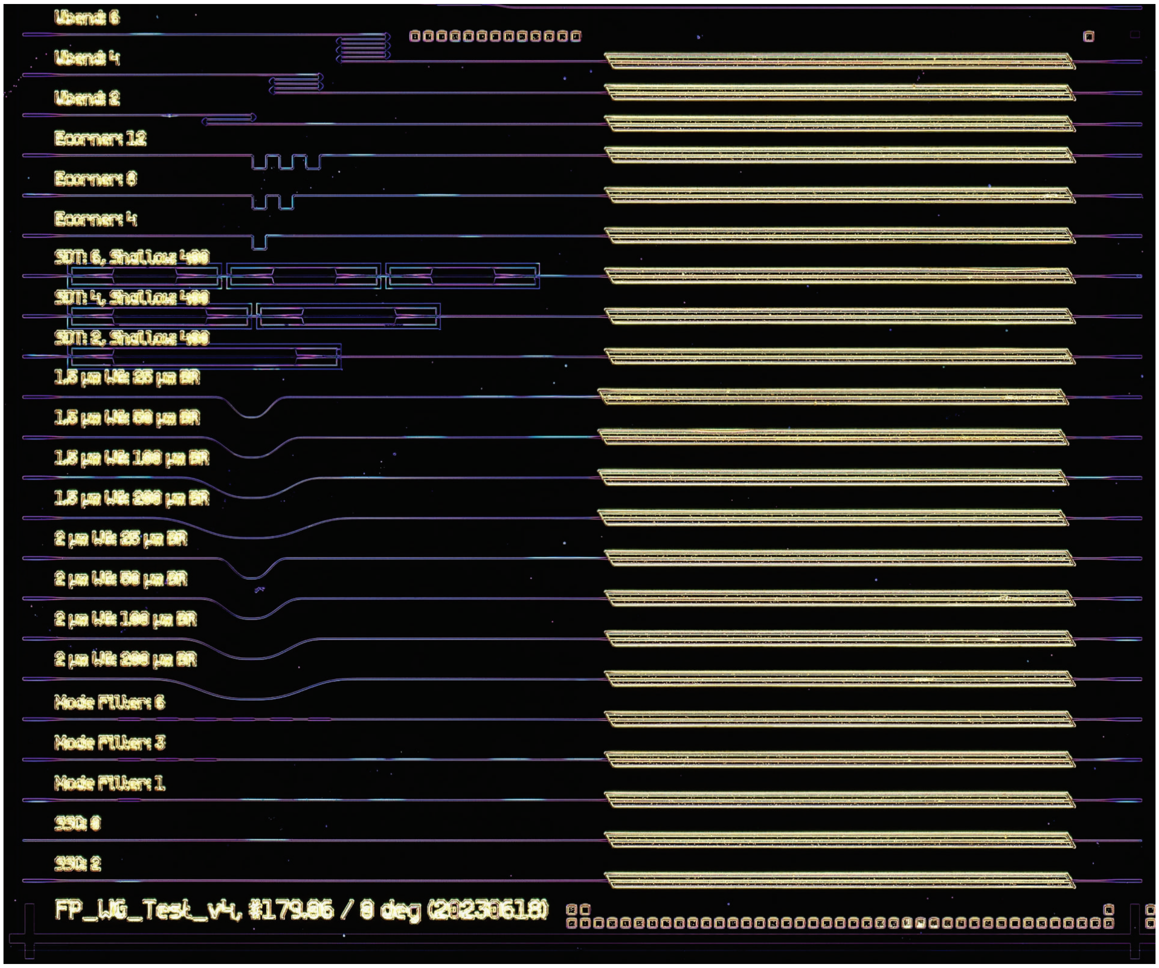

Figure 84: Micrograph of Fabry-Perot waveguide cavity test structures designed to determine insertion loss of various components.

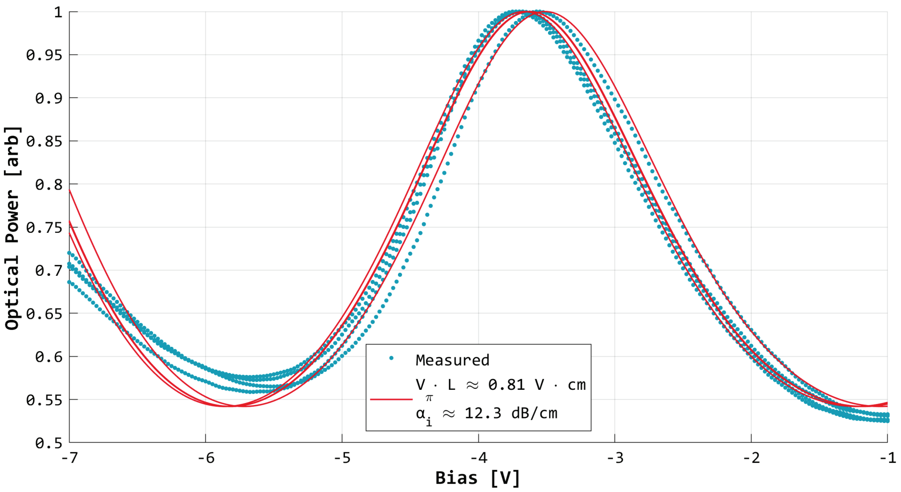

Figure 85: Multiple normalized transmission measurements of Fabry-Perot waveguide cavity with 1-mm-long phase modulator and spot size converter components (dotted blue), and associated simultaneous fit of propagation loss and quadratic phase modulation coefficients (solid red).

Measurements of a straight 0.247-cm-long passive waveguide with a 1-mm-long phase modulator and spot-size converters with cleaved facets on either end indicated 12.3 dB/cm passive loss at 1030 nm. Each spot size converter is expected to have 0.4 dB EL from simulation results, resulting in a total expected 0.8 dB EL within the waveguide, or 3.2 dB/cm apparent excess propagation loss in the FP cavity waveguides. Assuming negligible RAM over the measured bias range of the phase modulator, and no IL for the phase modulator, the propagation loss of the straight waveguide sections is thus ~9 dB/cm. This is in relatively good agreement with the expected value of 6.5 dB/cm at 1030 nm.

Several other components were also characterized with the same technique: the fringe contrast of a FP waveguide with the component was measured, and the contributions from the passive waveguide and spot-size converters were subtracted. These results are displayed in Table 5.

Table 5: Measured component losses from active-passive fabrication.

Component	#	Measured FP EL [dB]	Component EL [dB]	Simulated EL [dB]
Spot-size convertor	2	-	-	0.8
Straight waveguide	0.247 cm	2.2	9 dB/cm	6.5 dB/cm
100 μm S-bend	2	7	2	0.2
SDT	2	12	4.5	0.04
SDT	4	10	1.8	0.04
90° corner	8	12	1.1	0.4
180° U-bend	4	11	2	0.1

All tested components had significantly higher EL than simulated. While this is expected to some extent, the SDTs in particular had excessively high EL. This likely results from the insufficiently anticipated critical alignment tolerance between the shallow rib and deep ridge etch masks for this component. Small misalignments between these two etches can significantly alter the geometry of the SDT. Future designs may ameliorate this with appropriately shaped geometries including gradual transitions.

The 90° corner and 180° U-bend showed better EL than was anticipated, given that the lithographic resolution was insufficient to fully resolve their geometries. Thus, they may be beneficially utilized in future fabrications to reduce the length of the MMI splitter tree.

Using the measured passive waveguide loss and SDT EL, a new estimate of the total OPA PIC IL is ≥27 dB, consisting of 2.85 dB from lensed fiber coupling at each facet, 1 dB from the MMI splitter tree, 9 dB from the 1/8 splitting, 5.3 dB from propagation, ≥4 dB from two SDTs, and 2.3 dB from absorption in the unpumped 750-μm-long SOA. This is in good agreement with the measured 24-30 dB IL of the fabricated and tested devices, indicating that the spot size converter, MMI splitter tree, and SOA absorption ILs are close to estimated values, and that the curved waveguides with 150 μm bend radii have low loss.

5.10.2 PHASE MODULATOR OPTICAL PERFORMANCE

Coarse phase modulation coefficients were determined from the FP cavity measurements performed in the previous section by quadratic fitting of the $\phi(V)$ term in the Airy transmission function, as described in section 3.4.1. The estimated single-sided $V_\pi \cdot L$ modulation efficiency at 1030 nm was 0.81 V·cm. This is somewhat worse than the expected 0.6 V·cm efficiency, indicating a possible discrepancy between the designed and realized epitaxial structure.

However, the FP cavity measurements only use a 1 mm phase modulator with limited modulation depth, and have a large error in the phase modulation measurements. Future work includes more detailed phase modulation measurements at multiple wavelengths by utilizing the MZM test structures that were fabricated at the same time as the OPA PICs.

5.10.3 OPTICAL PHASED ARRAY PERFORMANCE

The OPA performance of this OPA PIC design has not yet been tested. Two OPA PICs have been mounted and sent to the OPA testing facility, and future work includes their evaluation.

5.10.4 ACTIVE DEVICE PERFORMANCE

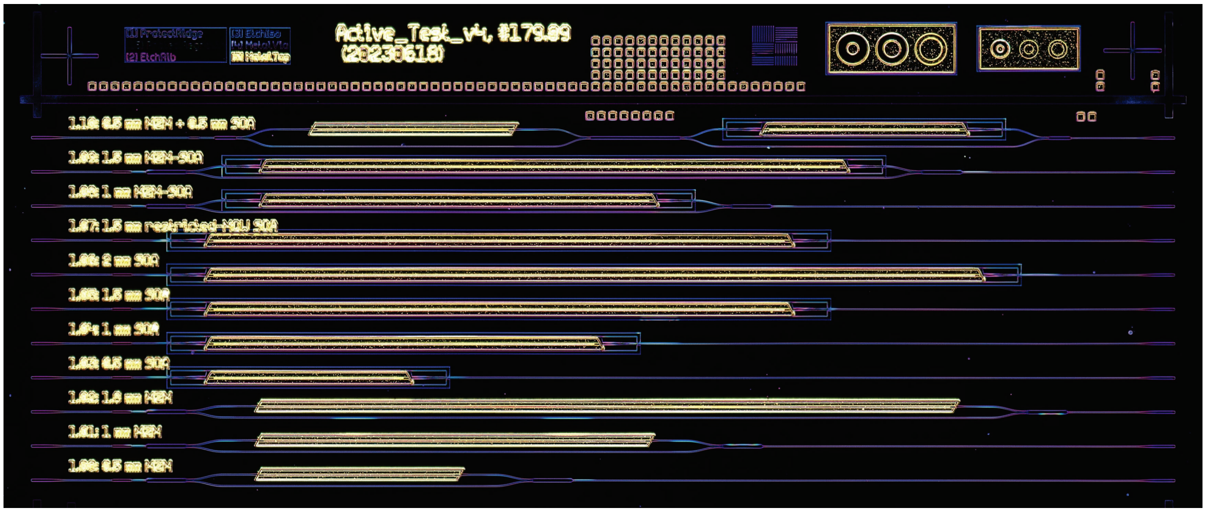

Figure 86: Typical test die with varying lengths of SOAs as well as phase modulators.

SOAs were fabricated as 750-μm-long devices on the 1x8 OPA PICs, as well as in varying lengths on test dies. A typical test die is shown in Figure 86, containing various lengths of SOAs as well as phase modulators in MZM configurations. Both the input and output are AR coated cleaved facets. These SOAs were designed to test the gain as a function of injection current, input power, and SOA length, for comparison to simulated values. Cleaved-facet FP lasers were also fabricated from this same test die by cleaving both sides, reducing the longer SOAs to pure active region FP lasers and the shorter SOAs to active-passive FP lasers as shown in Figure 87. These can then be further cleaved to test varying lengths of FP lasers as discussed in section 3.4.5. Several tests were performed on these various active devices under continuous-wave (CW) current injection, with output powers measured by an integrating sphere and spectra measured by lensed fiber coupling into an optical spectrum analyzer (OSA).

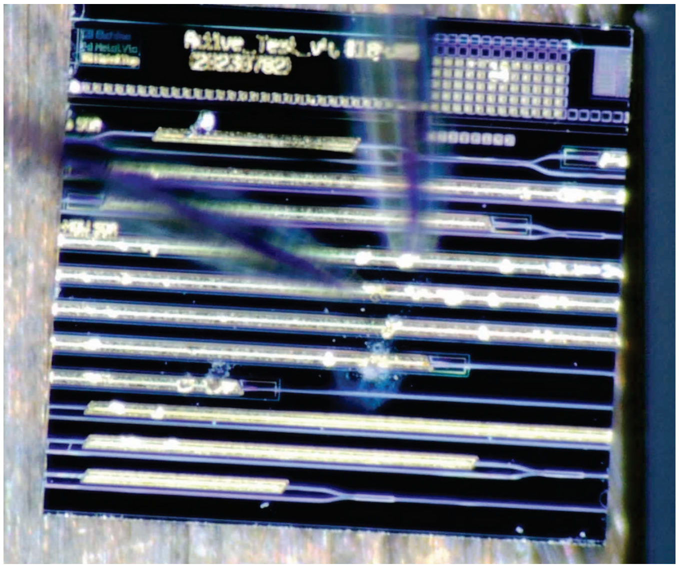

Figure 87: Cleaved facet FP lasers formed by cleaving both sides of the SOA test die.

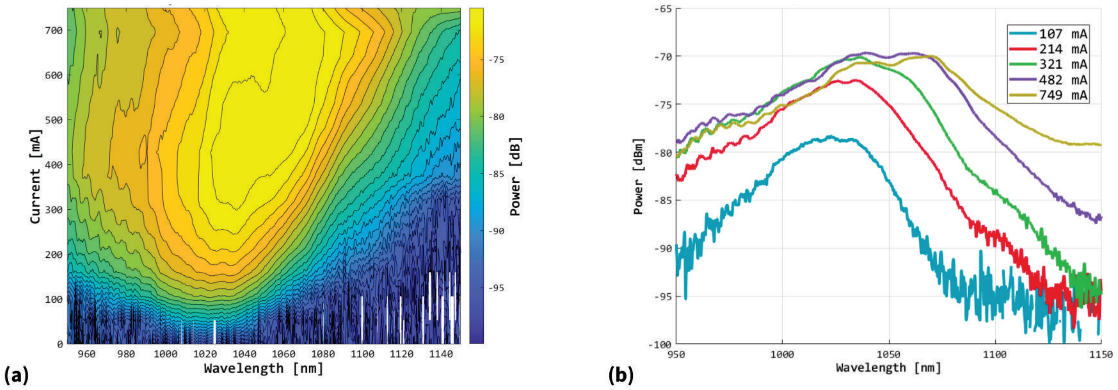

Figure 88: Spectrum of 2000 µm long SOA with AR coated output facets: (a) contour plot at injection currents ranging from 0 to 750 mA, (b) wavelength slices at selected currents.

Firstly, the spectrum of the SOAs was tested to determine the wavelength of the amplified spontaneous emission (ASE), which indicates the gain wavelength. This was measured by fiber coupling the output of one facet into an OSA, and resulted in data well represented by Figure 88, which shows the output of a 2000-µm-long SOA. This spectrum shows a peak near 1020 nm at low currents, which shifts to higher wavelengths under additional current injection. This behavior was expected – the design operational wavelength is 1030 nm, and the MQWs were selected to have a PL peak of 1020 nm as redshift due to thermal self-heating under current injection was anticipated. However, the ASE power is unexpectedly low.

Secondly, LIV measurements of the SOAs with 3 mW of light injected into the waveguide via a lensed fiber were performed. Results were noisy due to changing lensed fiber coupling from self-heating at different currents, but no amplification of the input was detected.

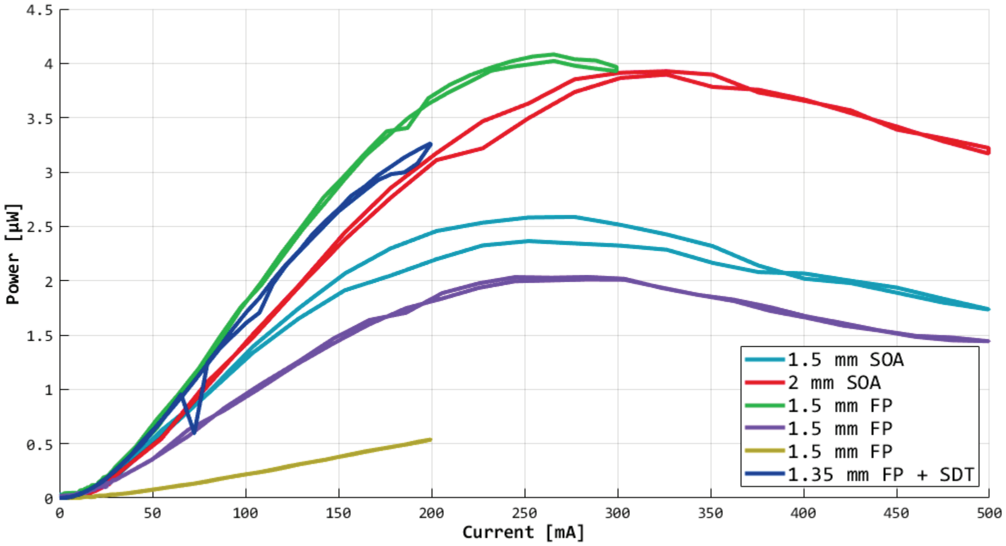

Figure 89: LIV measurements of multiple SOAs and FP cleaved-facet devices of varying lengths. The “FP + SDT” of the last device indicates that it is an active-passive FP laser including a shallow-deep transition and passive length.

Thirdly, LIV measurements of the SOAs and then the cleaved FP waveguides were performed to measure the SOA ASE power and FP laser threshold current and differential quantum efficiency. With a one-sided output measured by an integrating sphere and the power doubled to account for both facets, the results of these measurements are shown in Figure 89, with a maximum output power of only 4 μW from any device.

Unfortunately, no lasing was observed from the FP laser devices. The output spectrum of these devices showed only ASE at the expected wavelengths, as seen in Figure 90, with no lasing. The spectrum and behavior are similar to the SOAs. The overall power is weaker due to poorer coupling to the lensed fiber, as the FP laser devices have a shallow rib waveguide with a larger mode than the passive deep ridge waveguide outputs of the SOAs.

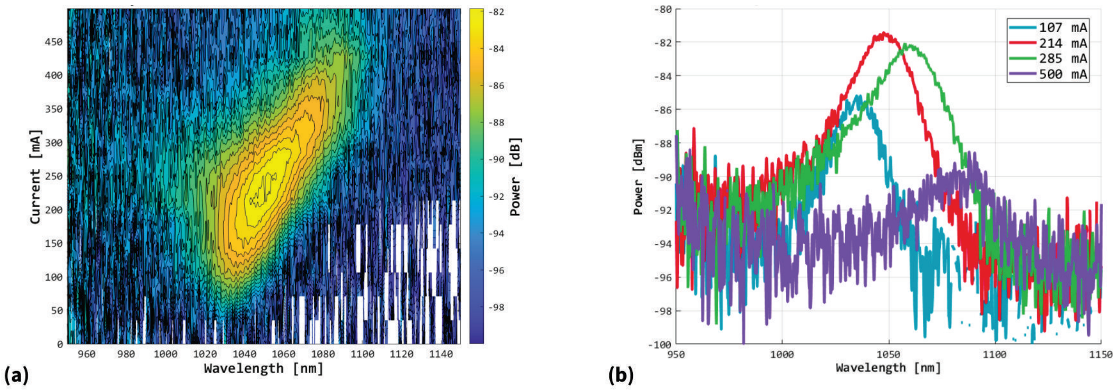

Figure 90: Spectrum of 1500 µm long FP device with cleaved facets: (a) contour plot at injection currents ranging from 0 to 500 mA, (b) wavelength slices at selected currents.

Testing of the 9th-order laser devices indicated they merely functioned as long SOAs.

These results indicate that the material gain is extremely poor, the internal loss of the active regions is extremely high, or both. Insertion loss testing of the full OPA PIC devices restricted active region excess loss to under 3 dB/cm, which is not high enough to produce the observed effects. Further testing of fully fabricated active device performance was suspended in order to conduct a more detailed investigation of the MQW regions and attempt to identify the reasons for the extremely low gain.

5.11 Investigation of Gain

The results of active device characterization indicate very poor gain performance. Broadly, the poor performance may be caused by a material problem, or by a fabrication error. To determine which of these is the case and elucidate the exact cause in more detail, further investigation into the material properties of the active devices was conducted.

5.11.1 PHOTOLUMINESCENCE

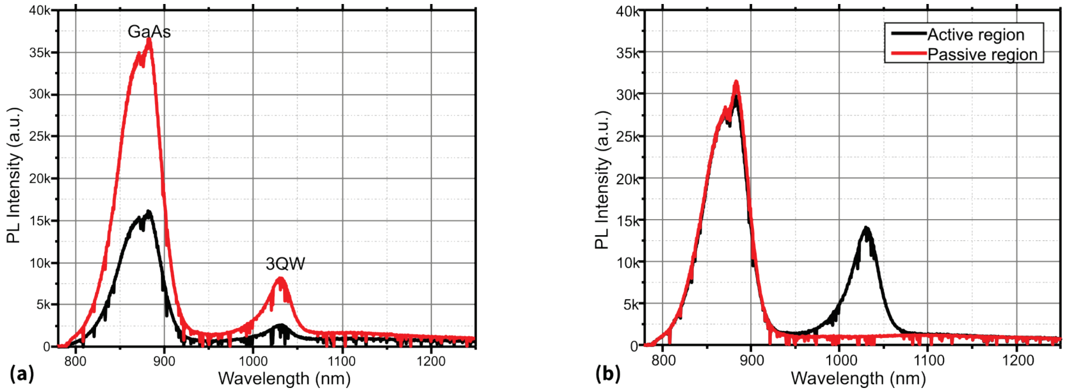

Figure 91: PL spectrum of (a) the epitaxy prior to regrowth at two different PL intensities, indicating poor QW emission, and (b) the epitaxy after selective removal of quantum wells in passive regions, indicating good active-passive definition.

PL measurements optically pump the tested material at a short wavelength and observe the resulting optical emission, producing a spectrum related to the inherent material gain. PL measurements were performed by colleague Bei Shi on both the as-received epitaxy prior to regrowth, and the epitaxy after selective removal of MQW regions. The results are shown in Figure 91. The active regions in both cases have 10 nm of GaAs on top, but the MQW emission peak is only 1/2 or less the intensity of the GaAs emission peak. This is unexpectedly poor MQW behavior. In comparison, a very similar epitaxy in [70] showed a MQW PL peak greater than the GaAs peak, as would be expected for performant MQWs. This result indicates that the active layer of the epitaxy may be defective or damaged, and is likely the cause of the poor active device performance.

The comparison of PL results between active and passive regions, however, indicates that the active-passive processing performed as expected. The MQWs are clearly removed from passive regions and unaltered in active regions, demonstrating that the active-passive process developed here is a successful design.

5.11.2 X-RAY DIFFRACTION

X-ray diffraction (XRD) measures the spectrum of x-rays diffracting through the semiconductor crystal lattice of the target material. This spectrum depends on the exact composition of the material, so measured spectra can be compared to simulated spectra to determine the composition of the target. Several measurements were taken by Bei Shi.

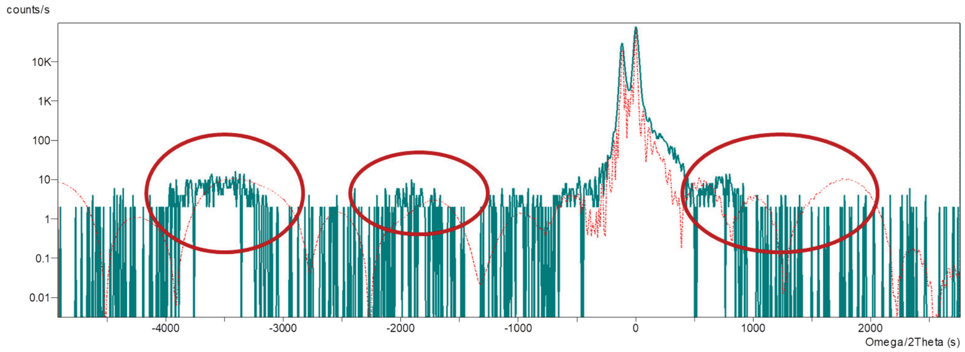

Figure 92: XRD spectrum of the epitaxy prior to regrowth, with differences between the expected (dotted red) and measured (solid teal) spectra circled in dark red.

XRD measurement of the initial epitaxy prior to regrowth, and shown in Figure 92, grossly matched the expected main peaks from the GaAs and AlGaAs layers, but did not match the smaller side peaks. This is interpreted as potential structural defects in the MQWs.

XRD measurement of the regrown epitaxy, shown in Figure 93, indicated that the regrown layers are correct except for one difference: the top AlGaAs layer composition is in actuality only 25% aluminum instead of the desired 30%. Subsequent optical simulation of the as-grown structure indicated no change to the expected propagation loss, but the expected single-sided $V_\pi \cdot L$ modulation efficiency with an $Al_{25}GaAs$ top cladding is 0.7 V·cm at 1030 nm instead of 0.6 V·cm, due to reduced confinement of the optical mode. This brings the expected modulation efficiency closer to the measured value of 0.8 V·cm.

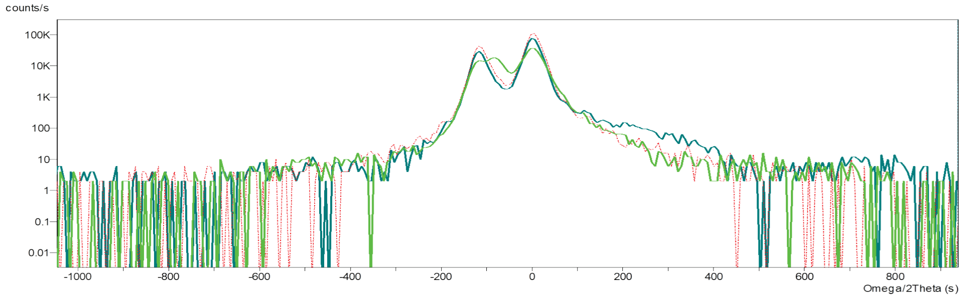

Figure 93: XRD spectrum of the epitaxy before (teal) and after (green) regrowth. The post-regrowth peak was expected to have the same secondary peak as pre-regrowth, corresponding to the $Al_{30}GaAs$ upper and lower cladding, but instead shows a split peak, indicating the $Al_{30}GaAs$ lower cladding and $Al_{25}GaAs$ regrown cladding.

5.11.3 SECONDARY ION MASS SPECTROMETRY

Secondary ion mass spectrometry (SIMS) measurements are able to determine the elemental composition of the epitaxy as a function of depth by ablating the material with a cesium ion beam and performing mass spectrometry of the ejected elemental ions. This can be used to measure the epitaxial composition and doping as a function of depth, which thus provides measurements of layer thickness.

A SIMS measurement of the regrown top cladding, shown in Figure 94, indicated that all the layers were grown as expected, with the exception of the doping of the $Al_{25}GaAs$ top cladding being only 5e16 cm^{-3} instead of 2e17 cm^{-3}. This is expected to change the conductivity of this layer by a factor of 2-3. More precise electrical measurements of the active devices would be required to resolve this difference, so it is not a factor in the current results. The high O concentration just above the MQW layer, discerned by the slight indium content, indicates that there was some oxidation of the epitaxy prior to regrowth, possibly leading to additional propagation loss at the regrowth interface. Unexpected Si content in the regrown layers indicates that the MOCVD reactor may have been slightly contaminated, so future regrowths should more fully clean the reactor prior to regrowth. The low concentration, however, is unlikely to cause significant additional propagation loss.

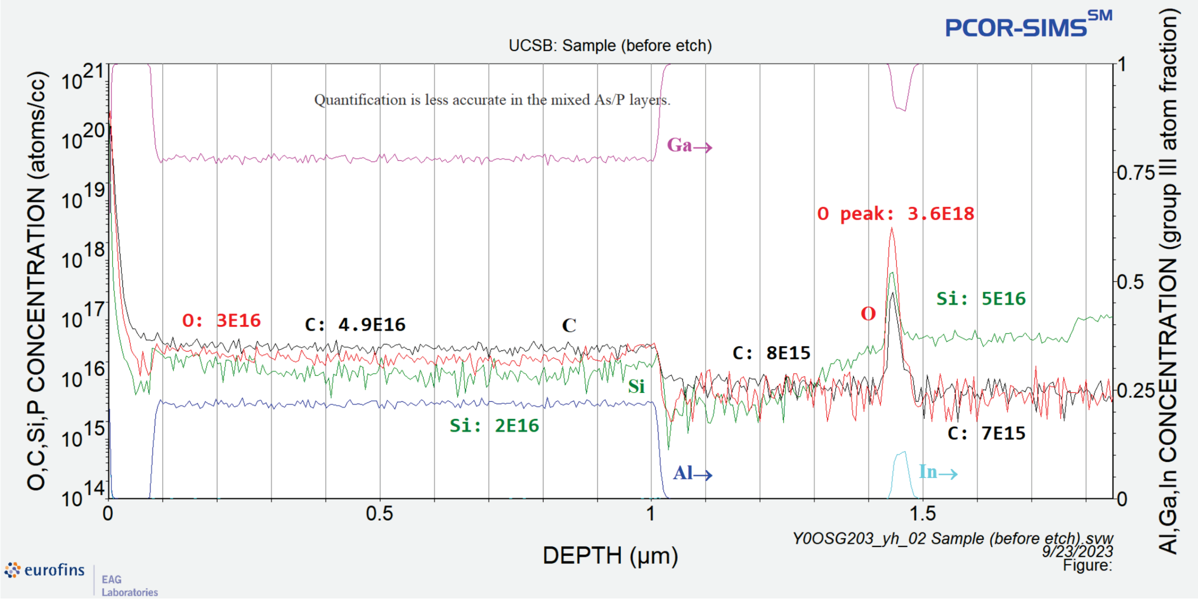

Figure 94: SIMS measurement of the regrown epitaxy.

Additional characterization of the MQW region by a more precise SIMS measurement of the top 100 nm of the unprocessed epitaxy is in progress, and is hoped to shed additional light on the MQW layer thickness and potential defects.

5.11.4 CONCLUSION OF GAIN INVESTIGATION

Investigation of the material properties of the active layer was conducted via PL and XRD analyses. The results of these support the conclusion that the MQW layers of the original epitaxy are significantly underperforming, possibly due to structural defects. Further investigation of the MQW layers is in progress, including a high resolution SIMS analysis focused on the MQW layer structure and consultation with the epitaxial vendor to determine if the MQW performance was abnormal during or after growth, and elicit a comparison to similar structures they have previously fabricated.

SIMS and XRD analysis of the regrown epitaxy showed it was as designed, except for slightly less aluminum content in the upper cladding and somewhat lower doping.

5.12 Chapter Summary

An active-passive process and associated epitaxy was developed, optimized for both efficient phase modulators and active regions capable of providing per-channel gain. The active-passive process was successfully demonstrated, with several 8-channel OPA PIC devices produced, as well as phase modulator test PICs. Individual 1-mm-long phase modulators tested at 1030 nm exhibited single-sided $V_\pi \cdot L$ modulation efficiency of approximately 0.8 V·cm, in approximate agreement with the predicted 0.7 V·cm value.

However, the performance of the active regions did not match predictions, producing no detectable gain and very low power ASE emission under current injection. The poor performance observed during the characterization of active devices prompted a deeper investigation into the cause of the reduced gain. Based on PL and XRD measurements, the likely cause is defective MQWs in the original epitaxy prior to processing. Investigation is ongoing to determine the origin of the defects and produce replacement epitaxy.

The successful production of passive and phase modulating devices in the non-active regions validated the active-passive design and fabrication process. This demonstrates the feasibility of a monolithic GaAs OPA PIC platform with an on-chip laser, full phase control, and per-channel gain, requiring only functional MQWs to achieve this goal.

Chapter 6

Future Work

Future iterations of the active-passive GaAs OPA PIC platform presented in Chapter 5 will build on the prior design methods and results, but will undoubtedly include additional design and process refinements as well as novel advances. Several items have already been identified during the work leading to both previous results that may be useful for future development. Additional notes regarding potential complications in extending the existing design and fabrication process are also included in this chapter.

6.1 Epitaxy

Primarily, the active-passive platform from Chapter 5 must be re-fabricated with new epitaxy that has a functional active region, in order to fully demonstrate the feasibility of this approach. The MQWs may need to be redesigned, or the epitaxial growth may simply need to be improved. Additional testing is required to determine which of these is the case.

Other epitaxial designs may also be considered for future work. As briefly discussed in section 5.4, an alternative to a blanket-regrowth design was considered during the active-passive design's development phase. This consisted of a dual-layer design with two vertically separated waveguides, one containing gain and the other performing passive and phase modulation functions. This was not developed to a fully usable state, but the possibility of good performance was demonstrated in simulation. The transition between upper and lower waveguides was incompletely modeled, but other similar designs in literature utilize higher aluminum content in the lower waveguides to produce an overall higher index [157], [159], [170], enabling easier transition from lower to upper waveguides.

6.2 Component Design

Several components could benefit from improved designs, especially if higher resolution lithography is used in future fabrications, such as with a deep-UV (DUV) lithographic tool.

Smaller waveguides are potentially an important development, providing smaller bend radii and thus a smaller device footprint, enhancing single-mode operation, and enabling smaller MMIs to further reduce the footprint. These may be possible with the improved resolution and alignment tolerance available from a DUV stepper, but will also require process improvements for reliably vertical and smoother sidewalls. Improved resolution may also enable reliably fabricable high-order grating lasers.

6.2.1 VERTICAL OUT-COUPLING

New components will likely be desired for future device designs, one possible component being vertical out-coupling structures. Initial investigations into two types of vertical out-couplers have already been performed: total internal reflection (TIR) mirrors and vertical grating couplers (VGCs). For both of these, the out-coupling direction can either be towards the immediate surface or through the substrate. The latter possibility will require additional polishing if thinned substrates are required, but may also facilitate avoiding any substrate thinning. If all coupling is via substrate-emission vertical couplers, double-side-polished wafers may be used with no thinning, and dies can be separated via dicing instead of cleaving. Epi-side N contacts would then be required.

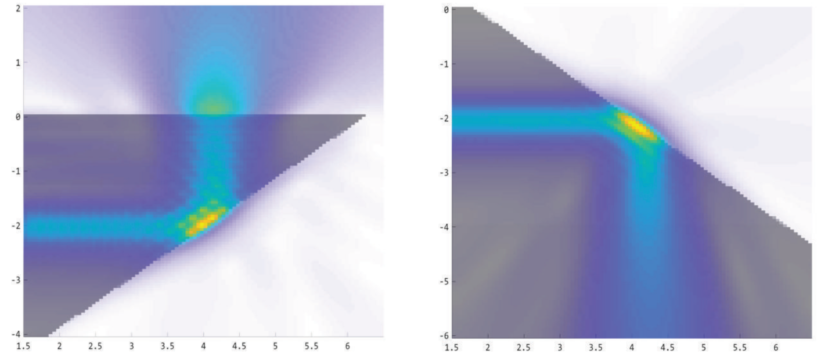

(a) **(b)**

Figure 95: Simulated TIR mirror reflecting the mode (a) upwards, and (b) downwards.

TIR mirrors are compact and easily fabricated vertical coupling devices. Simulations, as in Figure 95, show the optical mode cleanly redirected upwards or downwards depending on the TIR mirror angle with very little loss. Fabrication is straightforward using a 45-degree chemically assisted ion beam etch (CAIBE) tool, but the exact etch recipe and achievable etch quality remains to be developed. This process development is the primary task required to achieve TIR mirror fabrication. In-house AR coating can easily be applied to the emission surface via PECVD surface films. The drawback of TIR mirrors is that they are unable to easily engineer the size of the out-coupled mode.

VGCs are a well-known solution to out-coupling, and are widely used in silicon photonics [171]– [174]. Several examples have been shown in GaAs-based epitaxies [175], [176], but their use is not common in III-V materials due to the difficulty of achieving high vertical optical index contrasts. Advantages are control of the exact output size over a very wide, and even the possibility of focusing, but disadvantages are low out-coupling efficiency, with standard designs typically exhibiting 3 dB excess loss. Back-side emission may be able to help reduce excess loss with such strategies as thin-film DBRs or metal mirrors on the top of the epitaxy to break the vertical symmetry of the grating structure. The design of these components in the active-passive epitaxy has been investigated, but not to any great extent. Design difficulty would be significantly eased for processes using DUV lithography rather than the current i-line lithography processes, as VGC features are frequently significantly smaller than 0.5 μm.

6.2.2 PERFORMANCE LIMITATIONS

Ultimately, component excess loss (EL) is limited by fabrication variations and imperfections. Designs can readily achieve simulated <0.1 dB EL with only moderate optimization. Ideal designs will consider likely fabrication variation and may opt for higher nominal EL in exchange for more robust fabrication tolerance. Results from fabrication tests should also inform the development or optimization of existing and new components.

6.3 Fabrication

Several of the current fabrication processes are known to be imperfect, and would benefit from additional development. Certain improvements may also enable new capabilities or improved performance.

6.3.1 PROCESS DEVELOPMENT

One difficulty in the active-passive process stems from the hard mask that is deposited after the shallow rib etch. This hard mask is necessary for the high-resolution deep ridge etch. Because the shallow rib etch presents near-vertical sidewalls with moderate depth, however, there exist regions of hard mask with a very thick vertical extent (1.2-1.4 µm) on these sidewalls, such as around the shallow-deep conversion components. The hard mask dry etch is highly directional, so even when these regions are lithographically exposed, the hard mask is not fully removed. Removing these regions is the purpose of the 10 s long BHF dip following the deep ridge hard mask etch, but other problems can result from the undercut that also occurs in the regions of desired hard mask. One instance of this is occasional undesired removal of the hard mask around the 200-nm vertical steps when the waveguide crosses the isolation etch border, as mentioned in section 5.9.2 and shown in Figure 83. Three potential solutions to this are: (1) using thick photoresist for the deep ridge etch mask instead of hard mask, which would require accepting low resolution (≥1.2 µm) for the deep ridge layer, (2) applying a bias to the mask features where the vertically-coated sidewalls will be present, thereby incorporating the sidewall masking into the design, and (3) performing the isolation etch after the deep ridge etch to avoid the area known to develop problems from the 10 s long BHF soak. These solutions should be carefully considered with all implications thoroughly explored before further process development.

The various dry etches are another area in need of additional process development, as they have shown either week-to-week variation in etch rate and quality on the Panasonic

ICP #1, or location and exposed III-V area dependence on the Oxford ICP. If either of these issues were solved, the process reliability would be significantly improved.

6.3.2 IMPROVED PROCESSING

Further improvements beyond what the current process requires may enable new capabilities. In particular, smoother sidewall etches and higher resolution lithography may be combined to significantly reduce the minimum bend radius of the passive waveguides. The achievable aspect ratio of the deep ridge etches would also need to be verified for narrower waveguides.

If dry etching improvements are unable to produce sufficiently smooth sidewalls for narrower waveguides and tighter bend radii, other methods may be necessary. One possibility is thermal oxidation of the AlGaAs and GaAs layers to produce ultra-smooth effective sidewalls with very low loss [177]– [181].

6.4 Yield Improvement

From previous fabrication experience, yield can be expected to depend on a number of difficult to estimate factors, detailed below. Overall yield of the two previous designs was in the 15-20% range for full devices. Any fabrications using full 4” wafers should achieve significantly higher yield since many of these previously experienced problems are relevant specifically to small samples and the associated handling, or imperfect processes that were insufficiently tested before fabrication.

6.4.1 PRIMARY CONTRIBUTORS

The largest reduction in yield during past fabrications has been sample breakage from handling in the last few stages of processing or packaging. The first design without gain experienced a 28 percentage point yield decrease from sample breakage, and another 35 percentage points were assigned to general sample handling and contamination. With improved handling practices, the active-passive design had only a 6 percentage point yield reduction from lithographic errors and handling during processing, but subsequent breakage during packaging resulted in a further 25 percentage point reduction. Full 4” wafer processing should have even higher yield from handling due to easier sample movement, generally less required handling, and more uniform processing.

For both fabrications, there was no loss from AR coating, but optical testing found ~36% of micrographically verified waveguides to have poor optical transmission. The optically poor waveguides are likely caused by unseen contamination during processing, and 4” wafer processing would allow for improved cleaning and handling procedures compared to small samples.

The largest contributor to poor yield in the active-passive design was high electrical resistivity in two samples. Determination of the cause of this requires further investigation, but is likely related to the p-metal deposition step. While not definitively identified, it is possible that insufficiently removed photoresist separated the top metal from the top p-GaAs layer, thus forming a resistive contact. Overexposure, longer development times, and additional oxygen ion cleaning may be necessary. Deposition of a very thin p-metal layer at an earlier step, before the waveguide etches, may also eliminate this problem. Care to avoid local overexposure around the p-metal on further lithography steps will then be required.

6.4.2 EXPECTED FUTURE YIELD

Any fabrications on full 4” wafers should have high yield. Pessimistically assuming similar handling and contamination related errors as in the active-passive design (94% visual yield) and optical (64%) and electrical (75%) yield similar to the design without gain, the expected minimum yield of a 4” fabrication is ~50% for similarly sized devices. Optical and electrical failures will overlap, so the yield will be somewhat higher than a straightforward multiplication of electrical and optical test results.

Note that full-device yield will vary depending on device size. At this time, no clear estimate is available for how yield scales with device size. The yield reduction from handling errors is a mixture of device-scale, with large scratches eliminating entire devices, and area-scale, from contamination. The improved handling evinced in the active-passive fabrication has solved the majority of area-scale contamination, and the handling as discussed should not be present for 4” devices. The optical and electrical reductions are of uncertain and likely varying causes.

Assuming the ~50% yield is entirely area dependent and given for an 8 mm^2 device, a hypothetical 512-channel device is likely untenable if 100% functionality is absolutely required, but a hypothetical 16-channel flip-chip device may have >75% yield. However, these naïve assumptions should be checked by actual particle count measurements during future test fabrications. The acceptability of partial functionality should also be assessed for high-channel-count devices if scaling channel count is desired.

6.5 Packaging

Current packaging is fairly basic, consisting simply of soldering the PIC to an AlN carrier which is then soldered to a PCB. All components in this stack are then manually wire bonded together. This type of packaging may scale to a few hundred channels with commercial automated wire bonding, but is likely to be more expensive and less scalable than flip-chip bonding.

Flip-chip bonding is an alternative packaging method that mounts the PIC with the epitaxial side downwards by soldering pads or waveguides directly to a carrier or PCB. The method is in common use for some applications. However, the PIC and process need to be specially designed to accommodate this. Additionally, a flip-chip-bonded PIC no longer has visible waveguides, so alignment of external inputs may be difficult. Ideally on-chip lasers and back-side vertical couplers would be used.

6.6 Scaling Limitations

Several different considerations limit scaling to higher channel counts, beyond the potential yield issues discussed in section 6.4. These include routing and lithography limitations at the die design level, and thermal and optical power limitations at the waveguide functionality level.

6.6.1 ROUTING

The current packaging is the primary limitation to channel scaling, as every channel must be routed out to a wire bond pad. This routing either involves a more complex fabrication process as in the design without gain which utilized two metal lift-off steps to achieve routing over the top of neighboring phase modulators, or an end-routing connection as in the active-passive design that requires significant additional longitudinal space as more channels are added. In both cases the wire bond pads also occupy 150 µm of longitudinal space per channel. Channel scaling is not easily possible beyond 64 channels with the longitudinal method, or 128 channels with the crossover-routing method.

These channel scaling limitations are significantly relieved with flip-chip bonding, as all electrical routing can be accomplished on the carrier instead of the PIC, with associated relaxation of space restrictions and resolution tolerances. With the carrier providing most of the electrical conductivity, the channel pitch can also be significantly reduced as there is no need for large metal pads on the devices. At this point, other considerations become the limiting factors.

6.6.2 LITHOGRAPHY

Besides the space required to route the wire bond pads, other factors impact the maximum channel count achievable on a single mask design. These are primarily the maximum usable die size and the channel pitch. Bend radius may also be an important consideration for very large channel counts as this determines the length of the MMI splitter section; this may be improved with narrower waveguides and smoother sidewall etches.

Without flip-chip bonding, the minimum phase modulator pitch is approximately 30 µm to allow sufficient room for top metal. With flip-chip bonding, this could be reduced to 10-15 µm pitch, or possibly less.

The minimum SOA pitch using the current active-passive epitaxy and cross-section designs is roughly 35 µm in order to avoid optical coupling between neighboring devices in the shallow rib regions. Deep ridge or double-ridge waveguide designs may be possible for SOAs, although expected performance remains to be investigated and sidewall carrier recombination may be an important factor. With deep ridge SOAs, the minimum pitch would be the same as the phase modulators.

The lithographic tools in the UCSB NanoFab utilized for this work constrained the maximum die size. The GCA Autostep 200 i-line stepper has a maximum 14 mm x 14 mm reticle size, but away from the center the resolution degrades moderately. The ASML DUV stepper has a 21 mm x 21 mm reticle limit, and field stitching has been demonstrated on that tool. Note that only waveguide features need to fit within the reticle limits; non-waveguide features such as metal pads can be imaged on the MLA150 maskless aligner.

Assuming an SOA design similar to the one used in the active-passive design, and flip-chip bonding to eliminate the need for additional top routing, there is a maximum channel count of 400 on the GCA Autostep 200 tool when filling the 14 mm x 14 mm reticle size. Using the ASML DUV tool, there is a maximum channel count of 600 without field stitching. With deep ridge SOAs and flip-chip mounting, 1400-2100 channels may be possible in the 21 mm ASML reticle without field stitching.

6.6.3 THERMAL

With active devices present in the active-passive design and future designs, thermal restrictions become important. SOAs and lasers produce significant heat, and sufficiently dissipating this heat is the primary restriction on active region gain and SOA density. As the active-passive design is back-side-mounted, it relies on thermal conduction through the substrate and into the carrier. The density of SOAs thus cannot be very high, or significant thermal crosstalk will be present. The thermal conductivity of the AlN carrier is ~3x larger than the GaAs substate, so the substrate thickness is the primary limiter. A flip-chip-bonded device would also have a significantly shorter thermal path to the AlN carrier, and could therefore support both closer and higher power SOAs.

As a crude estimate, a 20 mm x 20 mm device with 1500 channels and 5 mW of optical power per channel would output 7.5 W of optical power, and possibly 75 W of thermal power dissipation if assuming poor (10%) electro-optical efficiency. This produces a heat load of ~20 W/cm^2, which is well within the capability of typical cooling solutions. The expected junction temperature has not been estimated at this point, but advanced commercial cooling solutions can readily handle 100 W/cm^2 with <15° C increase [182].

The composition of the epitaxy also plays a role, as some III-V materials have significantly lower thermal conductivity than others. A common III-V cladding material, InGaP, has thermal conductivity ~11 times lower than GaAs, so should be avoided in the primary thermal dissipation path.

6.6.4 OPTICAL POWER

Beyond the thermal restrictions on gain density, a potential limitation on optical power is two-photon absorption (TPA), a process that occurs at high optical intensity within a material when two photons are simultaneously absorbed to promote an electron to the conduction band [183]. The TPA loss α_{TPA} is given by:

$$\alpha_{\text{TPA}} = \beta_2\, I/2 = \beta_2\, P/(2\, A) \tag{6.1}$$

Where β_2 is the TPA coefficient, I is the optical intensity, P is the optical power, and A is the effective mode area. Typical values of β_2 for GaAs are 0.03 cm/MW at 860 nm, 0.02 cm/MW at 1060 nm, and 0.001 cm/MW at 1500 nm [87], [184]– [187].

At a fixed wavelength, the TPA strength depends primarily on the effective mode area. The threshold power for a given α_{TPA} is:

$$P_{\text{threshold}} = 2\, \alpha_{\text{TPA}}\, A/\beta_2 \tag{6.2}$$

A commonly used TPA threshold is $\alpha = 0.05\ \text{cm}^{-1} \approx 0.2$ dB/cm, giving an expected threshold power of:

$$\frac{P_{0.2\ \text{dB}}}{A} \approx \frac{2\cdot 0.05\ \text{cm}^{-1}}{0.02\ \text{cm/MW}} = 50\ \text{mW}/\mu\text{m}^2 \tag{6.3}$$

Given the OPA PIC's architecture only requires a very short length of high power after the SOA section, however, a more reasonable threshold may be 3 dB/cm, or $0.7\mathrm{cm}^{-1}$:

$$\frac{P_{3\,\mathrm{dB}}}{A} \approx \frac{2\cdot 0.7\ \mathrm{cm}^{-1}}{0.02\ \mathrm{cm/MW}} = 700\ \mathrm{mW/\mu m^2} \tag{6.4}$$

The effective mode area for the 2-μm-wide deep ridge passive waveguides is 1.24 μm^2, which corresponds to 860 mW optical power per waveguide. For shallow rib waveguides, this increases significantly to approximately 4 W per waveguide. If TPA proves to be an important limiting factor in future designs, slightly increasing the aluminum content in the waveguide core can significantly reduce β_2 [188].

6.7 Two-Dimensional Beam Steering

Many applications require two-dimensional beam steering. OPA PICs can provide this by two methods: (1) combining a 1D OPA with a grating output coupler and relying on the wavelength-dependent grating output angle, or (2) using a 2D grid of output apertures to create a full 2D OPA. Both techniques have previously been demonstrated. Other methods also exist [189], [190], but can be considered variations on these techniques.

Wavelength-dependent output gratings are the most common solution for 2D steering used by demonstrated OPA PICs, especially SiPh-based devices [44]– [48]. This method takes advantage of the wavelength dependency of grating couplers such that a single tunable laser can entirely control one dimension, while the other dimension is a typical OPA. The major benefit of this method is high packing density and efficient scaling – with only one direction to extend the array, emitters can be closely spaced while still providing 2D steering. However, applications must accept an operating wavelength that varies with steering angle. The maximum steering speed is also limited by the tuning speed of the source laser, and even with high-speed tuning sections, the photon lifetime will limit tunable lasers to low-GHz-range speeds.

Full 2D OPA PICs have also been demonstrated [41], [191]– [194]. These are implemented in the same way as 1D OPA PICs, but the outputs must be vertical and tiled to form a 2D aperture. They offer unmatched steering speed that is only limited by phase modulation bandwidth, and can also enable novel beamforming or multi-beam techniques [195]– [197], as a 2D OPA provides an arbitrarily controllable wavefront. Since no wavelength tuning is required, these are also suitable for high-speed coherent lasercom [198] or other applications requiring a stable wavelength. The difficulty, however, is in the layout and routing of the output apertures and waveguides. Dense apertures are desired to minimize sidelobe power and increase steering range, but space must be left to route waveguides to each aperture. This is the primary limitation of these systems, and why they are not as frequently utilized as the phase-and-wavelength type of 2D OPA PICs.

6.7.1 SPARSE 2D ARRAYS

The routing difficulties of 2D OPA PICs can be ameliorated by removing some of the emitting apertures. This is known as a sparse array, and sparse OPAs have been demonstrated [148], [199]– [201]. The tradeoff is reduced far-field power, especially in the main beam, and often increased sidelobe levels. With proper engineering of the removed elements, though, the sidelobe levels can even be improved above the performance of a uniform 2D array [146]. Power in the main beam, however, is always sacrificed. This is a particularly poor tradeoff for passive SiPh systems where all output power must be coupled in through a single input with a limited optical power handling capacity.

For active-passive systems with on-chip gain, this tradeoff is not as severe. The output power can be significantly higher than the input power, as each channel will provide its own amplification. Dense active-passive OPA PICs with many channels are likely to be thermally limited, as previously discussed in section 6.6.3. Therefore, the total output power of the OPA PIC will likely be the same regardless of whether it is a full or sparse 2D array, as sparse arrays will be able to support a higher power per channel.

To demonstrate the tradeoffs of this total-power-limited type of system, a series of simulations were performed. Assuming an output mode from the TIR mirror discussed in section 6.2.1, two different arrangements of output apertures were propagated to the far field. One is a full 2D array, and the other is a Costas array [202], the 2D equivalent of a Golomb ruler with the mathematically minimum cross-correlation between elements. Costas arrays only have one element per column, so such an output could be created simply by adding vertical couplers to the end of a 1D OPA PIC at different distances. These are the minimal possible sparse 2D array, shown as a limiting case. Denser 2D arrays can provide better performance if the complexity of 2D routing is acceptable.

The results for a 16-channel sparse OPA compared to a full 2D 16x16 OPA are shown in Figure 96 and Figure 97, with 31-channel results in Figure 98 and Figure 99.

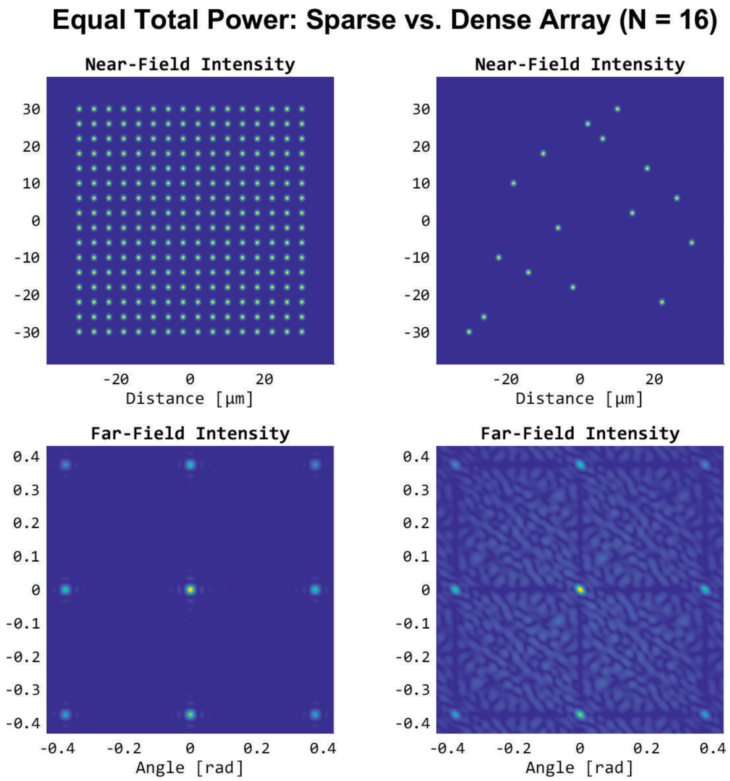

Figure 96: Near field (top) and far field (bottom) optical power distributions of full 16x16 channel (left) and sparse 16 channel (right) optical phased arrays with equal total emitted powers and a horizontal element pitch of 4 μm.

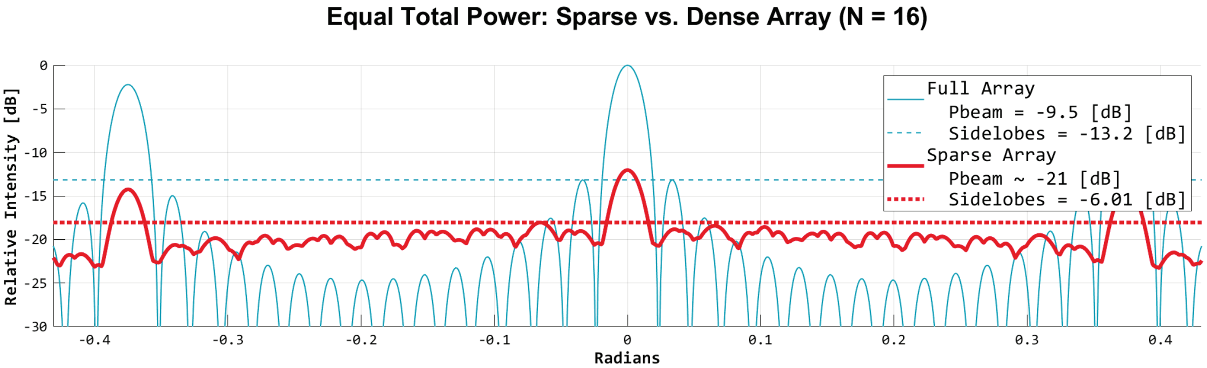

Figure 97: Slice through far-field pattern of full 16x16 channel (thin blue) and 16 channel (thick red) optical phased arrays with equal total emitted powers, with indicated relative main beam powers and sidelobe levels.

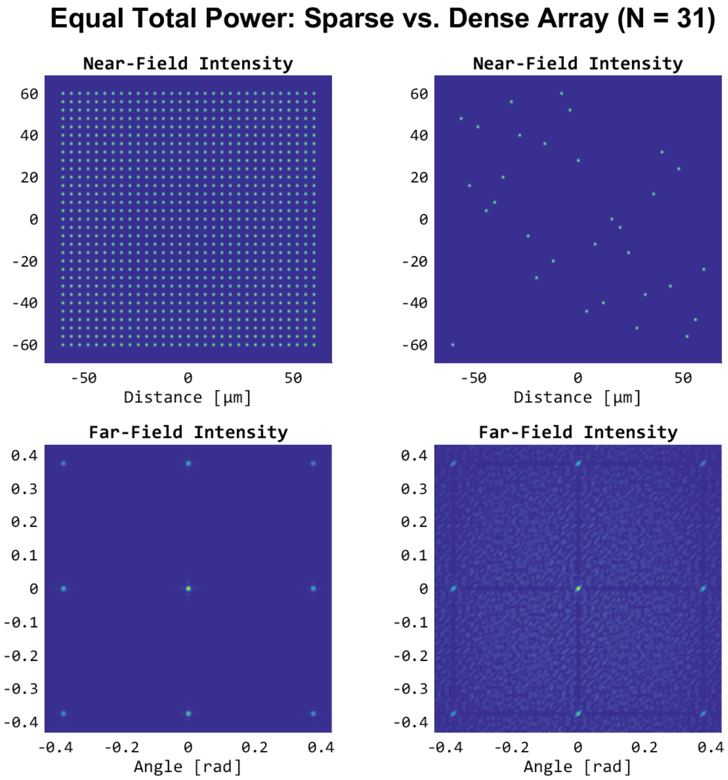

Figure 98: Near field (top) and far field (bottom) optical power distributions of full 31x31 channel (left) and sparse 31 channel (right) optical phased arrays with equal total emitted powers and a horizontal element pitch of 4 μm.

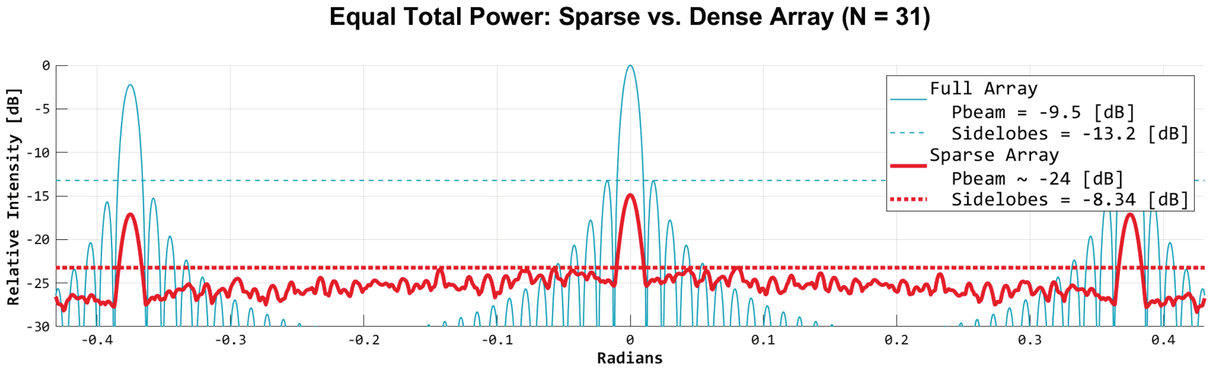

Figure 99: Slice through far-field pattern of full 31x31 channel (thin blue) and 31 channel (thick red) optical phased arrays with equal total emitted powers, with indicated relative main beam powers and sidelobe levels.

It is evident that for only 16 channels, a minimally sparse array can produce a distinct beam, but the sidelobe level is poor. Increasing to 31 channels somewhat improves the sidelobe level. However, a full 31x31 channel OPA is impractical for a PIC, so the results may instead be compared to the typical wavelength-steered PICs in Table 3; 8 dB sidelobe levels are competitive with SiPh systems having dozens to hundreds of channels. The simplicity of the sparse 2D OPA can be traded against specific application requirements.

6.8 Chapter Summary

Chapter 6 has discussed some of the work expected for future iterations of the active-passive GaAs OPA PIC platform presented in Chapter 5. This includes preliminary design updates, known areas requiring additional development, some channel and power scaling limitations, as well as several ideas for improved or novel devices and designs.

It is hoped that this discussion of expected developments will be helpful to future research on this and related topics.

Chapter 7

Conclusion

The demand for optical beam steering capabilities beyond the capability of traditional solutions has spurred the development of integrated photonic solutions to the problem. OPAs are an ideal match between PIC capabilities and beam steering requirements, but typical SiPh PIC solutions struggle to provide GHz-class phase modulation, and are unable to cover common wavelengths for some applications such as topographic LiDAR. GaAs-based PIC technologies can provide fast and efficient electro-optical phase modulators with a wide functional wavelength, and importantly offer well-developed gain materials.

The work presented in this dissertation has developed a GaAs-based PIC platform that is ideally suited for OPA applications. This includes fast and broadband electro-optic phase modulators to enable GHz-class beam steering, with demonstrated single-sided $V_\pi \cdot L$ phase modulation efficiency ranging from 0.5 V·cm to 1.22 V·cm at wavelengths from 980 nm to 1360 nm. These were leveraged to fabricate and demonstrate a 16-channel optical phased array with phase control featuring 0.92° beamwidth, 15.3° grating-lobe-free steering range, 12 dB sidelobe level, and ≥770 MHz single-element electro-optical bandwidth when operating at 1064 nm. This performance is highly competitive with other published integrated OPA PICs.

This modulator-optimized platform has been further developed with active-passive integration to add gain elements that can enable on-chip lasers and per-channel gain. Successful active-passive fabrication demonstrated phase modulators with single-sided $V_\pi \cdot L$ phase modulation efficiency of 0.8 V·cm at 1030 nm wavelength as well as other passive elements, paving the way for a fully monolithically integrated PIC platform for OPA applications. Ongoing work is underway to diagnose MQW performance and demonstrate functional gain from the same active-passive integration process in order to demonstrate a monolithically integrated OPA PIC.

References

[1] S. Royo and M. Ballesta-Garcia, “An Overview of Lidar Imaging Systems for Autonomous Vehicles,” *Appl. Sci.*, vol. 9, no. 19, p. 4093, 19, Multidisciplinary Digital Publishing Institute, Jan. 2019. https://doi.org/10/ggwdh5

[2] J. Chang, C. M. Schieler, K. M. Riesing, J. W. Burnside, K. Aquino, and B. S. Robinson, “Body pointing, acquisition and tracking for small satellite laser communication,” *Free-Space Laser Commun. XXXI*, vol. 10910, Mar. 22, 2019, p. 109100P. https://doi.org/10.1117/12.2511159

[3] S. Clark, “SpaceX launches first full batch of laser-equipped Starlink satellites,” *Spacefl. Now*, Sep. 2021. Accessed: Apr. 28, 2022. [Online]. Available: https://spaceflightnow.com/2021/09/14/spacex-launches-first-full-batch-of-laser-equipped-starlink-satellites/

[4] M. Stephen *et al.*, “Integrated Micro-Photonics for Remote Earth Science Sensing (Impress) Lidar,” *IGARSS 2019 - 2019 IEEE Int. Geosci. Remote Sens. Symp.*, Jul. 2019, pp. 4853–4856. https://doi.org/10/ggfxtv

[5] S. Mehta, J. Peach, and A. Weinert, “To Expedite Roadway Identification and Damage Assessment in LiDAR 3D Imagery for Disaster Relief Public Assistance,” *Infrastructures*, vol. 7, no. 3, p. 39, 3, Multidisciplinary Digital Publishing Institute, Mar. 2022. https://doi.org/10/gpnw9t

[6] “Flex Via Drilling | HDI Via Drilling | IC Packaging,” *MKS ESI*. Accessed: Aug. 26, 2023. [Online]. Available: https://www.esi.com/solutions/flex-pcb-processing/

[7] “Technology,” *Civan Lasers*. Accessed: Aug. 26, 2023. [Online]. Available: https://www.civanlasers.com/technology

[8] “Velodyne’s Guide to Lidar Wavelengths,” *Velodyne Lidar*, Nov. 5, 2018. Accessed: Oct. 8, 2023. [Online]. Available: https://velodynelidar.com/blog/guide-to-lidar-wavelengths/

[9] MIT Lincoln Laboratory, “Technology That Confronts Disaster | MIT Lincoln Laboratory.” Accessed: Oct. 8, 2023. [Online]. Available: https://www.ll.mit.edu/impact/technology-confronts-disaster

[10] NASA, “NASA Scientific Visualization Studio | Remote Sensing: Observing the Earth,” Jan. 2003. Accessed: Oct. 8, 2023. [Online]. Available: https://svs.gsfc.nasa.gov/2674/

[11] NASA, *Laser Communications Relay Demonstration (LCRD) Overview*, sec. Technology Demonstration Missions Program, Dec. 7, 2021. Accessed: Oct. 8, 2023. [Online]. Available: https://www.nasa.gov/directorates/stmd/tech-demo-missions-program/laser-communications-relay-demonstration-lcrd-overview/

[12] MKS ESI, “Rigid PCB Processing.” Accessed: Oct. 8, 2023. [Online]. Available: https://www.esi.com/products/rigid-pcb-processing/

[13] “Exploring the Potential of Dynamic Beam Lasers: Advancements in Welding Technology,” *Civan Lasers*, Jun. 2023. Accessed: Oct. 8, 2023. [Online]. Available: https://www.civanlasers.com/post/exploring-the-potential-of-dynamic-beam-lasers-advancements-in-welding-technology

[14] “Puck Lidar Sensor,” *Velodyne Lidar*. Accessed: Apr. 28, 2022. [Online]. Available: https://velodynelidar.com/products/puck/

[15] A. Seas, B. Robinson, T. Shih, F. Khatri, and M. Brumfield, “Optical communications systems for NASA’s human space flight missions,” *Int. Conf. Space Opt. — ICSO 2018*, vol. 11180, Jul. 12, 2019, pp. 182–191. https://doi.org/10/gr3mkw

[16] “MR-15-30,” *Optotune*. Accessed: Oct. 8, 2023. [Online]. Available: https://www.optotune.com/mr1530

[17] Д. И. vectorization, *English: Acousto-optic Modulator*, Jun. 2022. Accessed: Oct. 8, 2023. [Online]. Available: https://commons.wikimedia.org/wiki/File:Acousto-optic_Modulator-en.svg

[18] S. E. Miller, “Integrated Optics: An Introduction,” *Bell Syst. Tech. J.*, vol. 48, no. 7, pp. 2059–2069, 1969. https://doi.org/10.1002/j.1538-7305.1969.tb01165.x

[19] R. N. Hall, G. E. Fenner, J. D. Kingsley, T. J. Soltys, and R. O. Carlson, “Coherent Light Emission From GaAs Junctions,” *Phys. Rev. Lett.*, vol. 9, no. 9, pp. 366–368, American Physical Society, Nov. 1962. https://doi.org/10.1103/PhysRevLett.9.366

[20] M. I. Nathan, W. P. Dumke, G. Burns, F. H. Dill, and G. Lasher, “STIMULATED EMISSION OF RADIATION FROM GaAs *p-n* JUNCTIONS,” *Appl. Phys. Lett.*, vol. 1, no. 3, pp. 62–64, Nov. 1962. https://doi.org/10.1063/1.1777371

[21] T. M. Quist *et al.*, “SEMICONDUCTOR MASER OF GaAs,” *Appl. Phys. Lett.*, vol. 1, no. 4, pp. 91–92, Dec. 1962. https://doi.org/10.1063/1.1753710

[22] N. Holonyak and S. F. Bevacqua, “COHERENT (VISIBLE) LIGHT EMISSION FROM Ga(As_{1-x}P_x) JUNCTIONS,” *Appl. Phys. Lett.*, vol. 1, no. 4, pp. 82–83, Dec. 1962. https://doi.org/10.1063/1.1753706

[23] Z. I. Alferov, V. M. Andreev, E. L. Portnoy, and M. K. Trukan, “AlAs-GaAs heterojunction injection lasers with a low room-temperature threshold,” *Fiz Tekh Poluprov*, vol. 3, pp. 1328–1332, 1969.

[24] Z. Alferov, “Double heterostructure lasers: early days and future perspectives,” *IEEE J. Sel. Top. Quantum Electron.*, vol. 6, no. 6, pp. 832–840, Nov. 2000. https://doi.org/10.1109/2944.902131

[25] M. Smit, J. van der Tol, and M. Hill, “Moore’s law in photonics,” *Laser Photonics Rev.*, vol. 6, no. 1, pp. 1–13, 2012. https://doi.org/10.1002/lpor.201100001

[26] B. J. Isaac, B. Song, S. Pinna, L. A. Coldren, and J. Klamkin, “Indium Phosphide Photonic Integrated Circuit Transceiver for FMCW LiDAR,” *IEEE J. Sel. Top. Quantum Electron.*, vol. 25, no. 6, pp. 1–7, Nov. 2019. https://doi.org/10/gf5gn4

[27] N. Margalit, C. Xiang, S. M. Bowers, A. Bjorlin, R. Blum, and J. E. Bowers, “Perspective on the future of silicon photonics and electronics,” *Appl. Phys. Lett.*, vol. 118, no. 22, p. 220501, Jun. 2021. https://doi.org/10.1063/5.0050117

[28] Y. Blanchard and P. van Genderen, “A German radar chain, facing the British Chain Home during WW II,” *2014 11th Eur. Radar Conf.*, Oct. 2014, pp. 29–32. https://doi.org/10.1109/eurad.2014.6991199

[29] K. Inagaki and Y. Karasawa, “Ultrahigh-speed optical-beam steering by optical phased array antenna,” *Free-Space Laser Commun. Technol. VIII*, vol. 2699, Apr. 22, 1996, pp. 210–218. https://doi.org/10.1117/12.238413

[30] P. Mcmanamon *et al.*, “Optical phased array technology,” *Proc. IEEE*, vol. 84, pp. 268–298, Mar. 1996. https://doi.org/10.1109/5.482231

[31] “Excalibur Prototype Extends Reach of High-Energy Lasers.” Accessed: Oct. 28, 2018. [Online]. Available: https://www.darpa.mil/news-events/2014-03-06

[32] Angel Flores, Benjamin Pulford, Craig Robin, and Thomas Shay, “Coherent laser beam combining,” Technical Paper AFRL-RD-PS-TP-2015-0007, Oct. 2012.

[33] X. Wang *et al.*, “High-precision two-dimensional beam steering with a 64-element optical fiber phased array,” *Appl. Opt.*, vol. 60, no. 31, pp. 10002–10008, Nov. 2021. https://doi.org/10/gm98jz

[34] H. Fathi, M. Närhi, and R. Gumenyuk, “Towards Ultimate High-Power Scaling: Coherent Beam Combining of Fiber Lasers,” *Photonics*, vol. 8, no. 12, p. 566, 12, Multidisciplinary Digital Publishing Institute, Dec. 2021. https://doi.org/10/gsnfhv

[35] E. Otón, J. Pérez-Fernández, D. López-Molina, X. Quintana, J. M. Otón, and M. A. Geday, “Reliability of Liquid Crystals in Space Photonics,” *IEEE Photonics J.*, vol. 7, no. 4, pp. 1–9, Aug. 2015. https://doi.org/10.1109/jphot.2015.2451626

[36] W. Yang *et al.*, “High speed optical phased array using high contrast grating all-pass filters,” *Opt. Express*, vol. 22, no. 17, pp. 20038–20044, Aug. 2014. https://doi.org/10.1364/oe.22.020038

[37] Y. Wang, G. Zhou, K. Yu, and M. C. Wu, “Large-scale MEMS-actuated 2-D optical phased arrays,” *2018 IEEE Micro Electro Mech. Syst. MEMS*, Belfast, Jan. 2018, pp. 21–24. https://doi.org/10/gfzm7j

[38] D. K. Serkland, K. D. Choquette, G. R. Hadley, K. M. Geib, and A. A. Allerman, “Two-element phased array of antiguided vertical-cavity lasers,” *Appl. Phys. Lett.*, vol. 75, no. 24, pp. 3754–3756, Dec. 1999. https://doi.org/10.1063/1.125445

[39] K. Sayyah *et al.*, “Two-dimensional pseudo-random optical phased array based on tandem optical injection locking of vertical cavity surface emitting lasers,” *Opt. Express*, vol. 23, no. 15, pp. 19405–19416, Jul. 2015. https://doi.org/10.1364/oe.23.019405

[40] M. Zhang, C. Wang, P. Kharel, D. Zhu, and M. Lončar, “Integrated lithium niobate electro-optic modulators: when performance meets scalability,” *Optica*, vol. 8, no. 5, pp. 652–667, Optical Society of America, May 2021. https://doi.org/10/gj47x3

[41] H. Zhang, Z. Zhang, J. Lv, C. Peng, and W. Hu, “Fast beam steering enabled by a chip-scale optical phased array with 8 × 8 elements,” *Opt. Commun.*, vol. 461, p. 125267, Apr. 2020. https://doi.org/10/gjttqn

[42] “Optical Phased Array LiDAR,” *Analog Photonics*, Jun. 2021. Accessed: Oct. 8, 2023. [Online]. Available: https://www.analogphotonics.com/product/phased-array-lidar/

[43] R. Fatemi, A. Khachaturian, and A. Hajimiri, “A Low Power PWM Optical Phased Array Transmitter with 16° Field-of-View and 0.8° Beamwidth,” *2018 IEEE Radio Freq. Integr. Circuits Symp. RFIC*, Jun. 2018, pp. 28–31. https://doi.org/10.1109/rfic.2018.8428847

[44] J. C. Hulme *et al.*, “Fully integrated hybrid silicon two dimensional beam scanner,” *Opt. Express*, vol. 23, no. 5, pp. 5861–5874, Mar. 2015. https://doi.org/10.1364/oe.23.005861

[45] M. Zadka, Y.-C. Chang, A. Mohanty, C. T. Phare, S. P. Roberts, and M. Lipson, “On-chip platform for a phased array with minimal beam divergence and wide field-of-view,” *Opt. Express*, vol. 26, no. 3, pp. 2528–2534, Feb. 2018. https://doi.org/10.1364/oe.26.002528

[46] C. V. Poulton *et al.*, “Coherent LiDAR With an 8,192-Element Optical Phased Array and Driving Laser,” *IEEE J. Sel. Top. Quantum Electron.*, pp. 1–8, 2022. https://doi.org/10/gr3mkj

[47] Z. Zhang *et al.*, “A Tri-Layer Si3N4-on-Si Optical Phased Array with High Angular Resolution,” *IEEE Photonics Technol. Lett.*, pp. 1–1, 2022. https://doi.org/10/gs3gf9

[48] S. A. Miller *et al.*, “Large-scale optical phased array using a low-power multi-pass silicon photonic platform,” *Optica*, vol. 7, no. 1, pp. 3–6, Optica Publishing Group, Jan. 2020. https://doi.org/10/ggfxzn

[49] R. Chen *et al.*, “Breaking the temporal and frequency congestion of LiDAR by parallel chaos,” *Nat. Photonics*, vol. 17, no. 4, pp. 306–314, 4, Nature Publishing Group, Apr. 2023. https://doi.org/10.1038/s41566-023-01158-4

[50] A. W. Yu *et al.*, “A 16-beam non-scanning swath mapping laser altimeter instrument,” *Solid State Lasers XXII Technol. Devices*, vol. 8599, Mar. 18, 2013, pp. 147–161. https://doi.org/10/gs3ghn

[51] H. Zhou, Y. Chen, J. Hyyppä, and S. Li, “An overview of the laser ranging method of space laser altimeter,” *Infrared Phys. Technol.*, vol. 86, pp. 147–158, Nov. 2017. https://doi.org/10.1016/j.infrared.2017.09.011

[52] J. Guo, X. Fei, P. Ge, Z. Li, Y. Lv, and L. Sheng, “A 1064 nm single-photon lidar for three-dimensional imaging,” *J. Phys. Conf. Ser.*, vol. 1983, no. 1, p. 012093, IOP Publishing, Jul. 2021. https://doi.org/10.1088/1742-6596/1983/1/012093

[53] S. Chung, M. Nakai, and H. Hashemi, “Low-power thermo-optic silicon modulator for large-scale photonic integrated systems,” *Opt. Express*, vol. 27, no. 9, pp. 13430–13459, Apr. 2019. https://doi.org/10/ggf2wn

[54] J. Mulcahy, F. H. Peters, and X. Dai, “Modulators in Silicon Photonics—Heterogenous Integration & and Beyond,” *Photonics*, vol. 9, no. 1, p. 40, 1, Multidisciplinary Digital Publishing Institute, Jan. 2022. https://doi.org/10/gpjd29

[55] F. Gao *et al.*, “Comprehensive investigation of thermo-optic phase shifters on a multi-layered SiN-on-SOI platform,” *J. Light. Technol.*, pp. 1–7, 2023. https://doi.org/10/gs3ghp

[56] W. Xie *et al.*, “Heterogeneous silicon photonics sensing for autonomous cars [Invited],” *Opt. Express*, vol. 27, no. 3, pp. 3642–3663, Optica Publishing Group, Feb. 2019. https://doi.org/10.1364/OE.27.003642

[57] Z. Ruan *et al.*, “High-Performance Electro-Optic Modulator on Silicon Nitride Platform with Heterogeneous Integration of Lithium Niobate,” *Laser Photonics Rev.*, vol. n/a, no. n/a, p. 2200327, Feb. 2023. https://doi.org/10/gr3mj9

[58] A. Rahim *et al.*, “Taking silicon photonics modulators to a higher performance level: state-of-the-art and a review of new technologies,” *Adv. Photonics*, vol. 3, no. 2, p. 024003, SPIE, Apr. 2021. https://doi.org/10/gjvd3x

[59] S. Tan *et al.*, “Low-power consumption InP-based optical phase arrays with non-uniformly spaced output waveguides,” *Opt. Express*, vol. 31, no. 2, pp. 3199–3211, Optica Publishing Group, Jan. 2023. https://doi.org/10/gs3ghs

[60] J. Midkiff *et al.*, “Optical phased array beam steering in the mid-infrared on an InP-based platform,” *Optica*, vol. 7, no. 11, pp. 1544–1547, Optica Publishing Group, Nov. 2020. https://doi.org/10/ghhxrx

[61] M. Gagino, M. B. J. Van Rijn, E. A. J. M. Bente, M. K. Smit, and V. Dolores-Calzadilla, “Broadband operation of an InP optical phased array,” *IEEE Photonics Technol. Lett.*, pp. 1–1, 2022. https://doi.org/10/gr3mkr

[62] L. Jisan *et al.*, “Real-time LIDAR imaging by solid-state single chip beam scanner,” *Electron. Imaging*, vol. 34, pp. 1–4, Society for Imaging Science and Technology, Jan. 2022. https://doi.org/10/gr3mkp

[63] C.-W. Chow *et al.*, “Actively Controllable Beam Steering Optical Wireless Communication (OWC) Using Integrated Optical Phased Array (OPA),” *J. Light. Technol.*, pp. 1–7, 2022. https://doi.org/10/gs3gf7

[64] W. Guo *et al.*, “Two-Dimensional Optical Beam Steering With InP-Based Photonic Integrated Circuits,” *IEEE J. Sel. Top. Quantum Electron.*, vol. 19, no. 4, pp. 6100212–6100212, Jul. 2013. https://doi.org/10.1109/jstqe.2013.2238218

[65] Y. Guo, Y. Guo, C. Li, H. Zhang, X. Zhou, and L. Zhang, “Integrated Optical Phased Arrays for Beam Forming and Steering,” *Appl. Sci.*, vol. 11, no. 9, p. 4017, 9, Multidisciplinary Digital Publishing Institute, Jan. 2021. https://doi.org/10/gjts5f

[66] J. C. Norman, D. Jung, Y. Wan, and J. E. Bowers, “Perspective: The future of quantum dot photonic integrated circuits,” *APL Photonics*, vol. 3, no. 3, p. 030901, Mar. 2018. https://doi.org/10.1063/1.5021345

[67] C. D. Dobson, J. Franks, and F. S. Keeble, “Characteristics of GaAs lasers near room temperature,” *IEEE J. Quantum Electron.*, vol. 4, no. 4, pp. 151–154, Apr. 1968. https://doi.org/10/bkfgtp

[68] F. E. Goodwin, “A review of operational laser communication systems,” *Proc. IEEE*, vol. 58, no. 10, pp. 1746–1752, Oct. 1970. https://doi.org/10/bv4k7q

[69] I. Hayashi, “Recent progress in semiconductor lasers — cw GaAs lasers are now ready for new applications,” *Appl. Phys.*, vol. 5, no. 1, pp. 25–36, Oct. 1974. https://doi.org/10/dct293

[70] P. A. Verrinder *et al.*, “Gallium Arsenide Photonic Integrated Circuit Platform for Tunable Laser Applications,” *IEEE J. Sel. Top. Quantum Electron.*, vol. 28, no. 1: Semiconductor Lasers, pp. 1–9, Jan. 2022. https://doi.org/10/gmzfnn

[71] L. Wang *et al.*, “High Performance 1.3 µm Aluminum-Free Quantum Dot Lasers Grown by MOCVD,” *2020 Opt. Fiber Commun. Conf. Exhib. OFC*, Mar. 2020, pp. 1–3.

[72] J. J. Coleman, “Strained-layer InGaAs quantum-well heterostructure lasers,” *IEEE J. Sel. Top. Quantum Electron.*, vol. 6, no. 6, pp. 1008–1013, Nov. 2000. https://doi.org/10/bhv8mk

[73] J. G. Mendoza-Alvarez *et al.*, “Analysis of depletion edge translation lightwave modulators,” *J. Light. Technol.*, vol. 6, no. 6, pp. 793–808, Jun. 1988. https://doi.org/10/bvn68f

[74] J. Faist and F. K. Reinhart, “Phase modulation in GaAs/AlGaAs double heterostructures. I. Theory,” *J. Appl. Phys.*, vol. 67, no. 11, pp. 6998–7005, Jun. 1990. https://doi.org/10/bp3pdz

[75] S. S. Lee, R. V. Ramaswamy, and V. S. Sundaram, “Analysis and design of high-speed high-efficiency GaAs-AlGaAs double-heterostructure waveguide phase modulator,” *IEEE J. Quantum Electron.*, vol. 27, no. 3, pp. 726–736, Mar. 1991. https://doi.org/10/bhd2dh

[76] C. A. Berseth, C. Wuethrich, and F. K. Reinhart, “The electro-optic coefficients of GaAs: Measurements at 1.32 and 1.52 µm and study of their dispersion between 0.9 and 10 µm,” *J. Appl. Phys.*, vol. 71, no. 6, pp. 2821–2825, American Institute of Physics, Mar. 1992. https://doi.org/10/ctg32h

[77] S. Adachi, “Dispersion of the linear electro-optic coefficients in GaAs,” *J. Appl. Phys.*, vol. 72, no. 8, pp. 3702–3704, Oct. 1992. https://doi.org/10/fw3dmx

[78] A. Alping, X. S. Wu, T. R. Hausken, and L. A. Coldren, “Highly efficient waveguide phase modulator for integrated optoelectronics,” *Appl. Phys. Lett.*, vol. 48, no. 19, pp. 1243–1245, May 1986. https://doi.org/10/dsj42c

[79] M. Glick, F. K. Reinhart, G. Weimann, and W. Schlapp, “Quadratic electro-optic light modulation in a GaAs/AlGaAs multiquantum well heterostructure near the excitonic gap,” *Appl. Phys. Lett.*, vol. 48, no. 15, pp. 989–991, Apr. 1986. https://doi.org/10/fgzv6g

[80] D. R. Wight, J. M. Heaton, B. T. Hughes, J. C. H. Birbeck, K. P. Hilton, and D. J. Taylor, “Novel phased array optical scanning device implemented using GaAs/AlGaAs technology,” *Appl. Phys. Lett.*, vol. 59, no. 8, pp. 899–901, Aug. 1991. https://doi.org/10/fv8ggb

[81] Z. Wang *et al.*, “Chip scale GaAs optical phased arrays for high speed beam steering,” *Appl. Opt.*, vol. 59, no. 27, pp. 8310–8313, Optica Publishing Group, Sep. 2020. https://doi.org/10/gph92n

[82] “Photonics Simulation Software | Ansys Lumerical.” Accessed: Feb. 7, 2023. [Online]. Available: https://www.ansys.com/products/photonics

[83] “The COMSOL® Software Product Suite,” *COMSOL*. Accessed: Aug. 11, 2023. [Online]. Available: https://www.comsol.com/products

[84] J. Faist and F. K. Reinhart, “Phase modulation in GaAs/AlGaAs double heterostructures. II. Experiment,” *J. Appl. Phys.*, vol. 67, no. 11, pp. 7006–7012, Jun. 1990. https://doi.org/10/cj4hq7

[85] A. Alping and L. A. Coldren, “Electrorefraction in GaAs and InGaAsP and its application to phase modulators,” *J. Appl. Phys.*, vol. 61, no. 7, pp. 2430–2433, Apr. 1987. https://doi.org/10/cvx8p7

[86] V. V. Zolotarev *et al.*, “Enhancement of the refractive index modulation in a modulator based on GaAs/AlGaAs quantum wells,” *Semicond. Sci. Technol.*, vol. 34, no. 9, p. 095005, IOP Publishing, Jul. 2019. https://doi.org/10/gh3rph

[87] D. C. Hutchings, *The Nonlinear Optical Properties of Semiconductors*. Accessed: Sep. 2, 2022. [Online]. Available: https://www.gla.ac.uk/media/Media_237680_smxx.pdf

[88] “Basic Parameters of Gallium Arsenide (GaAs).” Accessed: Aug. 11, 2023. [Online]. Available: https://www.ioffe.ru/SVA/NSM/Semicond/GaAs/basic.html

[89] F. Stern, “Dispersion of the Index of Refraction Near the Absorption Edge of Semiconductors,” *Phys. Rev.*, vol. 133, no. 6A, pp. A1653–A1664, Mar. 1964. https://doi.org/10/d32vwm

[90] H. C. Huang, S. Yee, and M. Soma, “The carrier effects on the change of refractive index for n-type GaAs at λ=1.06,1.3, and 1.55 µm,” *J. Appl. Phys.*, vol. 67, no. 3, pp. 1497–1503, Feb. 1990. https://doi.org/10/dzmv7q

[91] H. C. Huang and S. Yee, “Change in refractive index for p-type GaAs at λ=1.06, 1.3, and 1.55 µm due to free carriers,” *J. Appl. Phys.*, vol. 70, no. 2, pp. 925–929, Jul. 1991. https://doi.org/10/bqx534

[92] J. R. D'Rozario, S. J. Polly, G. T. Nelson, D. Wilt, and S. M. Hubbard, "Modeling free-carrier absorption in ultrathin III-V solar cells with light management," *Opt. Express*, vol. 30, no. 5, pp. 7096–7109, Optica Publishing Group, Feb. 2022. https://doi.org/10/gs3ggb

[93] M. Sotoodeh, A. H. Khalid, and A. A. Rezazadeh, "Empirical low-field mobility model for III–V compounds applicable in device simulation codes," *J. Appl. Phys.*, vol. 87, no. 6, pp. 2890–2900, American Institute of Physics, Feb. 2000. https://doi.org/10/fh59jg

[94] W. G. Spitzer and J. M. Whelan, "Infrared Absorption and Electron Effective Mass in n-Type Gallium Arsenide," *Phys. Rev.*, vol. 114, no. 1, pp. 59–63, Apr. 1959. https://doi.org/10/cprfcr

[95] S. R. Johnson and T. Tiedje, "Temperature dependence of the Urbach edge in GaAs," *J. Appl. Phys.*, vol. 78, no. 9, pp. 5609–5613, Nov. 1995. https://doi.org/10/djjwzx

[96] D. I. Babic *et al.*, "Design and analysis of double-fused 1.55-/spl mu/m vertical-cavity lasers," *IEEE J. Quantum Electron.*, vol. 33, no. 8, pp. 1369–1383, Aug. 1997. https://doi.org/10/cg9rch

[97] W. J. Turner and W. E. Reese, "Absorption Data of Laser-Type GaAs at 300° and 77°K," *J. Appl. Phys.*, vol. 35, no. 2, pp. 350–352, Feb. 1964. https://doi.org/10/cxp75k

[98] H. C. Casey, D. D. Sell, and K. W. Wecht, "Concentration dependence of the absorption coefficient for n− and p−type GaAs between 1.3 and 1.6 eV," *J. Appl. Phys.*, vol. 46, no. 1, pp. 250–257, Jan. 1975. https://doi.org/10/bm4zhf

[99] T. Kageyama *et al.*, "Optical absorption coefficient of carbon-doped GaAs epitaxial layer by means of propagation -loss measurement of waveguide for long wavelength VCSEL," *2009 IEEE Int. Conf. Indium Phosphide Relat. Mater.*, Newport Beach, CA, USA, May 2009, pp. 351–354. https://doi.org/10/d6kb6d

[100] B. Bennett and R. Soref, "Electrorefraction and electroabsorption in InP, GaAs, GaSb, InAs, and InSb," *IEEE J. Quantum Electron.*, vol. 23, no. 12, pp. 2159–2166, Dec. 1987. https://doi.org/10/crr4h3

[101] G. Hagn, "Electro-optic effects and their application in indium phosphide waveguide devices for fibre optic access networks," Doctoral Thesis, ETH Zurich, 2001. Accessed: May 17, 2023. [Online]. Available: https://www.research-collection.ethz.ch/handle/20.500.11850/146406

[102] M. Nickerson, *LumericalTools*, Lumerical, MATLAB, Apr. 2023. Accessed: May 10, 2023. [Online]. Available: https://github.com/nickersonm/LumericalTools

[103] S. Gehrsitz, F. K. Reinhart, C. Gourgon, N. Herres, A. Vonlanthen, and H. Sigg, "The refractive index of AlxGa1−xAs below the band gap: Accurate determination and empirical modeling," *J. Appl. Phys.*, vol. 87, no. 11, pp. 7825–7837, May 2000. https://doi.org/10/b5drvx

[104] S. Adachi, "Optical dispersion relations for GaP, GaAs, GaSb, InP, InAs, InSb, AlxGa1−xAs, and In1−xGaxAsyP1−y," *J. Appl. Phys.*, vol. 66, no. 12, pp. 6030–6040, Dec. 1989. https://doi.org/10/d7xtn3

[105] D. E. Aspnes, S. M. Kelso, R. A. Logan, and R. Bhat, "Optical properties of AlxGa1−x As," *J. Appl. Phys.*, vol. 60, no. 2, pp. 754–767, Jul. 1986. https://doi.org/10/d35spp

[106] K. Papatryfonos *et al.*, "Refractive indices of MBE-grown AlxGa(1−x)As ternary alloys in the transparent wavelength region," *AIP Adv.*, vol. 11, no. 2, p. 025327, American Institute of Physics, Feb. 2021. https://doi.org/10/gjs47z

[107]S. Adachi, "GaAs, AlAs, and AlxGa1−xAs: Material parameters for use in research and device applications," *J. Appl. Phys.*, vol. 58, no. 3, pp. R1–R29, Aug. 1985. https://doi.org/10/fvv7br

[108] A. K. Saxena, "Electron mobility in Ga_{1-x}Al_xAs alloys," *Phys. Rev. B*, vol. 24, no. 6, pp. 3295–3302, American Physical Society, Sep. 1981. https://doi.org/10.1103/PhysRevB.24.3295

[109] "Ansys Lumerical CHARGE | 3D Charge Transport Solver." Accessed: Feb. 7, 2023. [Online]. Available: https://www.ansys.com/products/photonics/charge

[110] S. L. Chuang, *Physics of Optoelectronic Devices*, 1st edition, New York: Wiley-Interscience, 1995.

[111] L. A. Coldren, S. W. Corzine, and M. L. Mashanovitch, *Diode Lasers and Photonic Integrated Circuits*, John Wiley & Sons, 2012.

[112] “Homepage,” *Nazca Des.* Accessed: May 10, 2023. [Online]. Available: https://nazca-design.org/

[113] M. Nickerson, *photonics-pdk*, Python, Apr. 2023. Accessed: May 10, 2023. [Online]. Available: https://github.com/nickersonm/photonics-pdk

[114] “UCSB Nanofab: U.C. Santa Barbara Cleanroom: Semiconductor Manufacturing Research,” *UCSB NanoFab*. Accessed: Feb. 3, 2023. [Online]. Available: https://www.nanofab.ucsb.edu

[115] R. Regener and W. Sohler, “Loss in low-finesse Ti:LiNbO3 optical waveguide resonators,” *Appl. Phys. B*, vol. 36, no. 3, pp. 143–147, Mar. 1985. https://doi.org/10/b9h5xb

[116] B. Arar *et al.*, “Method for in-depth characterization of electro-optic phase modulators,” *Appl. Opt.*, vol. 56, no. 4, pp. 1246–1252, Optical Society of America, Feb. 2017. https://doi.org/10/gg4zx6

[117] “Phased Array Antenna Patterns—Part 3: Sidelobes and Tapering | Analog Devices.” Accessed: Feb. 13, 2023. [Online]. Available: https://www.analog.com/en/analog-dialogue/articles/phased-array-antenna-patterns-part3.html

[118] B. Pulford, “LOCSET phase locking : operation, diagnostics, and applications,” *Opt. Sci. Eng. ETDs*, Feb. 2012. [Online]. Available: https://digitalrepository.unm.edu/ose_etds/33

[119] M. Nickerson, P. Verrinder, L. Wang, B. Song, and J. Klamkin, “Broadband Optical Phase Modulator with Low Residual Amplitude Modulation,” *Opt. Adv. Photonics Congr. 2022 Pap. IW4B4*, Jul. 24, 2022. https://doi.org/10/grtvck

[120] M. Nickerson, B. Song, J. Brookhyser, G. Erwin, J. Kleinert, and J. Klamkin, “Gallium arsenide optical phased array photonic integrated circuit,” *Opt. Express*, vol. 31, no. 17, pp. 27106–27122, Aug. 2023. https://doi.org/10.1364/OE.492556

[121] L. B. Soldano and E. C. M. Pennings, “Optical multi-mode interference devices based on self-imaging: principles and applications,” *J. Light. Technol.*, vol. 13, no. 4, pp. 615–627, Apr. 1995. https://doi.org/10/b3k54j

[122] R. Spickermann, N. Dagli, and M. G. Peters, “GaAs/AlGaAs electro-optic modulator with bandwidth >40 GHz,” *Electron. Lett.*, vol. 31, no. 11, pp. 915–916, May 1995. https://doi.org/10/dcqq23

[123] S. Dogru and N. Dagli, “0.77-V drive voltage electro-optic modulator with bandwidth exceeding 67 GHz,” *Opt. Lett.*, vol. 39, no. 20, pp. 6074–6077, Optica Publishing Group, Oct. 2014. https://doi.org/10/grj46q

[124] R. G. Walker and Y. Zhou, “The Design of 50 GHz Gallium Arsenide Electro-Optic Modulator Arrays for Satellite Communications Systems,” *Front. Phys.*, vol. 9, 2021. https://doi.org/10/gs3ghd

[125] B. Arar *et al.*, “Double-heterostructure ridge-waveguide GaAs/AlGaAs phase modulator for 780 nm lasers,” *Appl. Phys. B*, vol. 116, no. 1, pp. 175–181, Jul. 2014. https://doi.org/10/gs3gg8

[126] J. H. Shin and N. Dagli, “Ultralow Drive Voltage Substrate Removed GaAs/AlGaAs Electro-Optic Modulators at 1550 nm,” *IEEE J. Sel. Top. Quantum Electron.*, vol. 19, no. 6, pp. 150–157, Nov. 2013. https://doi.org/10/gs3gg9

[127] J. Shin, Y.-C. Chang, and N. Dagli, “0.3V drive voltage GaAs⁄AlGaAs substrate removed Mach–Zehnder intensity modulators,” *Appl. Phys. Lett.*, vol. 92, no. 20, p. 201103, May 2008. https://doi.org/10/dqgzh7

[128] Y. T. Byun, K. H. Park, S. H. Kim, S. S. Choi, J. C. Yi, and T. K. Lim, “Efficient single-mode GaAs/AlGaAs W waveguide phase modulator with a low propagation loss,” *Appl. Opt.*, vol. 37, no. 3, pp. 496–501, Jan. 1998. https://doi.org/10/c8v6fq

[129] K. Komatsu, Y. Kohno, Y. Nakano, and T. Tanemura, “Large-Scale Monolithic InP-Based Optical Phased Array,” *IEEE Photonics Technol. Lett.*, vol. 33, no. 20, pp. 1123–1126, Oct. 2021. https://doi.org/10/gnbff6

[130] F. Valdez, V. Mere, and S. Mookherjea, “100 GHz bandwidth, 1 volt integrated electro-optic Mach–Zehnder modulator at near-IR wavelengths,” *Optica*, vol. 10, no. 5, pp. 578–584, Optica Publishing Group, May 2023. https://doi.org/10/gsfmrv

[131] Y. Li *et al.*, “High-Performance Mach–Zehnder Modulator Based on Thin-Film Lithium Niobate with Low Voltage-Length Product,” *ACS Omega*, vol. 8, no. 10, pp. 9644–9651, American Chemical Society, Mar. 2023. https://doi.org/10/gr3mjz

[132] S. Xue *et al.*, “Full-spectrum visible electro-optic modulator,” *Optica*, vol. 10, no. 1, pp. 125–126, Optica Publishing Group, Jan. 2023. https://doi.org/10/gs3ghv

[133] N. Jagatpal, A. J. Mercante, A. N. R. Ahmed, and D. W. Prather, “Thin Film Lithium Niobate Electro-Optic Modulator for 1064 nm Wavelength,” *IEEE Photonics Technol. Lett.*, vol. 33, no. 5, pp. 271–274, Mar. 2021. https://doi.org/10/gr3mjt

[134] C. Wang *et al.*, “Integrated lithium niobate electro-optic modulators operating at CMOS-compatible voltages,” *Nature*, vol. 562, no. 7725, pp. 101–104, 7725, Nature Publishing Group, Oct. 2018. https://doi.org/10/gd8dtq

[135] M. He *et al.*, “High-performance hybrid silicon and lithium niobate Mach–Zehnder modulators for 100 Gbit s−1 and beyond,” *Nat. Photonics*, vol. 13, no. 5, pp. 359–364, 5, Nature Publishing Group, May 2019. https://doi.org/10/ggft59

[136] P. O. Weigel *et al.*, “Bonded thin film lithium niobate modulator on a silicon photonics platform exceeding 100 GHz 3-dB electrical modulation bandwidth,” *Opt. Express*, vol. 26, no. 18, pp. 23728–23739, Optica Publishing Group, Sep. 2018. https://doi.org/10/gh5522

[137] X. Xiao *et al.*, “High-speed, low-loss silicon Mach–Zehnder modulators with doping optimization,” *Opt. Express*, vol. 21, no. 4, pp. 4116–4125, Optica Publishing Group, Feb. 2013. https://doi.org/10/ggmn3j

[138] A. Liu *et al.*, “Recent development in a high-speed silicon optical modulator based on reverse-biased pn diode in a silicon waveguide,” *Semicond. Sci. Technol.*, vol. 23, no. 6, p. 064001, May 2008. https://doi.org/10/d4p27g

[139] M. C. Shin *et al.*, “Chip-scale blue light phased array,” *Opt. Lett.*, vol. 45, no. 7, pp. 1934–1937, Optical Society of America, Apr. 2020. https://doi.org/10/ggpk46

[140] W. Ma *et al.*, “Practical two-dimensional beam steering system using an integrated tunable laser and an optical phased array,” *Appl. Opt.*, vol. 59, no. 32, pp. 9985–9994, Optica Publishing Group, Nov. 2020. https://doi.org/10/gr3mkg

[141] S. Chung, H. Abediasl, and H. Hashemi, “A Monolithically Integrated Large-Scale Optical Phased Array in Silicon-on-Insulator CMOS,” *IEEE J. Solid-State Circuits*, vol. 53, no. 1, pp. 275–296, Jan. 2018. https://doi.org/10.1109/jssc.2017.2757009

[142] D. Kwong *et al.*, “On-chip silicon optical phased array for two-dimensional beam steering,” *Opt. Lett.*, vol. 39, no. 4, p. 941, Feb. 2014. https://doi.org/10.1364/ol.39.000941

[143] J. K. Doylend, M. J. R. Heck, J. T. Bovington, J. D. Peters, L. A. Coldren, and J. E. Bowers, “Two-dimensional free-space beam steering with an optical phased array on silicon-on-insulator,” *Opt. Express*, vol. 19, no. 22, pp. 21595–21604, Optica Publishing Group, Oct. 2011. https://doi.org/10/c33dms

[144] S. A. Shakir, D. L. Fried, E. A. Pease, T. J. Brennan, and T. M. Dolash, “Efficient matrix approach to optical wave propagation and Linear Canonical Transforms,” *Opt. Express*, vol. 23, no. 20, pp. 26853–26862, Optica Publishing Group, Oct. 2015. https://doi.org/10/gg7pqt

[145] G. Yue and Y. Li, “Integrated lithium niobate optical phased array for two-dimensional beam steering,” arXiv:2303.15774, arXiv, Mar. 2023. https://doi.org/10.48550/arXiv.2303.15774

[146] H. Qiu, Y. Liu, X. Meng, X. Guan, Y. Ding, and H. Hu, “Bidirectional high sidelobe suppression silicon optical phased array,” *Photonics Res.*, vol. 11, no. 4, pp. 659–668, Optica Publishing Group, Apr. 2023. https://doi.org/10/gs3ggt

[147] D. Liang *et al.*, “Grating lobe-free silicon optical phased array with periodically bending modulation of dense antennas,” *Opt. Express*, vol. 31, no. 7, pp. 11423–11430, Optica Publishing Group, Mar. 2023. https://doi.org/10/gr3mj3

[148] R. Fatemi, A. Khachaturian, and A. Hajimiri, “A Nonuniform Sparse 2-D Large-FOV Optical Phased Array With a Low-Power PWM Drive,” *IEEE J. Solid-State Circuits*, pp. 1–16, 2019. https://doi.org/10.1109/jssc.2019.2896767

[149] D. N. Hutchison *et al.*, “High-resolution aliasing-free optical beam steering,” *Optica*, vol. 3, no. 8, pp. 887–890, Aug. 2016. https://doi.org/10.1364/optica.3.000887

[150] A. Yaacobi, J. Sun, M. Moresco, G. Leake, D. Coolbaugh, and M. R. Watts, “Integrated phased array for wide-angle beam steering,” *Opt. Lett.*, vol. 39, no. 15, pp. 4575–4578, Aug. 2014. https://doi.org/10.1364/ol.39.004575

[151] M. Smit *et al.*, “An introduction to InP-based generic integration technology,” *Semicond. Sci. Technol.*, vol. 29, no. 8, p. 083001, 2014. https://doi.org/10.1088/0268-1242/29/8/083001

[152]S. Arafin and L. A. Coldren, “Advanced InP Photonic Integrated Circuits for Communication and Sensing,” *IEEE J. Sel. Top. Quantum Electron.*, vol. 24, no. 1, pp. 1–12, Jan. 2018. https://doi.org/10.1109/JSTQE.2017.2754583

[153] E. J. Skogen, J. S. Barton, S. P. Denbaars, and L. A. Coldren, “A quantum-well-intermixing process for wavelength-agile photonic integrated circuits,” *IEEE J. Sel. Top. Quantum Electron.*, vol. 8, no. 4, pp. 863–869, Jul. 2002. https://doi.org/10.1109/JSTQE.2002.800849

[154] F. Xia, V. M. Menon, and S. R. Forrest, “Photonic integration using asymmetric twin-waveguide (ATG) technology: part I-concepts and theory,” *IEEE J. Sel. Top. Quantum Electron.*, vol. 11, no. 1, pp. 17–29, Jan. 2005. https://doi.org/10.1109/JSTQE.2004.841466

[155] V. Tolstikhin, “Distributed feedback lasers for regrowth-free multi-guide vertical integration in InP,” *2010 23rd Annu. Meet. IEEE Photonics Soc.*, Nov. 2010, pp. 521–522. https://doi.org/10/fw4ttg

[156] C. Watson, V. Tolstikhin, K. Pimenov, F. Wu, and Y. Logvin, “On-chip emitter for regrowth-free multi-guide vertical integration in InP,” *IEEE Photonic Soc. 24th Annu. Meet.*, Oct. 2011, pp. 336–337. https://doi.org/10/fzb5cf

[157] Z. Liao, “Vertical Integration of Optical Waveguides in the AlGaAs/GaAs Semiconductors,” Thesis, 2018. Accessed: Oct. 10, 2022. [Online]. Available: https://tspace.library.utoronto.ca/handle/1807/91990

[158] C. Liu, G. Zhao, F. Yang, Q. Lu, and W. Guo, “Design of Compact but Fabrication-Tolerant Vertical Coupler for Active–Passive Integration,” *J. Light. Technol.*, vol. 36, no. 3, pp. 755–762, Feb. 2018. https://doi.org/10.1109/JLT.2017.2771362

[159] S. P. Duggan, “Regrowth-free monolithic vertical integration of passive and active waveguides,” Doctoral thesis, University College Cork, 2019. Accessed: Oct. 27, 2022. [Online]. Available: https://cora.ucc.ie/handle/10468/7973

[160] S. Jung *et al.*, “Homogeneous photonic integration of mid-infrared quantum cascade lasers with low-loss passive waveguides on an InP platform,” *Optica*, vol. 6, no. 8, pp. 1023–1030, Optica Publishing Group, Aug. 2019. https://doi.org/10.1364/OPTICA.6.001023

[161] P. Verrinder *et al.*, “SGDBR tunable laser on gallium arsenide for 1030 nm lidar applications,” *2021 27th Int. Semicond. Laser Conf. ISLC*, Oct. 2021, pp. 1–2. https://doi.org/10/gpd82j

[162] P. Verrinder *et al.*, “Widely Tunable 1030 nm Gallium Arsenide Sampled Grating Distributed Bragg Reflector Lasers and Photonic Integrated Circuits,” *2022 Opt. Fiber Commun. Conf. Exhib. OFC*, Mar. 2022, pp. 1–3.

[163] J. Fricke, H. Wenzel, M. Matalla, A. Klehr, and G. Erbert, “980-nm DBR lasers using higher order gratings defined by i-line lithography,” *Semicond. Sci. Technol.*, vol. 20, no. 11, p. 1149, Oct. 2005. https://doi.org/10/c4gffw

[164] K. Paschke, J. Behrendt, M. Maiwald, J. Fricke, H. Wenzel, and G. Erbert, “High power single mode 980nm DBR tapered diode lasers with integrated sixth order surface gratings based on simplified fabrication process,” *Semicond. Lasers Laser Dyn. II*, vol. 6184, Apr. 14, 2006, p. 618401. https://doi.org/10/d8j2bc

[165] R. Millett, K. Hinzer, T. Hall, and H. Schriemer, “Optimal cavity lengths and duty cycles for second-order laterally-coupled distributed feedback lasers,” *2008 1st Microsyst. Nanoelectron. Res. Conf.*, Oct. 2008, pp. 61–64. https://doi.org/10/fhj5nb

[166] R. R. Millett, “Modeling fabrication, and measurement of laterally-coupled distributed feedback lasers,” Thesis, University of Ottawa (Canada), 2009. Accessed: Jan. 31, 2022. [Online]. Available: http://ruor.uottawa.ca/handle/10393/29951

[167] K. Dridi, A. Benhsaien, J. Zhang, and T. Hall, “1.55μm laterally coupled ridge-waveguide DFB lasers with third-order surface grating,” *Photonics North 2012*, vol. 8412, Oct. 24, 2012, pp. 461–466. https://doi.org/10/gpd7st

[168] K. Dridi, A. Benhsaien, J. Zhang, and T. J. Hall, “Narrow Linewidth 1550 nm Corrugated Ridge Waveguide DFB Lasers,” *IEEE Photonics Technol. Lett.*, vol. 26, no. 12, pp. 1192–1195, Jun. 2014. https://doi.org/10/gn3njh

[169] B. Janjua, M. L. Iu, Z. Yan, P. Charles, E. Chen, and A. S. Helmy, “Distributed feedback lasers using surface gratings in Bragg waveguides,” *Opt. Lett.*, vol. 46, no. 15, pp. 3689–3692, Optica Publishing Group, Aug. 2021. https://doi.org/10/gs3ghz

[170] B. Arar, “GaAs-based components for photonic integrated circuits,” M.S. Thesis, TU Berlin, Berlin, 2019. [Online]. Available: https://d-nb.info/118242290X/34

[171] K. Ogawa, W. Chang, B. Sopori, and F. Rosenbaum, “A theoretical analysis of etched grating couplers for integrated optics,” *IEEE J. Quantum Electron.*, vol. 9, no. 1, pp. 29–42, Jan. 1973. https://doi.org/10/dt794m

[172] A. Michaels and E. Yablonovitch, “Inverse design of near unity efficiency perfectly vertical grating couplers,” *Opt. Express*, vol. 26, no. 4, pp. 4766–4779, Feb. 2018. https://doi.org/10.1364/oe.26.004766

[173] S. Wang *et al.*, “Compact high-efficiency perfectly-vertical grating coupler on silicon at O-band,” *Opt. Express*, vol. 25, no. 18, pp. 22032–22037, Sep. 2017. https://doi.org/10.1364/oe.25.022032

[174] K. Harper, “Theory, Design, and Fabrication of Diffractive Grating Coupler for Slab Waveguide,” 2003. [Online]. Available: https://scholarsarchive.byu.edu/etd/101

[175] T. Suhara, K. Okada, T. Saso, and H. Nishihara, “Focusing grating coupler in AlGaAs optical waveguide,” *IEEE Photonics Technol. Lett.*, vol. 4, no. 8, pp. 903–905, Aug. 1992. https://doi.org/10.1109/68.149903

[176] X. Zhou, I. Kulkova, T. Lund-Hansen, S. L. Hansen, P. Lodahl, and L. Midolo, “High-efficiency shallow-etched grating on GaAs membranes for quantum photonic applications,” *Appl. Phys. Lett.*, vol. 113, no. 25, p. 251103, Dec. 2018. https://doi.org/10.1063/1.5055622

[177] Y. Luo and D. C. Hall, “Nonselective Wet Oxidation of AlGaAs Heterostructure Waveguides Through Controlled Addition of Oxygen,” *IEEE J. Sel. Top. Quantum Electron.*, vol. 11, no. 6, pp. 1284–1291, Nov. 2005. https://doi.org/10/dzc4xn

[178] D. Liang, J. Wang, and D. C. Hall, “Single-Facet Folded-Cavity Diode Laser With Ultrasmall Bend Radius High-Index-Contrast Oxidized AlGaAs Ridge Waveguide,” *IEEE Photonics Technol. Lett.*, vol. 19, no. 8, pp. 598–600, Apr. 2007. https://doi.org/10.1109/lpt.2007.893907

[179] Y. Lou and D. C. Hall, “Low-loss nonselectively oxidized AlxGa1−xAs heterostructure waveguides,” *Appl. Phys. Lett.*, vol. 93, no. 26, p. 261111, Dec. 2008. https://doi.org/10.1063/1.3058709

[180] D. Liang and D. C. Hall, “Reduction of etched AlGaAs sidewall roughness by oxygen-enhanced wet thermal oxidation,” *Appl. Phys. Lett.*, vol. 91, no. 6, p. 061110, Aug. 2007. https://doi.org/10.1063/1.2766859

[181] J. F. Bauters *et al.*, “Oxygen-enhanced wet thermal oxidation of GaAs,” *Appl. Phys. Lett.*, vol. 99, no. 14, p. 142111, American Institute of Physics, Oct. 2011. https://doi.org/10/fd53m2

[182] Micro Cooling Concepts, Inc, “Microchannel/Microimpingement Coolers.” Accessed: Oct. 6, 2023. [Online]. Available: https://www.microcoolingconcepts.com/coolers.html

[183] A. Villeneuve, C. C. Yang, G. I. Stegeman, C. N. Ironside, G. Scelsi, and R. M. Osgood, “Nonlinear absorption in a GaAs waveguide just above half the band gap,” *IEEE J. Quantum Electron.*, vol. 30, no. 5, pp. 1172–1175, May 1994. https://doi.org/10.1109/3.303676

[184] D. A. Kleinman, R. C. Miller, and W. A. Nordland, “Two-photon absorption of Nd laser radiation in GaAs,” *Appl. Phys. Lett.*, vol. 23, no. 5, pp. 243–244, American Institute of Physics, Sep. 1973. https://doi.org/10/d4zcxg

[185] S. Krishnamurthy, Z. G. Yu, L. P. Gonzalez, and S. Guha, “Temperature- and wavelength-dependent two-photon and free-carrier absorption in GaAs, InP, GaInAs, and InAsP,” *J. Appl. Phys.*, vol. 109, no. 3, p. 033102, American Institute of Physics, Feb. 2011. https://doi.org/10/dhp7sj

[186] H. Q. Le, H. K. Choi, and C. A. Wang, “Measurement of the two-photon absorption coefficient in a GaAs/AlGaAs quantum well laser,” *Appl. Phys. Lett.*, vol. 57, no. 3, pp. 212–214, American Institute of Physics, Jul. 1990. https://doi.org/10/b5h3f5

[187] Z. Zheng, A. M. Weiner, J. H. Marsh, and M. M. Karkhanehchi, “Ultrafast optical thresholding based on two-photon absorption GaAs waveguide photodetectors,” *IEEE Photonics Technol. Lett.*, vol. 9, no. 4, pp. 493–495, Apr. 1997. https://doi.org/10/cqtsbc

[188] P. Bhasker, J. Norman, J. E. Bowers, and N. Dagli, “Low Voltage, High Optical Power Handling Capable, Bulk Compound Semiconductor Electro-optic Modulators at 1550 nm,” *J. Light. Technol.*, pp. 1–1, 2020. https://doi.org/10/ggjb4k

[189]N. Dostart *et al.*, “Serpentine optical phased arrays for scalable integrated photonic lidar beam steering,” *Optica*, vol. 7, no. 6, pp. 726–733, Optical Society of America, Jun. 2020. https://doi.org/10/gg2qmv

[190] Y. Ren *et al.*, “Compact 2D serpentine optical phased array,” *Appl. Opt.*, vol. 60, no. 24, pp. 7158–7163, Optical Society of America, Aug. 2021. https://doi.org/10/gng7jg

[191] J. Sun, E. Timurdogan, A. Yaacobi, E. S. Hosseini, and M. R. Watts, “Large-scale nanophotonic phased array,” *Nature*, vol. 493, no. 7431, pp. 195–199, Jan. 2013. https://doi.org/10.1038/nature11727

[192] F. Aflatouni, B. Abiri, A. Rekhi, and A. Hajimiri, “Nanophotonic projection system,” *Opt. Express*, vol. 23, no. 16, pp. 21012–21022, Aug. 2015. https://doi.org/10.1364/oe.23.021012

[193] H. Abediasl and H. Hashemi, “Monolithic optical phased-array transceiver in a standard SOI CMOS process,” *Opt. Express*, vol. 23, no. 5, pp. 6509–6519, Mar. 2015. https://doi.org/10.1364/oe.23.006509

[194] F. Ashtiani and F. Aflatouni, “N × N optical phased array with 2N phase shifters,” *Opt. Express*, vol. 27, no. 19, pp. 27183–27190, Sep. 2019. https://doi.org/10.1364/oe.27.027183

[195] J. Notaros, C. V. Poulton, M. J. Byrd, M. Raval, and M. R. Watts, “Integrated optical phased arrays for quasi-Bessel-beam generation,” *Opt. Lett.*, vol. 42, no. 17, pp. 3510–3513, Sep. 2017. https://doi.org/10.1364/ol.42.003510

[196]F. Xiao and L. Kong, “Optical multi-beam forming method based on a liquid crystal optical phased array,” *Appl. Opt.*, vol. 56, no. 36, pp. 9854–9861, Dec. 2017. https://doi.org/10.1364/ao.56.009854

[197] Y. Wu *et al.*, “Multi-beam optical phase array for long-range LiDAR and free-space data communication,” *Opt. Laser Technol.*, vol. 151, p. 108027, Jul. 2022. https://doi.org/10/gs3ghc

[198] D. J. Geisler, C. M. Schieler, T. M. Yarnall, M. L. Stevens, B. S. Robinson, and S. A. Hamilton, “Demonstration of a variable data-rate free-space optical communication architecture using efficient coherent techniques,” *Opt. Eng.*, vol. 55, no. 11, p. 111605, Aug. 2016. https://doi.org/10.1117/1.oe.55.11.111605

[199] R. Fatemi, A. Khachaturian, and A. Hajimiri, “Scalable Optical Phased Array with Sparse 2D Aperture,” *Conf. Lasers Electro-Opt. 2018 Pap. STu4B6*, May 13, 2018, p. STu4B.6. https://doi.org/10.1364/cleo_si.2018.stu4b.6

[200] Q. Huang *et al.*, “Sparse 2-D optical phased array with large grating-lobe-free steering range based on an aperiodic grid,” *Opt. Lett.*, vol. 48, no. 11, pp. 2849–2852, Optica Publishing Group, Jun. 2023. https://doi.org/10/gs3ggc

[201] D. Shin *et al.*, “Aperiodic optical phased array based on number theory,” Optica Open, Feb. 2023. https://doi.org/10.1364/opticaopen.22005074.v1

[202] T. Fukui *et al.*, “Non-redundant optical phased array,” *Optica*, vol. 8, no. 10, pp. 1350–1358, Optica Publishing Group, Oct. 2021. https://doi.org/10/gnsmkb